

**DOUBLE RESONANT CHARACTER IN AN OPTICAL
CAVITY FOR HIGH PERFORMANCE AND STABLE
POLYMER SOLAR CELLS**

QUAN LIU

ICFO – INSTITUTE DE CIÈNCIES FOTÒNIQUES
UNIVERSITAT POLITÈCNICA DE CATALUNYA
BARCELONA, ESPAÑA 2018

KIT-KARLSRUHE INSTITUTE OF TECHNOLOGY
KARLSRUHE, GERMANY 2018

**DOUBLE RESONANT CHARACTER IN AN OPTICAL
CAVITY FOR HIGH PERFORMANCE AND STABLE
POLYMER SOLAR CELLS**

Quan LIU

under the supervision of

Main advisor: Jordi MARTORELL (ICFO)

Co-advisor: Uli LEMMER (KIT)

submitted this thesis in partial fulfillment

of the requirements for the degree of

DOCTOR

by the

UNIVERSITAT POLITÈCNICA DE CATALUNYA, 2018

KARLSRUHE INSTITUTE OF TECHNOLOGY, 2018

To my family

Acknowledgements

First, let me thank the European Commission for offering me an opportunity to study at the Institute of Photonic Science (ICFO).

I would like to thank my advisor *Prof. Jordi Martorell* for his patient guidance and strong support throughout my Ph.D work. The most valuable thing I have learned from him could be how to use photon management to improve light absorption in thin film solar cells and how to write a good scientific paper.

I would also like to thank my colleagues in Nanostructured Organic Photovoltaic group (Alberto Martinez-Otero, Miguel Montes, Pablo Romero, Paola Mantilla, Silvia Colodrero, Laura Ciammaruchi, Johann Toudert, Guillermo, *et al.*) for assistance in device fabrication and characterization, as well as Vittoria Finazzi and Carlos Dengra for technical support.

Finally, I would like to thank my parents and my wife, Qian for their love, tolerance and support all the time.

The work in this thesis was supported by the European Commission through the Erasmus Mundus Joint Doctorate Programme Europhotonics (Grant No.159224-1-2009-1-FR-ERAMUNDUSMJD).

Abstract

Solution-processed thin film solar cells emerged as very promising photovoltaic technologies suitable for a low cost roll-to-roll upscale production. Such thin film character also ensures lightweight and flexibility for the solar cell modules, making them ideal for a wide variety of applications where silicon panels cannot be used. In addition to the above-mentioned advantages, common in all solution-processed thin film technologies, polymer solar cells (PSCs) have a unique semitransparency, which makes them very useful for solar window applications and very competitive in building integrated photovoltaics.

In recent years, a remarkable progress has been achieved in the field of PSCs. The power conversion efficiency of PSCs has already surpassed the 11% barrier. However, to be able to eventually compete with other solution-processed thin film technologies, such device efficiency must be further improved. Given the low charge carrier mobility in commonly used organic π -conjugated semiconductors, the tradeoff between optical absorption and charge collection, limits the thickness of the majority of photoactive layers currently being used to approximately 100 nm. To overcome the limited light absorption in such thin active layers, an adequate optical management becomes very important. Ideally, a light absorption or short-circuit current enhancement should be achieved without affecting the other photovoltaic parameters, such as the photovoltaic device open circuit voltage and fill factor.

In this thesis, we implement a one-dimensional new optical planar cavity that exhibits a resonant character at two different nonharmonic frequencies of each other, which we

named two-resonance tapping cavity (TRTC). With such TRTC we demonstrate that one may reach an optimal broadband light trapping in thin film cells, largely improving the photocurrent of the solar without sacrificing the device electrical properties.

A limited stability is another obstacle that may prevent any industrial application of the PSC technology. In accordance, in parallel to a device efficiency increase one must address the problem of a short operational device lifetime. In the current thesis, we performed several experiments, which lead us to understand the physics behind the rapid destruction of the active layer nanomorphology under illumination. In addition, we propose and implement a new procedure based on the formation of a highly ordered PCBM phase to circumvent such degradation path, and achieve high-performance PSCs with long lifetimes.

The current thesis has been divided into five chapters. Chapter 1 briefly reviews some photon management approaches and some basics of degradation mechanisms in PSCs. Chapter 2 describes the TRTC concept and the experimental implementation of PTB7-Th:PC₇₁BM cells integrated in such TRTC. In Chapter 3 we describe the use of the TRTC concept presented in Chapter 2 to achieve an optimal balance between open circuit voltage and photocurrent in flexible PBDBT:ITIC cells. In Chapter 4 we demonstrate an approach to increase the operational lifetimes of PSCs based on a UV treatment to actively remove chemisorbed oxygen on the ZnO interlayer. Finally, in Chapter 5, an in-depth study of the fast burn-in loss for PTB7-Th:PC₇₁BM cells is given, and a new explanation to the such degradation path is proposed. In addition, we propose and implement an approach to circumvent such degradation and achieve long lifetime high efficiency solar cells.

Resumen

Las celdas solares de capa fina procesadas por métodos en solución surgieron como una interesante tecnología fotovoltaica para una producción *roll-to-roll* a bajo coste. El carácter de película delgada también asegura el bajo peso y la flexibilidad de los módulos solares, haciéndolos ideales para una gran variedad de aplicaciones donde los paneles de silicio no pueden ser usados. Además de las ventajas mencionadas, compartidas por todas las tecnologías de capa fina procesadas en solución, las celdas solares de polímero (PSCs) presentan propiedades únicas de semi-transparencia, lo que las hace útiles para aplicaciones en ventanas solares y muy competitivas como elementos integrados en edificios.

En los últimos años, se ha logrado un progreso notable en el campo de las PSCs. La eficiencia de conversión de energía de las PSCs ha superado ya la barrera del 11%. Sin embargo, para poder competir finalmente con otras tecnologías de capa delgada procesadas en solución, la eficiencia del dispositivo debe mejorarse aún más. Debido a la baja movilidad de los portadores de carga para los típicos semiconductores orgánicos π -conjugados, el compromiso entre absorción óptica y recolección de carga limita el espesor de la mayoría de las capas fotoactivas que se utilizan actualmente a aproximadamente 100 nm. Para mejorar la limitada absorción de luz en dichas capas activas, el uso de estrategias ópticas adecuadas es muy relevante. Idealmente, se debería lograr un aumento de la absorción de la luz o de la corriente a cortocircuito sin afectar a los demás parámetros fotovoltaicos, tales como el voltaje a circuito abierto y el factor de llenado del dispositivo fotovoltaico.

En esta tesis, incorporamos una nueva cavidad óptica planar unidimensional que presenta un carácter resonante en dos frecuencias no armónicas diferentes, y que llamamos *two-resonance tapping cavity* (TRTC). Con la TRTC demostramos que puede alcanzarse una captura óptima de la luz en celdas de capa fina sobre un amplio rango de longitudes de onda, mejorando en gran medida la fotocorriente sin sacrificar las propiedades eléctricas del dispositivo solar. La falta de estabilidad es otro obstáculo que puede prevenir la aplicación industrial de la tecnología de PSCs. De esta manera, en paralelo a un aumento de la eficiencia del dispositivo, se debe abordar el problema de su corta vida operativa. En esta tesis, llevamos a cabo varios experimentos para entender la física que determina el rápido deterioro de la nanomorfología de la capa activa en condiciones de iluminación. Además, proponemos e implementamos un nuevo procedimiento basado en la formación de una fase de PCBM altamente ordenada para eludir la vía de degradación y conseguir PSCs de alto rendimiento con una vida útil extendida.

La tesis se ha dividido en cinco capítulos. El Capítulo 1 revisa brevemente algunas de las estrategias para la manipulación de fotones y las bases de los mecanismos de degradación en PSCs. El Capítulo 2 describe el concepto de TRTC y la implementación experimental de celdas de PTB7-Th:PC₇₁BM incluyendo la TRTC. En el Capítulo 3 describimos el uso del concepto TRTC presentado en el Capítulo 2 para conseguir un balance óptimo entre voltaje a circuito abierto y fotocorriente en celdas flexibles de PBDBT:ITIC. En el Capítulo 4 demostramos una estrategia para mejorar la vida operativa de los PSCs basado en un tratamiento con luz UV para eliminar activamente el oxígeno quimisorbido en la capa de ZnO. Finalmente, en el Capítulo 5, se presenta un estudio en profundidad de la *fast burn-in loss* para las celdas de PTB7-Th:PC₇₁BM, y se propone una nueva explicación de la ruta de degradación. Además, proponemos e implementamos una alternativa para evitar la degradación y conseguir celdas solares de alta eficiencia con una larga vida útil.

Academic production

List of Publications

1. **Q. Liu***, J. Toudert, L. Ciammaruchi, G. Martínez-Denegri, J. Martorell. High open-circuit voltage and short-circuit current flexible polymer solar cells using ternary blends and ultrathin Ag-based transparent electrodes *J. Mater. Chem. A* **5**, 25476–25484 (2017)
2. **Q. Liu**, J. Toudert, F. Liu, P. Mantilla-Perez, M. M. Bajo, T. P. Russell, J. Martorell. Circumventing UV light induced nano-morphology disorder to achieve long lifetime PTB7-Th:PCBM based solar cells. *Adv. Energy Mater.* **7**, 1701201 (2017).
3. **Q. Liu**, P. Romero-Gomez, P. Mantilla-Perez, S. Colodrero, J. Toudert, J. Martorell. A two-resonance tapping cavity for an optimal light trapping in thin-film solar cells. *Adv. Energy Mater.* **7**, 1700356 (2017).
4. P. Mantilla-Perez, T. Feurer, J.-P. Correa-Baena, **Q. Liu**, S. Colodrero, J. Toudert, M. Saliba, S. Buecheler, A. Hagfeldt, A. N. Tiwari, J. Martorell. Monolithic CIGS–Perovskite tandem cell for optimal light harvesting without current matching. *ACS Photonics* **4**, 861–867 (2017).

5. **Q. Liu***, P. Mantilla-Perez, M. Montes Bajo, P. Romero-Gomez, J. Martorell. UV-induced oxygen Removal for Photostable, High-Efficiency PTB7-Th:PC₇₁BM Photovoltaic cells. *ACS Appl. Mater. Interfaces* **8**, 28750–28756 (2016).
6. X. Elias†, **Q. Liu**†, C. Gimbert-Surinach, R. Matheu, P. Mantilla-Perez, A. Martínez-Otero, X. Sala, J. Martorell, A. Llobet. Neutral water splitting catalysis with a High FF triple junction polymer cell. *ACS Catal.* **6**, 3310–3316 (2016) (**†Equal contribution**).
7. D. S. Ghosh, **Q. Liu***, P. Mantilla-Perez, T. L. Chen, V. Mkhitarian, M. Huang, S. Garner, J. Martorell, V. Pruneri. Highly flexible transparent electrodes containing ultrathin silver for efficient polymer solar cells. *Adv. Funct. Mater.* **25**, 7309–7316 (2015) (***Corresponding author**).
8. A. Martínez-Otero, **Q. Liu**, P. Mantilla-Perez, M. Montes Bajo, J. Martorell. An extremely thin and robust interconnecting layer providing 76% fill factor in a tandem polymer solar cell architecture. *J. Mater. Chem. A* **3**, 10681–10686 (2015).

Book chapters

1. P. Mantilla-Perez, **Q. Liu**, S. Colodrero, P. Romero-Gomez, and J. Martorell. The Future of Semiconductor Oxides in Next Generation Solar Cells. Chapter 12–*Photon Management with oxides in organic solar cells*. Elsevier, 481–499 (2018).

Table of Contents

Abstract	i
Resumen	iii
Academic production	v
1 Introduction	19
1.1 The state-of-the-art organic PVCs.....	22
1.2 Operational principle of PSCs.....	23
1.3 Photon management for improving light absorption in PSC	29
1.4 Overcoming unstable blend nanomorphology in PSCs	31
1.5 Thesis objectives and outline	33
2 Broadband light trapping in thin film solar cells	36
2.1 Two-resonance tapping cavity concept.....	37
2.2 Materials and architectures for TRTC-based cells.....	41
2.3 Design of optimal thin-film solar cells incorporating a TRTC	47
2.4 Conclusions	52
3 High-performance flexible PSCs using a TRTC electrode	54
3.1 Optical properties of ITIC and ternary PBDBT:ITIC:PC ₇₁ BM blend films.....	55
3.2 High performance non-fullerene blend based TRTC cells.	58
3.3 Integration of TRTC on PET substrates for high-performance flexible cells.....	64
3.4 Impact of PC ₇₁ BM on thermal stability for ternary solar cells	67

3.5 Conclusions	68
4 UV-induced molecular oxygen removal for enhanced stability	69
4.1 Device structure and photostability of PTB7-Th:PC ₇₁ BM active layer.....	70
4.2 Influence of UVN treatment on device performance.....	72
4.3 Effect of UVN treatment on device photostability.	78
4.4 Conclusions	82
5 Circumventing light-induced PCBM disorder for long lifetime PSC	83
5.1 Light-induced burn-in in PTB7-Th:PC ₇₁ BM polymer solar cells.....	84
5.2 UV-induced degradation of exciton diffusion and charge mobility in PC ₇₁ BM nano domains	89
5.3 Circumventing PCBM disorder to achieve highly stable cells with high efficiency.....	92
5.4 Conclusions	102
Conclusions.....	103
Appendix A.....	105
Appendix B.....	108
Appendix C.....	120
Appendix D.....	122
Appendix E.....	124
Reference	127

Chapter 1

Introduction

In the past decades, human activity induced global climate change has become a matter of growing concern. The primary driver of the climate change is the massive use of fossil fuels, which results in large carbon dioxide (CO₂) emissions, accounting for more than 60% of total heat-trapping gases emitted into our atmosphere. When compared to the global CO₂ level before the start of the industrial revolution, the current level has increased by more than 45% and reaching up to above 400 ppm¹. A clear sign of the CO₂ impact on the earth's climate is that the yearly average global temperature in the recent years, in particular, 2016, is the highest ever recorded. If the global warming continues, the dangerous threshold of a 2 °C temperature rise could be surpassed, and potentially catastrophic consequences for the climate may occur².

Today's global primary energy consumption has reached the level of 13 Billion toes (Btoes)ⁱ in 2016^{3,4}, and is expected to steadily grow and exceed 17 Btoes by 2035, as shown in **Figure 1.1a**. To alleviate the accumulation rate of CO₂ in the atmosphere, burning of oil and coal must continue to decrease, while the use of renewable energies, including wind, solar, geothermal, biomass, and biofuels has to significantly

ⁱ Tonne of oil equivalent (toe) is a unit of energy. 1 toe = 11,630 kilowatt hours (kwh).

Chapter 1. Introduction

increase in the next decades, as seen in the energy use forecast depicted in **Figure 1.1b**. In such forecast, the renewable energy share in the primary energy distribution is estimated to increase up to 10% by 2035. Among the renewable sources, solar energy is the most abundant with a solar irradiation on the surface of the earth equivalent to 170,000 terawatts per year, which is about 10,000 times larger than the present world energy consumption. Solar photovoltaic technology, directly converting solar energy to electricity, has been generally accepted as one of the optimal solutions, not only to supply a sustainable energy to meet the global energy demand but also to reduce carbon emissions and air contaminants.

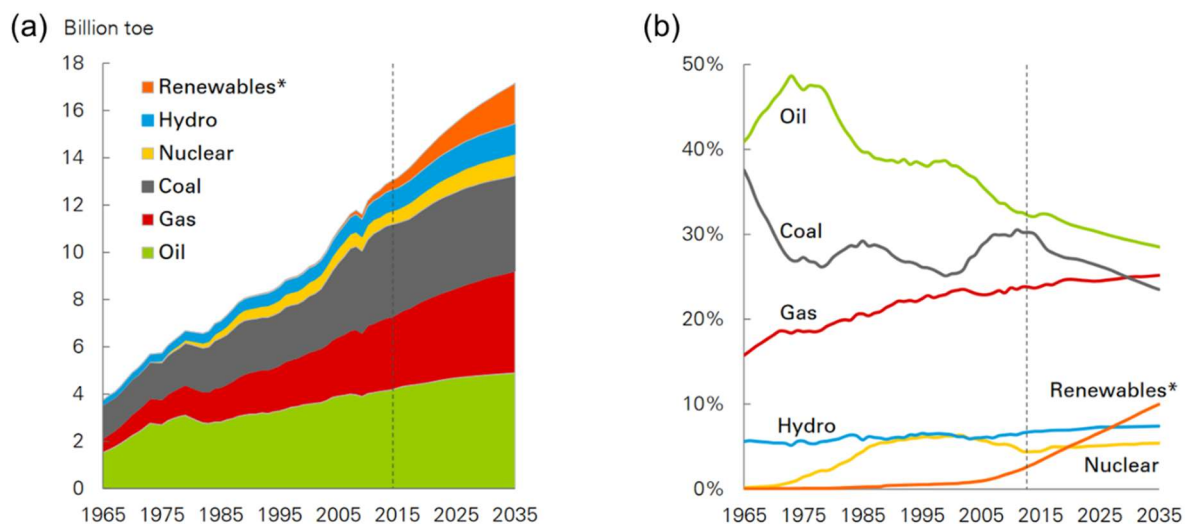


Figure 1.1. (a) Total global primary energy consumption by type. (b) Percentage share of primary energy. *Renewables here include wind, solar, geothermal, biomass, and biofuels. Source: BP Energy Outlook (2017)³.

Photovoltaic cells (PVCs) have experienced a rapid development since 1975, with power conversion efficiencies of single-junctions increasing from 6% to above 26%, as indicated in **Figure 1.2** (NREL chart). Currently, crystalline and polycrystalline silicon PVCs dominate the solar market, representing about 90% of the world total solar cell production, due to their high efficiency, excellent reliability, and maturity of the technology. However, such PVC technologies have a relatively long energy payback time, and it is difficult for them to produce solar modules using a large-scale

Chapter 1. Introduction

roll-to-roll manufacturing method. Solution-processed thin film PVC technologies, which can be implemented in a potentially low cost roll-to-roll production, have been developed in the past two to three decades. Such technologies include mesoporous dye-sensitized, quantum dots, copper zinc tin sulfide (CZTS), perovskite-based inorganic cells, and polymer or small molecular based organic cells. The efficiency evolution for such emerging solution-process thin-film PVCs is summarized in **Figure 1.2**.

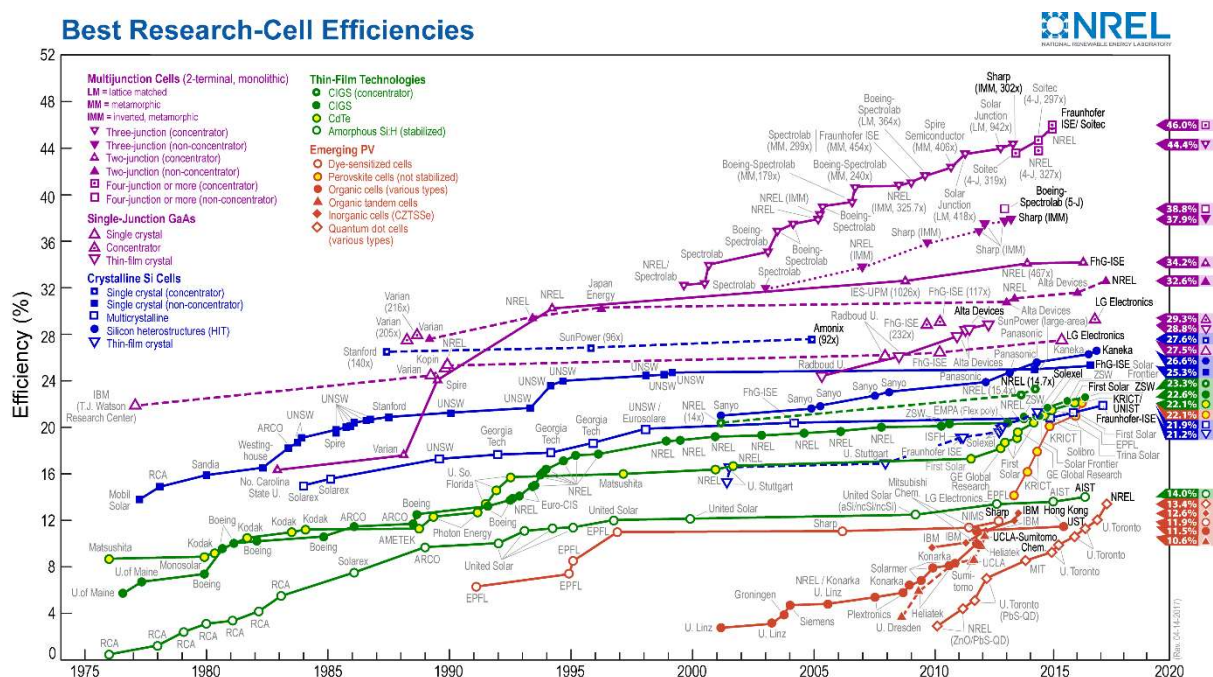


Figure 1.2. Record efficiencies certified by NREL for various photovoltaic technologies⁵.

With a continuous effort on improving the performance of such solution-processed thin film solar cells, a power conversion efficiency (PCE) comparable to the one from silicon PVCs has been achieved in recent years. Indeed, a single-junction perovskite-based cell recently reached a record efficiency higher than 22%⁶, exceeding the performance of polycrystalline silicon solar cells, while all the other emerging technologies already surpassed the 11% PCE barrier. These scientific breakthroughs put such potentially lower cost solar technologies closer to a commercial application.

Chapter 1. Introduction

1.1 The state-of-the-art organic PVCs

Compared to other emerging solar cells, which exhibit a higher record PCE, the organic PVC technology exhibits very good reproducibility, reliability in the fabrication, and an extremely low environmental impact. More importantly, after more than 30 years of research, the organic based PVCs has become a very mature technology, which is very close to being ready for an up-scaling and a production in a continuous processing using printing or other similar solution-based material deposition in a roll-to-roll configuration⁷. In addition, organic PVCs may provide a wide choice of photoactive materials, given that molecular engineering can tailor the material properties by a relatively simple modification of functional groups in polymers or small molecules. Indeed, with a proper molecular design, organic material based solar devices have a great potential to be incorporated in semitransparent photovoltaic windows, making organic PVC one of the most competitive technologies in building integrated photovoltaics (BIPV).

A steady increase in PCE of polymer solar cells (PSCs) has been reported resulting from the combined efforts in the synthesis of new polymers⁸, the use of non-fullerene blends⁹, the implementation of ternary blends¹⁰, a better morphology control or interfacial engineering¹¹, and an optimal photon management¹². The high performance PffBT4T-C₉C₁₃:PC₇₁BM fullerene blend, and PBDBT:ITIC non-fullerene blend led to certified PCEs for single-junction cells surpassing 11%^{13,14}. Some estimates indicate that organic materials based solar cells may soon reach 15% PCE¹⁵.

The low charge mobility in the organic absorbers is still one of the critical factors limiting a further increase in the PCE of organic cells. A dramatic reduction in fill factor (*FF*), indicating an inefficient charge collection, is normally observed when active layers thicker than 200 nm are being used. An optimal balance between the light absorption and charge collection is typically reached for state-of-the-art PSCs when the active layer thickness is approximately 100 nm. Therefore, photon

Chapter 1. Introduction

management becomes of great importance in enhancing the light harvesting efficiency in such extremely thin PSCs. As will be discussed below in **Section 1.3**, many different optical strategies have been explored in recent years for improving light absorption and consequently PCE in polymer cells.

In addition, PSCs exhibit a relatively short operational lifetime when compared to silicon cells. This issue may severely limit their industrial application. In recent years, various degradation mechanisms caused by external agents such as oxygen, moisture, light or heat have been proposed. At the same time, several experimental reports indicated that the nanomorphology instability of the active layer in the presence of some or all such agents may play a very relevant role in the device degradation path¹⁶. In **Section 1.4** of the current thesis, we summarize the approaches reported in the literature for overcoming the degradation of the blend nanomorphology to prolong device operational lifetime.

1.2 Operational principle of PSCs

PSC devices rely on a mixture of a light-sensitive polymer or small molecular donor and a fullerene derivative as an acceptor to absorb light, generate excitons and produce electricity. In order to create more donor/acceptor interfaces within the exciton diffusion length, the mixtures are typically blended in a nanoscale network known as a bulk heterojunction (BHJ). This concept was initially proposed by Prof. Heeger in 1995¹⁷ and still is widely used today. In most of the experimental studies reported in this thesis, we use a high performance fullerene BHJ blend consisting of PTB7-Th polymer donor and PC₇₁BM acceptor. In some cases, we also consider a non-fullerene blend consisting of PBDBT polymer donor and the ITIC acceptor. Their respective molecular structures are shown in **Figure 1.3**. Note that to achieve an optimal active layer morphology in the current high-performance PSCs, a small quantity of the high boiling point additive, such as diiodooctane (DIO), is often added

Chapter 1. Introduction

to the blend solution during spin coating¹⁸. DIO can effectively suppress the formation of the large-scale donor/acceptor phase segregation, leading to a more homogeneous nanomorphology allowing for a more efficient charge generation and transport.

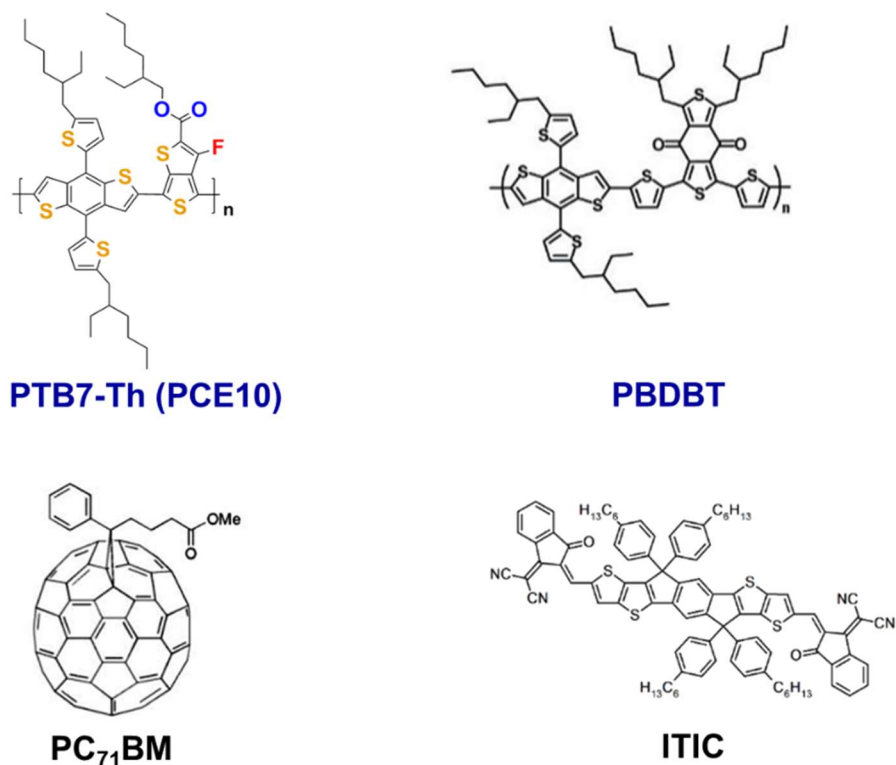


Figure 1.3. Molecular structures of the donor and acceptor materials.

To complete a PSC device, the BHJ active layer is typically sandwiched between an electron-transporting layer (ETL) and a hole-transporting layer (HTL), and a front transparent electrode and a back metal opaque electrode are used to collect the extracted photo-generated carriers, as schematically depicted in **Figure 1.4**.

In such BHJ based solar cells, the currently accepted mechanism for photocurrent generation is described in the following four key steps, including exciton generation, exciton diffusion, exciton separation, and charge collection, as indicated in Figure 1.4.

Chapter 1. Introduction

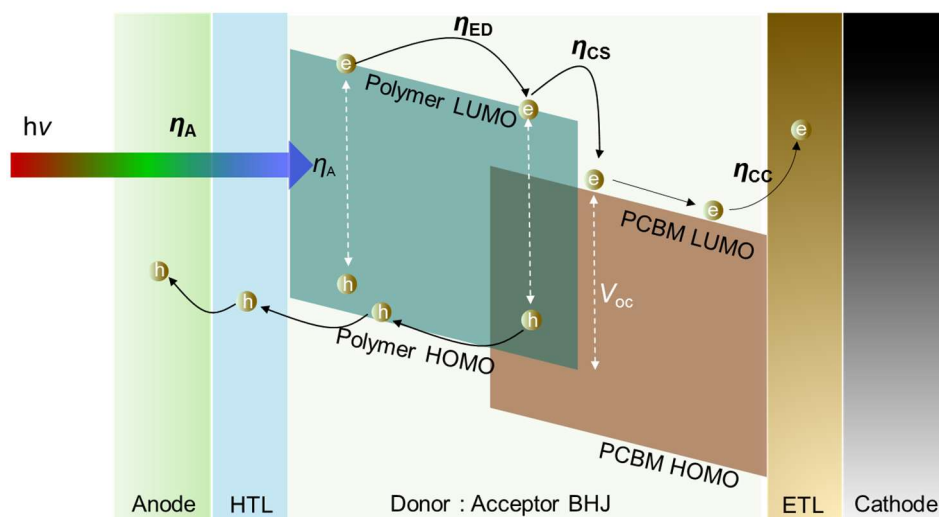


Figure 1.4. Working principle for organic BHJ solar cells indicated the several steps from light absorption to charge collection. Here, HOMO and LUMO indicate highest occupied molecular orbital and lowest unoccupied molecular orbital, respectively.

Exciton generation. Photons with an energy above the bandgap (E_g) of the photoactive material are absorbed when the sunlight passes through the device to generate bound excitons. The efficiency in the photogeneration of excitons is given by the photon absorption efficiency (η_A). As indicated above, given the reduced thickness of the active layer in the majority of polymer cells, more than 20% of the photons are scattered out of the device or absorbed outside of the active layer.

Exciton diffusion. After creation, an exciton may diffuse to the donor/acceptor interface for separation. The exciton diffusion length (L_D) is used, here, to characterize the distance that an exciton can migrate before charge recombination, and is given by:

$$L_D = \sqrt{D\tau} \quad (1.1)$$

where D is the exciton diffusion coefficient and τ is the average exciton lifetime. Since such lifetime in most polymer films is typically less than 1 ns, the L_D is limited to less than 10 nm. Consequently, the size of polymer domains should be just a few

Chapter 1. Introduction

nm to allow for an efficient exciton dissociation at the donor/acceptor interfaces. This is the case for many of the BHJs used in PSCs, which exhibit a morphology consisting of interconnected nano-domains or nano-channels. The efficiency of the excitons reaching such BHJ interfaces prior to recombination is determined by the exciton diffusion efficiency (η_{ED}).

Charge separation. Due to the relatively high electron-hole binding energy of ~ 0.3 - 1 V, an energetic offset at the p-n material interface is required to split the exciton and create free carriers. To reach an efficient exciton dissociation at the donor/acceptor interface, the LUMO offset of the donor and acceptor materials should be larger than 0.3 eV. The efficiency of the exciton dissociation process is determined by the charge separation efficiency (η_{CS}).

Charge transport and collection. Upon dissociation of the excitons, the free charge carriers will travel, under the action of a built-in electric field, in opposite directions to the respective electrodes for collection¹⁹. To reach an efficient charge transport, each donor or acceptor phase must exhibit continuous pathways from the charge generation sites to the electrodes. Otherwise, charges are either trapped or recombined with opposite charge carriers and thus cannot be collected by the respective electrodes. Therefore, the nanomorphology of the blend plays a fundamental role in the charge transport and collection. In addition, the interfacial layers (HTL and ETL) help to form good ohmic contacts between the active layer and the electrodes, leading to an effective extraction of the free carriers. The efficiency in collecting the separated charges at the layer/electrode interfaces that travel across the photoactive blend to reach the external circuit is given by the charge collection efficiency (η_{CC}).

Finally, the product of the four efficiencies above gives the external quantum efficiency (EQE (λ)):

$$\text{EQE}(\lambda) = \eta_A(\lambda) \times \eta_{ED} \times \eta_{CS} \times \eta_{CC} \quad (1.2)$$

Chapter 1. Introduction

The EQE (λ) is the ratio between the collected photo-generated carriers and the number of incident photons. The product of $\eta_{ED} \times \eta_{CS} \times \eta_{CC}$ represents the internal quantum efficiency (IQE), which is the ratio between the collected photo-generated carriers and the number of absorbed photons by the active layer and is typically wavelength independent. The IQE (λ) can be calculated as:

$$IQE = EQE(\lambda)/(1-R(\lambda)-A(\lambda)) \quad (1.3)$$

where $R(\lambda)$ is the total reflectance of the device and $A(\lambda)$ is the parasitic absorption in the non-active layers²⁰. For a single donor-acceptor BHJ system, the IQE may exhibit a weak wavelength dependency, which can be ascribed to a non-homogenous exciton diffusion within the active layer. In the majority of cases considered in this thesis, such non-homogeneous distribution can be ignored, except when considering the degradation mechanism described in Chapter 5.

With the EQE (λ) spectral response, the device short-circuit current density (J_{sc}) can be easily determined using the equation below:

$$J_{sc} = \int \frac{EQE(\lambda) \cdot P_{AM1.5}(\lambda) \cdot q \cdot \lambda}{h \cdot c} d\lambda \quad (1.4)$$

where $P_{AM1.5}$ is the photon flux of the global standard solar spectral irradiance at air mass 1.5 (AM1.5G), as shown in **Figure 1.5a**. By integrating the EQE over the solar electromagnetic spectrum, one can evaluate the maximum photocurrent that the cell will produce when exposed to sunlight. Figure 1.5b shows an EQE example for a typical PTB7-Th:PC₇₁BM solar cell, and the corresponding integrated J_{sc} calculated using the equation 1.4 above.

Chapter 1. Introduction

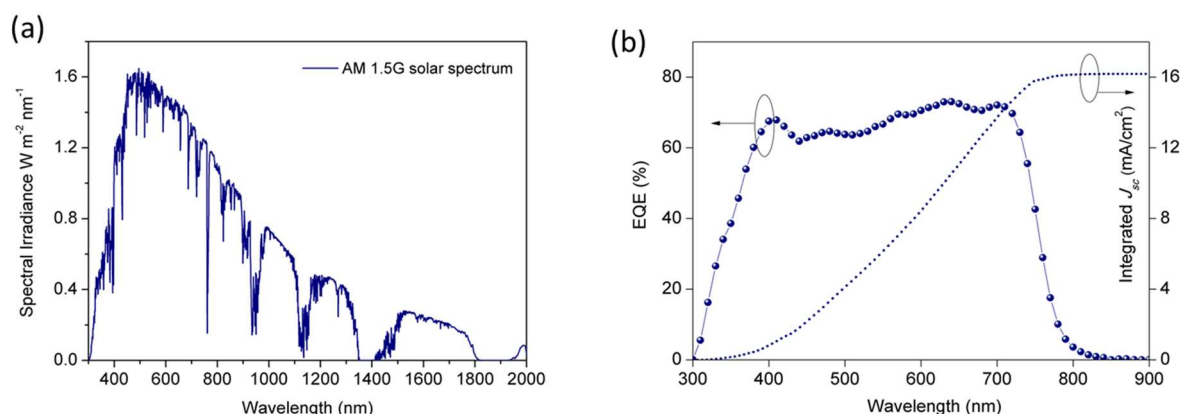


Figure 1.5. (a) Solar spectral irradiance at AM 1.5 collected from American Society for Testing and Materials (ASTM). Standard: ASTM G-173-03. (b) Numerically computed EQE (dots) and J_{sc} (dashed line) of a standard PTB7-Th:PC₇₁BM solar cell.

To characterize the electric performance of a solar cell, current density–voltage (J – V) characteristics may be recorded, both in the dark and under AM 1.5G 1-sun illumination, as shown in **Figure 1.6**. Based on the J – V curves, the photovoltaic parameters J_{sc} , open-circuit voltage (V_{oc}) and FF can be determined. The product between the photocurrent and voltage denoting the maximum power point (MPP), or where the output power is the largest, is indicated in Figure 1.6. The FF is defined as $FF = V_{MPP}I_{MPP}/(J_{sc}V_{oc})$, and characterizes how “rectangular” the J – V curve is. The FF is a measure of the competition between the sweep-out of the photo-generated carriers and the recombination of such carriers²¹. With such photovoltaic parameters, one may easily determine the PCE as:

$$PCE = \frac{P_{out}}{P_{In}} = \frac{V_{MPP}I_{MPP}}{P_{In}} = \frac{V_{oc}J_{sc}FF}{P_{In}} \quad (1.5)$$

where P_{In} is the incident light power, usually standardized to be a AM1.5G 1-sun illumination or 100 mW/cm². The limiting theoretical efficiency for a single-junction photovoltaic cell with a planar configuration is around 33% as can be determined from the Shockley-Queisser (SQ) detailed balance theory²².

Chapter 1. Introduction

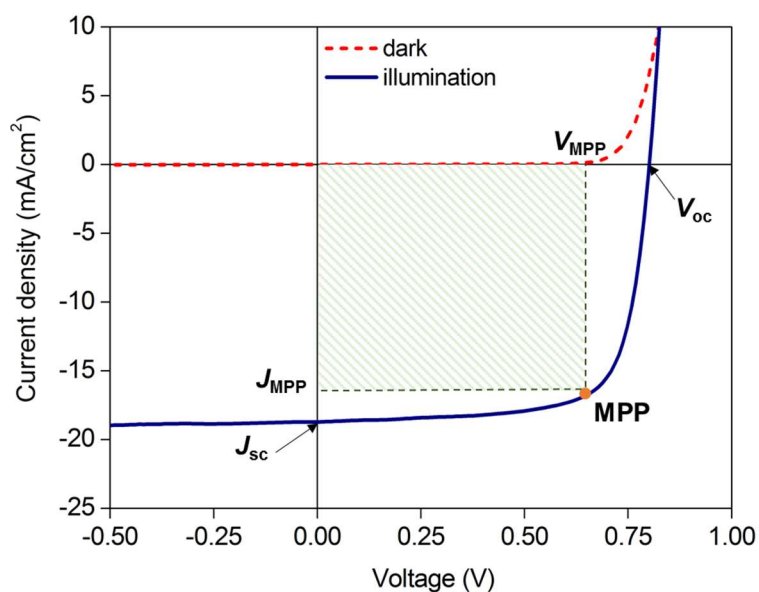


Figure 1.6. An example of typical J - V curves in the dark (dashed line) and under AM1.5G 1-sun illumination (solid line), with all the relevant points indicated.

1.3 Photon management for improving light absorption in PSC

As previously mentioned, the optimal active layer thickness for the state-of-the-art PSCs is normally limited to around 100 nm, resulting in a partial “escape” from the device of the incident light. Therefore, photon management plays a very important role in maximizing the light harvesting in such devices^{23,24}. Recently, tuning the thicknesses of the relevant layers in opaque single-junction PSCs provided an effective approach to redistribute the optical electrical field inside the device^{25,26,27}. In this way, an optimal light absorption within the active layer could be achieved. In addition, the improvement in light harvesting may be reached by using a buffer layer material with lower parasitic absorption, for instance, replacing Ca buffer material with a BCP organic layer²⁸. Moreover, a top illuminated cavity configuration reported by Chen, et al. demonstrated a significant photocurrent enhancement in PIDTT-DFBT:PC₇₁BM PSCs when a proper high refractive index capping layer was used²⁹. Such one-dimension (1-D) photon management approaches have been proven to be very effective in the case of semi-transparent PSCs. For instance, Betancur, et al.

Chapter 1. Introduction

designed and implemented a 1-D non-periodic photonic structure deposited on top of the rear semitransparent electrode to enhance the light absorption in, both, near-UV and near-infrared regions in semi-transparent PSCs³⁰. As a result, the semitransparent PTB7:PC₇₁BM cells reached a performance equivalent to almost 80% that of its opaque counterpart, and exhibited a PCE of 5.6% with 30% visible light transmission. Later, Yu, et al. fabricated semitransparent PCDTBT:PC₇₁BM PSCs using 1-D photonic crystals as distributed Bragg reflectors (DBR)³¹. By tuning the pair number of the DBR, a high PCE of 5.3% was achieved and the average device transmission was around 28%. Zhang, et al. reported a roll-to-roll compatible semitransparent cell incorporating a bottom 1-D photonic crystal and a top solution-processed PEDOT:PSS layer³². The device performance was enhanced by 37% when compared with those of the cell without using photonic crystal, while maintaining the whole device semitransparent character.

A 1-D planar homo-tandem architecture is another effective method to overcome the reduced light absorption in the single-junction PSCs without degrading the device *FF*. Recently, two identical PTB7:PC₇₁BM subcells connected in series with an interconnecting layer (ICL) of MoO₃/Ag/PFN demonstrated ~12% efficiency enhancement compared to the single-junction counterpart³³. The enhancement mainly originated from the improved light harvesting capacity in the tandem cell. PCE enhancements are also achieved using such homo-tandem approach when other BHJ materials are used. For example, Zhou, et al. demonstrated that the fully optimized PTB7-Th:PC₇₁BM homo-tandem cells based on ZnO/CPEPh-Na ICL reached a PCE of 11.3%, approximately a 25% enhancement in efficiency compared to single junction cells³⁴. Moreover, Chen, et al. implemented a non-fullerene P3TEA:SF-PDI2 blend in a homo-tandem configuration using an ICL of PEDOT:PSS/ZnO, yielding a PCE of 10.8%, which was around 14% higher than the performance of the corresponding optimal single-junction cells³⁵.

Chapter 1. Introduction

Light absorption enhancements in single-junction PSCs have also been demonstrated by incorporating nanospheres, or nanostructuring in buffer layers or photoactive layers. For instance, Mariano, et al. implemented an array of parallel fibers to couple light in the whispering gallery and around 30% photocurrent enhancement was achieved in the P3HT:ICBA PSCs³⁶. Chen, et al. incorporated a nanoimprinted deterministic aperiodic nanostructure (DAN) on a ZnO layer to enhance the light harvesting in PTB7:PC₇₁BM cells. Compared with the planar reference device, nanostructured PSCs gained an 18% increase in photocurrent and a larger than 10% increase in PCE was obtained³⁷. Also, nanostructured devices can achieve up to 20% improvement in the photocurrent when incorporating the Moth's eye nanostructures (MEN) on the substrate^{38,39} or directly on the photoactive layer⁴⁰.

Metallic nanoparticles embedded into buffer layers or photoactive layers have also been demonstrated as an effective strategy to improve light harvesting in PSCs. This occurs because the metallic nanostructures can be used as subwavelength plasmons and scatterers to couple and trap the incident light into the thin photoactive layers^{41,42}. For example, Cheng, et al. introduced Ag NPs in the MoO₃ buffer layer in inverted P3HT:PC₆₁BM PSCs, achieving a 13% enhancement in light harvesting via plasmonic backscattering⁴³. A similar effect was also obtained⁴³ by implementing self-assembled plasmonic oligomers in the same blend based PSCs, which increased the photocurrent by more than 12%⁴⁴. Very recently, Choi, et al. incorporated silica-coated silver nanoparticles (Ag@SiO₂)⁴⁵ or carbon-dot-supported silver nanoparticles (CD-Ag)⁴⁶ as plasmonic materials into the PTB7:PC₇₀BM-based PSCs, resulting in remarkable enhancement in J_{SC} and thus PCE.

1.4 Overcoming unstable blend nanomorphology in PSCs

A fast degradation, known as burn-in⁴⁷, and long-term one are typically observed in PSCs under light aging, even when the cell is isolated from other external corrosive

Chapter 1. Introduction

agents by a proper encapsulation or by placing it in an inert atmosphere^{48, 49}. Schaffer, et al. reported a direct evidence of a morphological degradation in a P3HT:PCBM polymer solar cell by in situ micro-focused grazing incidence small angle X-ray scattering (μ GISAXS) measurements⁵⁰. The observed $\sim 25\%$ decrease in J_{sc} during the early stages of operation was quantitatively correlated with the morphological changes of the photoactive layer. To overcome the morphology instability, crosslinking strategies⁵¹ have been widely used for “locking” the as-cast blend morphology, including the incorporation of crosslinkable groups on the alkyl chains of the polymer^{52,53} or the fullerene derivatives⁵⁴. The addition of small molecule crosslinkers into the photoactive layer has been considered, too^{55,56}. For instance, P3HT-Br⁵³ and PBDTTPD-Br⁵⁴ are crosslinkable polymers, which exhibited significant enhancements in the long-term thermal stability compared to the non-crosslinkable counterparts. Rumer, et al. utilized a small molecular crosslinker of bis-azide 1,6-diazidohexane (DAZH) to enhance the blend stability without significantly impacting device performance⁵⁷. On the other hand, processing blend films without the small molecular additive, such as DIO, can also help to stabilize the blend morphology and thus improve the device stability^{57,58}.

As much as light tends to be a trigger to a degradation path, light-induced morphological stabilization has been demonstrated by Li, et al⁵⁹. The light exposure causes oligomerization of PC₆₀BM, enabling the PCDTBT/PCBM blend morphology stable under heat and light stresses. Increasing the polymer crystallinity is another alternative to improve the device operational stability. Heumueller, et al. demonstrated that highly crystalline materials, such as KP115, exhibit a reduced burn-in degradation and may be more stable under various conditions⁶⁰. A similar effect has been achieved by using a relative pure high molecular weight PCDTBT polymer⁶¹. The device maintained more than 82% of its initial efficiency even after 1,400 h light aging.

Very recently, non-fullerene PSCs have been proven to be more stable than fullerene analogues due to a relatively stable blend nanomorphology. Cha, et al. greatly

Chapter 1. Introduction

improved the stability of PffBT4T-2OD based PSCs by replacing PC₇₁BM with the EH-IDTBR non-fullerene small molecule acceptor⁶². Interestingly, no burn-in loss has been observed in such non-fullerene cells under illumination for more than 60 h. The burn-in free behavior was also found by Gasparini, et al., when using IDTBR, a non fullerene acceptor, instead of PCBM in the P3HT PSCs⁶³. After 2000 h light aging test, the P3HT:IDTBR cell PCE dropped less than 10% while a larger than 35% drop was seen in the fullerene cells.

1.5 Thesis objectives and outline

As noted PSCs can be fabricated with PCEs higher than 10%. This efficiency may be suitable for some applications, but for PSCs to be able to eventually compete with other technologies alternative to the silicon technology, such PSC efficiency must be further increased. If one takes a look at the average values of the three parameters that determine the PCE of many different state-of-the-art PSCs, it is quite obvious that V_{oc} , as well as J_{sc} , must be increased. This should be achieved without any reduction in FF , which is already comparable, or even higher, than the FF s found in solar cells from similar solution-processed techniques. As there are many issues in a PSC that can be linked to a reduced V_{oc} , the limited J_{sc} can be, to a large extent, almost exclusively linked to the approximately 100 nm thickness of the active layer. An objective of the current thesis is to increase such J_{sc} without any significant alteration or reduction of the other two photovoltaic parameters. This will be reached by implementing a light management as external as possible to the electrical part of the solar cell. It is also an objective of the current thesis to increase light absorption but not to introduce any alteration in the critical nanomorphology of the same active layer, which may also have a detrimental effect on the photovoltaic parameters. These are the main reasons why in the current thesis we adopted a 1-D approach to enhance light absorption in PSCs. In the past, 1-D approaches succeeded in improving the performance of semi-transparent PSCs but exhibited very limited results when opaque

Chapter 1. Introduction

cells were considered. The novel approach we followed aims at achieving a broadband light trapping with the implementation of a new optical planar cavity configuration that we named two-resonance tapping cavity (TRTC). This optical cavity exhibits a resonant character at two different non-harmonic frequencies, when adjusting the materials or geometry configurations of the partially transparent front cavity layers. The effectiveness of that approach is clear provided a J_{sc} enhancement higher than 20% can be predicted using the modified transfer matrix model described in **Appendix A**.

In Chapter 2, we designed and implemented such TRTC configuration to reach an optimal light trapping in PSCs. We studied several specific configurations where the character of such two fundamental resonances co-exist leading to the broadband light trapping mentioned above. With the photon management provided by the TRTC, we report a PCE above 11.1%, when a high-performance PTB7-Th: PC₇₁BM organic cell is integrated within such cavity. This increase in PCE, equivalent to a J_{sc} increase larger than 2 mA/cm², is demonstrated to be achieved without any significant alteration of the other two photovoltaic parameters.

In Chapter 3, we considered the use of the TRTC configuration presented in chapter 2 to increase the J_{sc} in PSCs fabricated using a high V_{oc} non-fullerene active blend. When one combines the TRTC with a ternary blend, we demonstrated that one may achieve a broadband light absorption with a very limited reduction in the photovoltage. Indeed, only a small loss in V_{oc} is seen when the ITIC electron acceptor is partially substituted with PC₇₁BM to enhance the TRTC effect. In the same chapter we also show that such TRTC concept could be integrated on PET substrates, and truly flexible cells with excellent mechanical stability were demonstrated.

PSC will not become a commercial alternative unless the inherent low stability of the organic compounds or structures is addressed in parallel to the PCE increase. As noted above, the physics underlying degradation mechanisms are not fully understood. It is

Chapter 1. Introduction

quite obvious that there are many different parts of the cell which physical properties may be affected during operation, leading to a fatal degradation of the cell performance. Provided we cannot comprehensively address such problems within the scope of the current thesis, we focused our attention to alterations in the active layer, either in composition or in structure, which may end up leading to a degradation of the cell. Our aim was to understand the physics behind them and eventually propose and implement solutions that may circumvent such degradation paths and lead to more stable cells.

We focused our attention to the PTB7-Th:PC₇₁BM blend as active material because it is one of the most prominent active materials in PSCs, in addition, to have been considered, in many occasions, as one of the most easily degradable blends. Contrary to such prior results, in Chapter 4, we show that PTB7-Th:PC₇₁BM photoactive material is intrinsically stable under sun illumination when such material is isolated from the corrosive action of oxygen and moisture. We also demonstrated that an effective UV-induced removal of molecular oxygen chemisorbed on the sol-gel ZnO ETL, could improve the photostability of PTB7:PC₇₁BM solar cells.

In chapter 5, we systematically studied the origin of the burn-in loss in encapsulated PTB7-Th:PC₇₁BM cells under full sun illumination and proposed a novel explanation to unveil the physics behind the light-induced burn-in loss. We demonstrated that such burn-in is triggered by a spin flip occurring at the PC₇₁BM/polymer interface after a UV photon absorption, leading to the accumulation of electrostatic potential energy that initiates a rapid destruction of the nanomorphology in the fullerene phase of the polymer cell. We also provided an approach to circumvent this degradation path by introducing a highly ordered PC₇₁BM phase in the active layer. In that case, the burn-in loss of PTB7-Th:PC₇₁BM cells was significantly suppressed and device operational lifetime over 10 years was achieved.

Chapter 2

Broadband light trapping in thin film solar cells

To reach an optimal photon absorption in thin film photovoltaic devices, the sunlight should be effectively trapped in the absorber layer provided in the standard planar cell architecture a considerable portion of the photons is rejected or scattered out of such layer. An enhanced light-harvesting in the photoactive layer relative to a given reference cell has been observed in many cases when the planar cell configuration is altered, particularly, in, those cases where a 3-dimensional nanostructure has been incorporated. Examples include hexagonal arrays of nano-columns^{64,65} or nano-hole⁶⁶ embossed in the active layer, textured electrodes in a periodic grating^{67,68} or in a random configuration⁶⁹, nanospheres to couple light in the whispering gallery^{36,70,71}, and plasmonic nanoparticles embedded in the buffer layers or absorber layer^{44,46,72,73,74,75}. However, light trapping or confinement using the above mentioned nanostructures has never been shown to be critical in record performing thin film cells. In addition, some of such nanostructures may cause a major disruption in the nano-morphology or uniformity of the cell active layer, leading to a dramatic decrease in electrical properties of the device, such as FF and V_{oc} ^{65,76}.

As a general rule, the approach to optimize light trapping in thin film solar cells should be relatively easy to implement without sacrificing the cell electrical properties. To

Chapter 2. Broadband light trapping in thin film solar cells

fulfill the requirements, a 1-D planar configuration could be the optimal choice. A good example is in the photon-conversion semitransparent devices employing 1-D photonic crystals, previously reported by our group^{30,77,78,79}.

In this chapter, we discuss the implementation of a 1-D two-resonance tapping cavity (TRTC) that can be made to have a resonant character at two different frequencies, non-harmonic of each other, when adjusting the materials or geometry configurations of the partially transmitting cavity layers. We study specific configurations where the character of such two fundamental resonances co-exist leading to a broadband light trapping. We also study in detail the case where a high-performance PTB7-Th:PC₇₁BM organic cell⁸⁰ is integrated within such cavity. We analyze experimental results indicating that a power conversion efficiency of 11.1% can be reached. In Section 2.1, we firstly illustrate the TRTC concept and demonstrate how TRTC works, based on numerical simulations in the framework of the TMF described in Appendix A. Then, in the Section 2.2 we study the material- and architecture- dependence of the TRTC. Finally, in Section 2.3 we integrate the optimal TRTC to solar cells based on various polymer active layers to achieve their highest possible efficiencies.

2.1 Two-resonance tapping cavity concept

A standard optical cavity, usually formed by a high reflectance mirror (HRM) separated a fixed distance from another partially reflecting metallic cavity layer (MCL), can be made to resonate at a fundamental frequency and its harmonics. The separation between the MCL and the HRM combined with the refractive index of the filling material univocally determines such cavity fundamental resonant frequency. By adding a dielectric cavity layer (DCL) as can be seen in **Figure 2.1**, one may obtain a cavity that when decreasing the MCL thickness can be made to resonate at a new fundamental frequency lying in between the fundamental and the second harmonic of the MCL optical cavity.

Chapter 2. Broadband light trapping in thin film solar cells

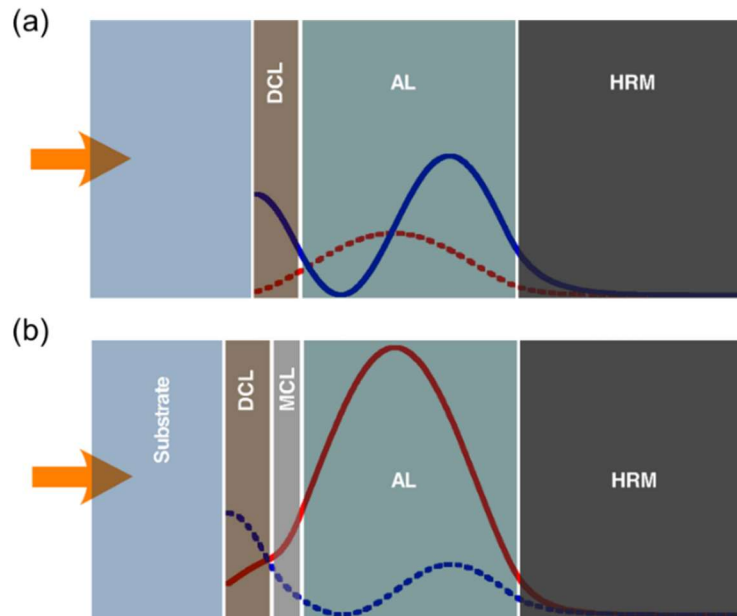


Figure 2.1. Schematic diagram of cavities formed by an active layer (AL) dispersion less layer ($n=2.0$ and $k=0$) sandwiched in between a DCL and a HRM (a), and by an AL sandwiched in between a DCL/MCL and a HRM (b). Blue and red curves correspond to field intensity distributions at 440 nm and 655 nm, respectively. The resonant field intensities are shown as solid lines while the non-resonant ones are shown as dashed.

Although such DCL sits at approximately the same distance the MCL is from the HRM, the boundary conditions for the electromagnetic field change drastically because the material changes from being a good quality conductor to a dielectric material. For a DCL cavity without a MCL, the boundary conditions are such that on the HRM side the resonant electrical field tends to vanish while on the DCL side the field amplitude takes a maximum value as seen in the top part of **Figure 2.1a**. When the MCL thickness is increased, at resonance the electrical field tends to vanish on both sides of the cavity, as seen in the bottom part of **Figure 2.1b**. The former case is somehow similar to the vibration of string fixed from one end and loose from the other one, while the latter one is similar to the vibration of a string fixed from both ends. Indeed, the confinement capacity provided by such two non-harmonic resonances of each other could be achieved with any type of wave provided the boundary conditions

Chapter 2. Broadband light trapping in thin film solar cells

set are similar to the ones that can be achieved when using the DCL and MCL combination. The difference in the boundary conditions is what allows to have two cavities with a very similar length and filled with the same index material, but resonating at two relatively close frequencies which are not subsequent harmonics of each other. When both the DCL and MCL are present and their thicknesses are fixed to some specific values that will be given in Section 2.2, the resulting cavity is non resonant at either one of the two frequencies, but at the same time light propagation within it has a reminiscence from both resonant frequencies. Light propagation in such new cavity we propose is analogous to the several cycles inharmonic vibration of a string during the transition of a note tapped by the right hand sustained or pulled off into a note fretted by the left hand in the two-handed tapping guitar playing technique. This is the reason why such type of optical cavity has been referred to as a two-resonance tapping cavity (TRTC)⁸¹.

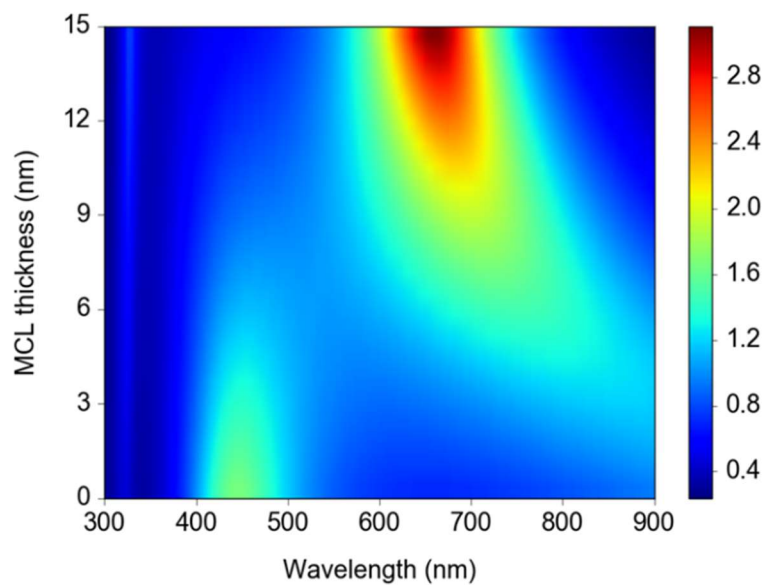


Figure 2.2. Computed field amplitude in a dispersion less ($n=2.0$ and $k=0$) AL as a function of the wavelength and MCL thickness. The device architecture used was MgF_2 (94 nm)/SK-10 substrate/DCL (20 nm)/MCL (0-15 nm)/AL (107 nm)/Ag (100 nm).

Chapter 2. Broadband light trapping in thin film solar cells

When a TRTC is formed with the DCL adjacent to the MCL by increasing the thickness of the latter layer from zero to any value above 10 nm one can switch the resonance from the DCL to the MCL fundamental frequencies, as seen in **Figure 2.2**. For intermediate MCL thicknesses, between 5 and 10 nm approximately, the field confinement effect from both fundamental resonances is smeared but the character from both resonances survives leading to a broadband light trapping. Note that this is fundamentally different than an anti-reflection coating that relies on achieving a high transmission via an optimal electromagnetic interference. The effectiveness in the light confinement provided by such TRTC is demonstrated by the observation of an increased light absorption.

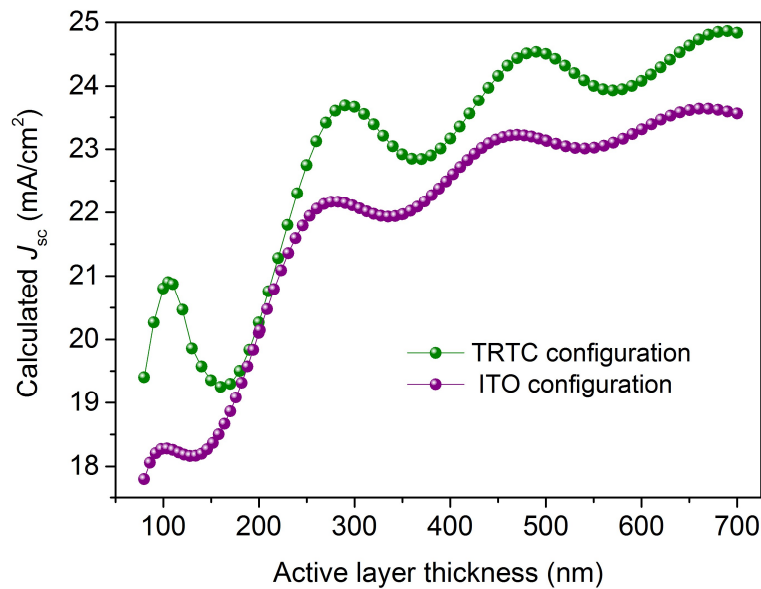


Figure 2.3. Predicted optimal short-circuit current as a function of the AL thickness in a standard ITO configuration cell (purple) or in TRTC configurations (olive). Here, the AL is a semiconductor material with a constant value of $n = 2.0$.

To evaluate the dependence of the TRTC effect in terms of the thickness of the active layer, we consider a simple thin film solar cell configuration where the absorber material is a “semiconductor” material exhibiting a square root growth for the density of states in terms of the excitation energy above the band gap. In this evaluation, variations in the real part of the refractive index are neglected. As seen in **Figure 2.3**,

Chapter 2. Broadband light trapping in thin film solar cells

for such type of material light collection can be, for certain sizes of the absorber layer, more than 2.5 mA/cm² larger for the TRTC configuration than for the standard ITO cell configuration. This simulation results suggest that TRTC is a general approach that, in principle, can be applied to any kind of thin film photovoltaic device to reach optimal performances.

2.2 Materials and architectures for TRTC-based cells

In this section we consider the implementation of the TRTC for the specific case where the PTB7-Th:PC₇₁BM polymer blend is used as the absorber layer. In the study carried out in this Section 2.1, we present numerical computations that can be used to design the optimal TRTC, but always considering the experimental constraints. For instance, the materials that may be used in the DCL or the inclusion of layers which are not relevant to achieve the optimal TRTC but that must be included to, for instance, obtain a MCL in the optimal conditions.

In such implementation of the TRTC, the absorber layer is enclosed in between a 100 nm thick Ag HRM and the DCL/MCL. The MCL consisting of a 10 nm thick Ag layer sandwiched between two 5 nm ZnO layers. Although neither of such two ZnO layers plays any relevant optical role, in an experimental implementation of the TRTC, the bottom one would be needed to optimize the transmission and electrical properties of the thin Ag layer, while the top one would prevent any Ag degradation in the event that such electrode is exposed to the ambient air^{82,83}. For the DCL, adjacent to the bottom ZnO layer, we analyze four different dielectric inorganic materials with high transparency in the visible region of the spectrum: Al₂O₃, ZnO, MoO₃ and TiO₂. Their corresponding refractive indexes are shown in **Figure 2.4a**.

Chapter 2. Broadband light trapping in thin film solar cells

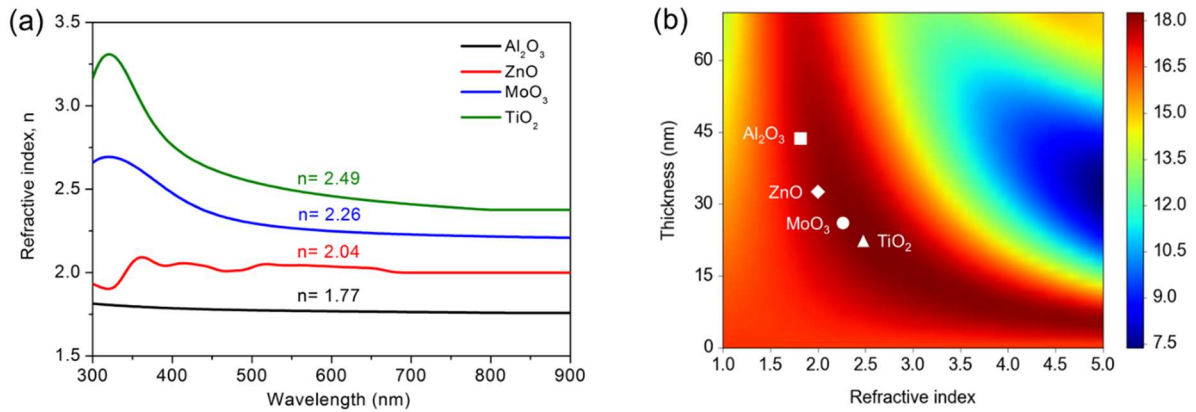


Figure 2.4. (a) Refractive index of dielectric cavity materials: Al₂O₃, ZnO, MoO₃ and TiO₂. (b) Numerically computed short-circuit current (color bar) as a function of DCL refractive index and thickness when the AL material is the PTB7-Th: PC₇₁BM blend. The optimal DCL for the dielectric materials used in the experiments are indicated: Al₂O₃ (square), ZnO (diamond), MoO₃ (circle), and TiO₂ (triangle). Internal quantum efficiency (IQE) here for simulations is assumed to be 90%.

As can be seen in Figure 2.4b, a maximum short-circuit current is predicted for the higher refractive index materials such as the TiO₂ or MoO₃. The optimal DCL thickness must be selected in each case to maximize the J_{sc} in accordance to Figure 2.4b. As expected, when the refractive index of the DCL increases, the resonance corresponding to that layer becomes sharper, as shown in **Figure 2.5a**. When this is combined with a 10 nm Ag thickness for the MCL, one achieves a remarkable two-resonance tapping effect for the MoO₃ and TiO₂ cases. As seen in Figure 2.5b, in both cases, the MCL or DCL fundamental resonances are smeared and become barely distinguishable. In contrast, the standard resonant cavity formed without the DCL layer exhibits the usual single sharp resonance (see Figure 2.5b).

Chapter 2. Broadband light trapping in thin film solar cells

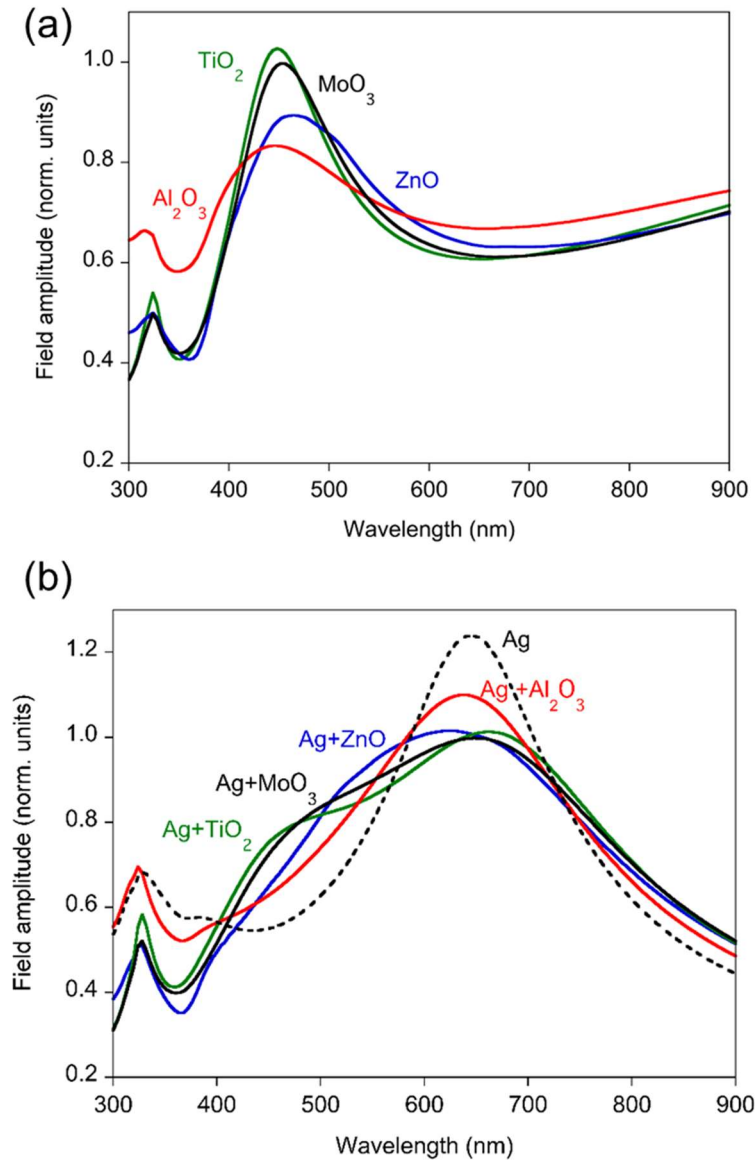


Figure 2.5. Optical field amplitude in the AL layer as a function of the wavelength for (a) DCL and (b) DCL/MCL. The AL here is a non-absorbing dielectric with a refractive index real part equal to 2.0 and the Ag MCL thickness is taken to be 10 nm, and the DCL materials are Al_2O_3 (red solid line), MoO_3 (black solid line), ZnO (blue solid line) and TiO_2 (green solid line).

To evaluate what effect does the predicted confinement, shown in Figure 2.5b, have on the light absorption by the polymer blend, we numerically computed the EQEs of completed cell architectures. The exact thicknesses for each DCL layer (given in **Table 2.1**) was determined numerically using the transfer matrix model outlined in the

Chapter 2. Broadband light trapping in thin film solar cells

optical simulation section from the introduction chapter. We used an inverse integration approach to find the optimal cell configuration that maximizes the J_{sc} . The numerically computed EQEs that maximize the J_{sc} are shown in **Figure 2.6** for the four different DCL materials under consideration.

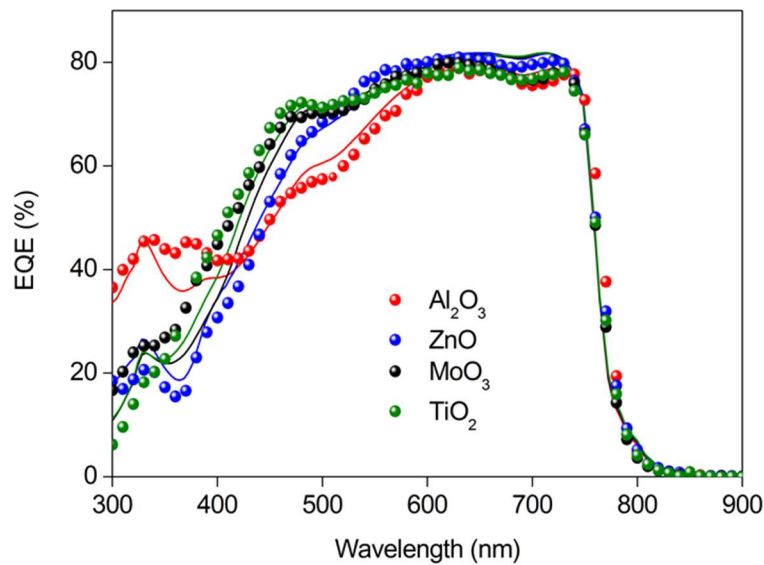


Figure 2.6 Experimentally measured (dots) and simulated (solid lines) EQEs for PTB7-Th:PC₇₁BM TRTC cells based on the above four DCL materials with predicted optimal thickness.

Such numerical predictions are compared to experimentally measured EQEs from cells fabricated when the ITO electrode is replaced by the DCL/MCL combination. In such experimental implementation all DCL and MCL materials are deposited by magnetron sputtering at room temperature. Fabrication details are given in **Appendix B**. The fabricated device architectures consisted of fused silica substrate/DCL/ZnO (5 nm)/MCL/ZnO (5 nm)/sol-gel ZnO (SG-ZnO, 10 nm)/PTB7-Th: PC₇₁BM (95 nm)/MoO₃ (5 nm)/Ag (100 nm). The measured Photovoltaic parameters are all given in Table 2.1. When the corresponding experimentally measured EQEs are compared to the computed ones in **Figure 2.6**, one clearly sees that the TRTC obtained when the material of the DCL is either MoO₃ or TiO₂ the broadband absorption is optimal. Such EQEs indicate a strong absorption in the green-red spectral regions for all cases, extending to the blue region when the refractive index of DCL material is larger.

Chapter 2. Broadband light trapping in thin film solar cells

Table 2.1 Photovoltaic properties of inverted PTB7-Th: PC₇₁BM devices employing various TRTC configurations under AM 1.5G solar illumination at 100 mW cm⁻².

DCL material	Thickness (nm)	J_{sc} (mA cm ⁻²)	V_{oc} (V)	FF (%)	PCE (%)
Al ₂ O ₃	44	17.54 ± 0.25	0.800 ± 0.001	73.1 ± 0.4	10.25 ± 0.14 (10.43)
ZnO	33	17.96 ± 0.20	0.800 ± 0.001	73.4 ± 0.7	10.56 ± 0.09 (10.69)
MoO ₃	26	18.29 ± 0.20	0.796 ± 0.001	73.2 ± 0.3	10.66 ± 0.10 (10.78)
TiO ₂	19	18.45 ± 0.13	0.797 ± 0.001	72.9 ± 0.5	10.72 ± 0.11 (10.86)

Device structure here is fused silica substrate /DCL/ZnO (5 nm)/MCL/ZnO (5 nm)/SG-ZnO (10 nm)/AL (95 nm)/MoO₃ (5 nm)/Ag (100 nm) with MCL Ag (10 nm). The average values and standard deviations were obtained from over 10 devices and the value in the parentheses corresponds to the best devices.

Once the material for the DCL is selected, one can find an optimal performance for the TRTC cell is by adjusting the DCL as well as the MCL thickness. As seen in **Figure 2.7a**, an almost wavelength independent EQE covering the entire absorption band of the PTB7-Th: PC₇₁BM blend is found for a 19 nm TiO₂ DCL. Similarly, if the contribution to the optical resonance of the MCL is diminished by reducing the Ag layer thickness within the MCL, one observes, as seen in Figure 2.7b, that the EQE is reduced in the green to near IR range of the spectrum. The corresponding PV parameters are given in **Table 2.2**.

Chapter 2. Broadband light trapping in thin film solar cells

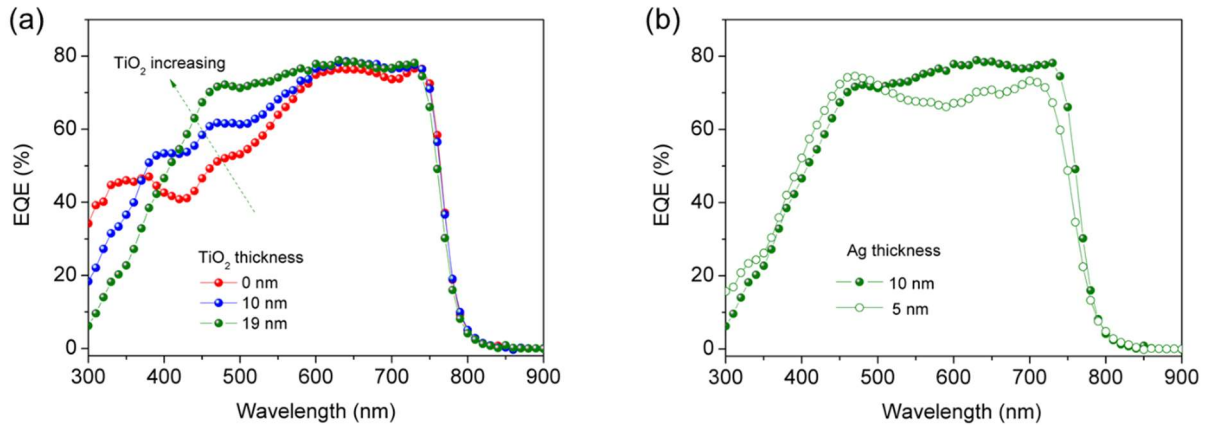


Figure 2.7. Experimentally measured (dots) and computed (solid lines) EQEs for the devices of fused silica/DCL/ZnO (5 nm)/MCL/ZnO (5 nm)/SG-ZnO (10 nm)/PTB7-Th:PC₇₁BM (95 nm)/MoO₃ (5 nm)/Ag (100 nm). (a) The MCL is fixed to a 10 nm Ag layer and the DCL corresponds to a TiO₂ layer of 0 nm (red dots), 10 nm (dots), and 19 nm (green dots) in thickness. (b) The DCL is fixed to a 19 nm TiO₂ layer and the MCL corresponds to an Ag layer with 5 nm (purple) and 10 nm (green) thickness.

Table 2.2. Thickness of DCL and Ag in MCL dependent solar cell properties of PTB7-Th:PC₇₁BM devices under AM 1.5G solar illumination at 100 mW cm⁻². DCL and MCL here are TiO₂ and ZnO (5 nm)/Ag/ZnO (5 nm), respectively.

Configuration	J_{sc} (mA cm ⁻²)	V_{oc} (V)	FF (%)	PCE (%)
DCL (0 nm)/MCL (10 nm)	17.54 ± 0.27	0.794 ± 0.001	72.0 ± 0.5	10.04 ± 0.10 (10.17)
DCL (10 nm)/MCL (10 nm)	18.22 ± 0.16	0.795 ± 0.002	72.1 ± 0.3	10.45 ± 0.10 (10.51)
DCL (19 nm)/MCL (5 nm)	17.03 ± 0.16	0.798 ± 0.002	69.2 ± 0.8	9.41 ± 0.16 (9.61)
DCL (19 nm)/MCL (10 nm)	18.50 ± 0.21	0.795 ± 0.005	72.1 ± 0.9	10.62 ± 0.30 (10.86)

2.3 Design of optimal thin-film solar cells incorporating a TRTC

Light harvesting in a TRTC cell can be further enhanced if the effect of the TRTC is combined with a reduced light reflection at the substrate by introducing an anti-reflection coating (ARC). In that event, one may achieve the largest enhancement for the light absorption in a cell configuration that remains 1-D.

As seen in Figure 2.3, when the active layer thickness is around 100 nm in TRTC configuration, we observe a significant enhancement in J_{sc} as compared to corresponding ITO reference cells. The calculated EQEs when the photoactive material is a 100 nm thick PTB7-Th:PC₇₁BM polymer blend layer are shown in **Figure 2.8**. One sees that the TRTC has the effect of increasing the EQE for wavelengths from the visible to near infrared spectrums.

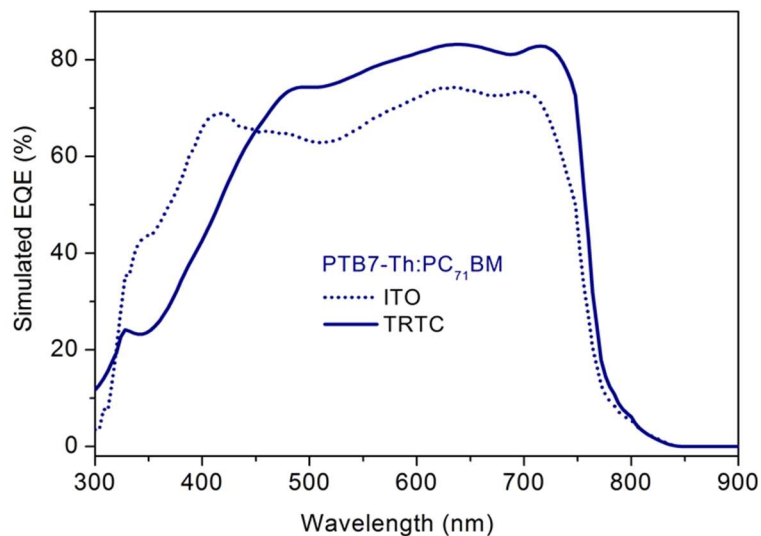


Figure 2.8. Simulated EQEs for PTB7-Th: PC₇₁BM active layer employing the standard ITO (dot line) and the TRTC (solid line) configurations. The TRTC cell architectures used were: MgF₂ (100 nm)/SK10 substrate/TiO₂ (19 nm)/ZnO (5 nm)/Ag (9.6 nm)/ZnO(5 nm)/SG-ZnO(5 nm)/PTB7-Th: PC₇₁BM (96 nm)/MoO₃ (5 nm)/Ag (100 nm).

Chapter 2. Broadband light trapping in thin film solar cells

The entire architecture is shown in **Figure 2.9a**. As indicated above, to determine the thickness for all layers, as well as the optimal index for the substrate we implemented an inverse solving approach using a modified transfer matrix method (see chapter 1.3) that combines the coherent superposition of field amplitudes within the ARC and cell layers with the superposition of field intensities within the substrate layer.

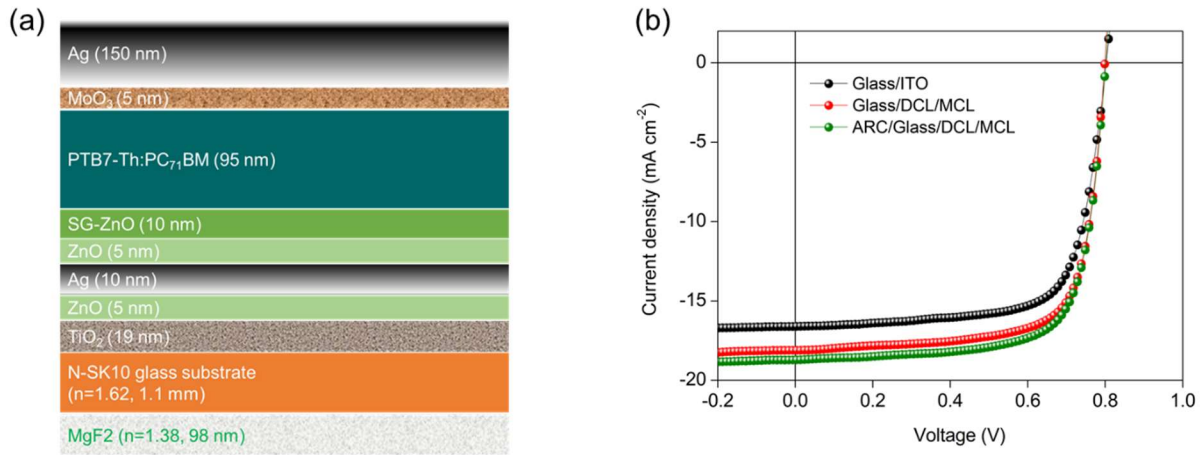


Figure 2.9. (a) Optimal PTB7-Th: PC₇₁BM device configuration employing the TRTC. (b) J - V characteristics when measured under AM 1.5G illumination at 100 mW/cm².

Using such modified transfer matrix method we numerically determined the maximum J_{sc} to be close to 18.9 mA/cm² for the following architecture: MgF₂ (100 nm)/N-SK10 substrate/DCL/ZnO(5 nm)/MCL/ZnO(5 nm)/SG-ZnO(10 nm)/PTB7-Th: PC₇₁BM (95 nm)/MoO₃ (5 nm)/Ag (100 nm). Here DCL and MCL are made of 19 nm thick TiO₂ and 10 nm thick Ag, respectively. As noted above the contribution from the MCL and DCL resonances is smeared when the Ag thickness is in the 5 to 10 nm range. The combined effect of the wavelength dependence in the solar spectrum and in the blend absorption pushes the optimal cell architecture towards a 10 nm thick MCL, favoring the MCL resonance over the DCL. The TRTC cells, with or without the ARC, exhibit a higher J_{sc} than the ITO cell as can be seen in Figure 2.9b. With the TRTC the averaged PCE increases from 9.33% (reference ITO cell) to 10.62% and further increases to 11.01% when the ARC is incorporated. One of the highest PTB7-Th:

Chapter 2. Broadband light trapping in thin film solar cells

PC₇₁BM TRTC cells were independently tested at Newport laboratory that certified a PCE of $10.4 \pm 0.23\%$. The increase in PCE here mainly originates from the enhancement in J_{sc} that jumps by more than 2 mA/cm^2 from 16.53 mA/cm^2 to 18.74 mA/cm^2 as shown in **Table 2.3**. Note that the enhancement in J_{sc} is achieved without sacrificing FF and V_{oc} . Indeed, as seen in Table 2 the TRTC devices exhibited higher FF s than ITO counterparts mainly due to a reduced average series resistance. This is consistent with a lower sheet resistance of $5.4 \text{ } \Omega/\text{sq}$ in the MCL based electrodes as compared to $15 \text{ } \Omega/\text{sq}$ for the ITO electrode.

Table 2.3 Photovoltaic parameters of ITO and TRTC based solar cells under AM 1.5G solar illumination at 100 mW cm^{-2} .

Cell configuration	J_{sc} (mA cm^{-2})	V_{oc} (V)	FF (%)	PCE (%)	R_s (Ω)	R_p ($\text{k}\Omega$)
Glass/ITO	16.53 ± 0.22	0.790 ± 0.006	71.1 ± 0.1	9.33 ± 0.16 (9.60)	64.3	18.7
Glass/DCL/MCL	18.09 ± 0.13	0.800 ± 0.002	73.3 ± 0.3	10.62 ± 0.11 (10.53)	31.0	21.3
ARC/Glass/DCL/MCL	18.74 ± 0.17	0.802 ± 0.002	73.0 ± 0.3	11.01 ± 0.09 (11.13)	32.1	23.8

ARC corresponds to MgF_2 (100 nm) while the DCL/MCL structure incorporates two ZnO layers is TiO_2 (19 nm)/ZnO (5 nm)/Ag (10 nm)/ZnO (5 nm).

Chapter 2. Broadband light trapping in thin film solar cells

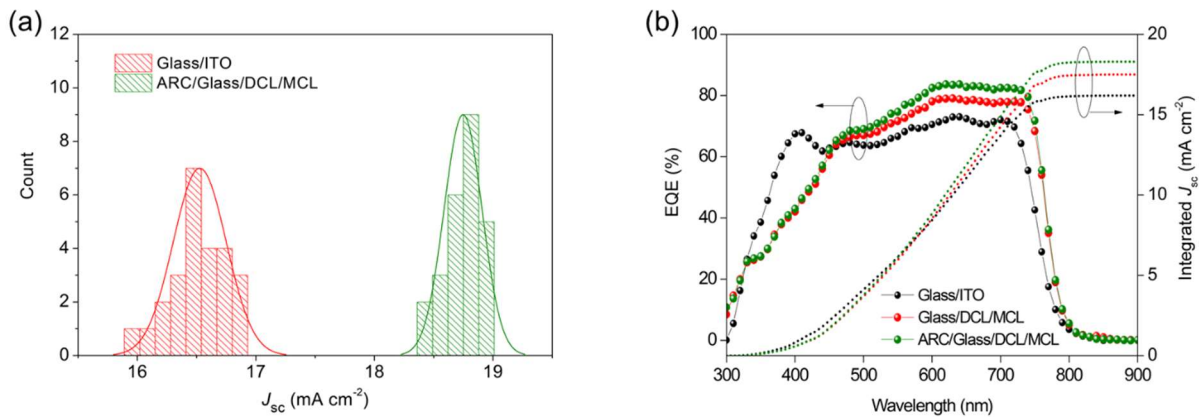


Figure 2.10. (a) J_{sc} distribution for 25 ITO reference devices (red bars) and for 25 ARC/TRTC devices (green bars). The solid lines represent the Gaussian distribution fittings. (b) Experimentally measured EQE and intergrated J_{sc} from EQE curves for the ITO cell (black), and the TRTC cell in a) with (green) and without (red) the ARC.

The J_{sc} distributions shown in **Figure 2.10a** demonstrate the reliability and reproducibility of the J_{sc} enhancement provided by the TRTC. When comparing the EQE of the three cells shown in **Figure 2.10b**, we observe that the TRTC leads to an enhancement in the photon absorption for almost the entire wavelength range except at shorter wavelengths where the absorption of the materials used in MCL and/or in DCL is larger than the absorption of ITO. In addition, the EQE profile for both TRTC cases is slightly higher towards the IR rather than the UV side. Although the TRTC can provide an almost wavelength independent flat photon absorption, this changes when the TRTC is designed to optimize the performance of a solar cell. In other words, the larger sun photon flux in the 700 to 800 nm range combined with the PTB7-Th:PC₇₁BM absorption leads the inverse numerical optimization targeting the maximum J_{sc} , to yield an EQE that prioritizes an IR shifted photon absorption. Note that all EQEs were previously computed using the inverse integration approach to maximize J_{sc} and, once the entire layer architecture was known, fabrication of the devices was carried out.

Chapter 2. Broadband light trapping in thin film solar cells

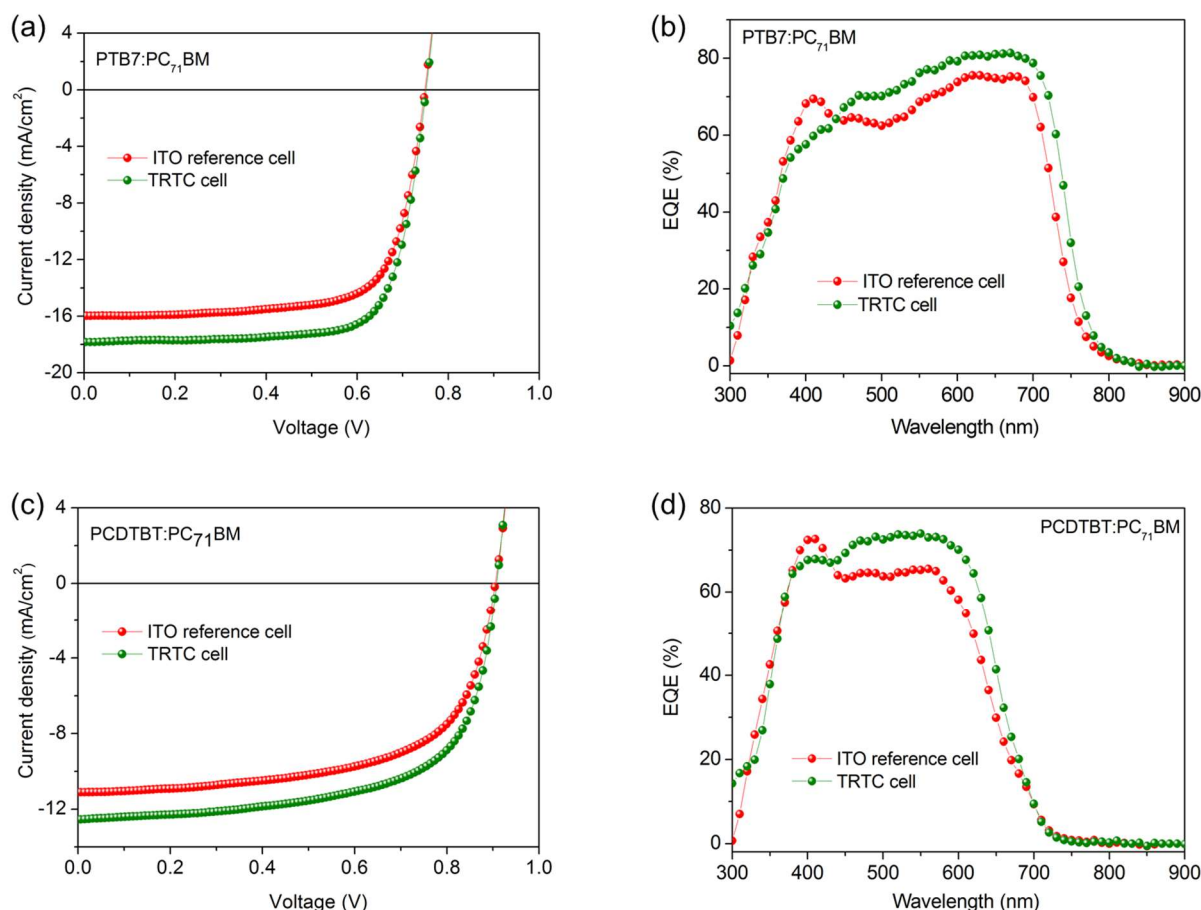


Figure 2.11. $J-V$ (a) and EQE (b) curves of PTB7:PC₇₁BM inverted solar cells employ ITO and TRTC configurations. $J-V$ (c) and EQE (d) curves of PCDTBT:PC₇₁BM using standard ITO and TRTC electrodes.

Top PCEs can be obtained irrespective of the polymer blend used as can be seen in **Figure 2.11**, where PTB7-Th is substituted by the Poly[[4,8-bis[(2-ethylhexyl)oxy]benzo[1,2-b:4,5-b']dithiophene-2,6-diyl][3-fluoro-2-[(2-ethylhexyl)carbonyl]thieno[3,4-b]thiophenediyl]] (PTB7) or Poly[N-9'-heptadecanyl-2,7-carbazole-alt-5,5-(4',7'-di-2-thienyl-2',1',3'-benzothiadiazole)] (PCDTBT) polymer. Both polymer based TRTC devices show ~15% enhancement relative to the optimal ITO reference cells. The detailed PV parameters are summarized in below **Table 2.4**.

Chapter 2. Broadband light trapping in thin film solar cells

Table 2.4. Photovoltaic parameters of ITO and TRTC based solar cells under AM 1.5G solar illumination at 100 mW cm^{-2} . TRTC cells fabricated using MgF_2 (100 nm)/SK-10 substrate/ TiO_2 (19 nm)/ ZnO (5 nm)/Ag (10 nm)/ ZnO (5 nm) electrodes.

Active layer	Structure	J_{sc} (mA cm^{-2})	V_{oc} (V)	FF (%)	PCE (%)
PTB7:PC ₇₁ BM	ITO	16.09 ± 0.11	0.747 ± 0.001	72.1 ± 1.4	8.67 ± 0.19 (8.86)
	TRTC	17.79 ± 0.09	0.750 ± 0.001	72.9 ± 0.9	9.72 ± 0.12 (10.04)
PCDTBT:PC ₇₁ BM	ITO	11.08 ± 0.12	0.917 ± 0.002	62.3 ± 0.8	6.33 ± 0.14 (6.50)
	TRTC	12.43 ± 0.20	0.910 ± 0.004	64.2 ± 0.4	7.26 ± 0.12 (7.43)

2.4 Conclusions

In this chapter, we studied a new type of 1-D optical cavity that can be used to enhance the performance of thin film cells. Contrary to the common believe that dielectric layers would act as simple anti-reflection coatings, we demonstrate that the combination of an insulator with a good conductor leads to the formation of an optical cavity that can be made to have a resonant character at two non-harmonic frequencies of each other. The increase in energy storage capacity relies, precisely, in the inharmonic character of the electromagnetic field propagation within such cavity.

We selected four different inorganic transparent materials with different refractive index for the DCL and demonstrated that thinner films are needed for higher refractive index materials to reach an optimal TRTC-based solar cell. We showed that TiO_2 is one of the best materials to construct such TRTC due to its high index amongst transparent inorganic materials.

We also demonstrated that the energy confinement capacity seen remains even when the material composition is changed or the thickness of the active layer is increased,

Chapter 2. Broadband light trapping in thin film solar cells

and can, in principle, be applied to reach efficiency limit performances for any kind of thin film photovoltaic device. Moreover, this effect is more pronounced for photoactive materials where their absorption band exhibit a large wavelength dependent absorption, for instance, in organic materials or metal halide perovskites.

Chapter 3

High-performance flexible PSCs using a TRTC electrode

Solar cells with PCEs higher than 11% were demonstrated in Chapter 2 using a TRTC configuration to achieve a broadband light absorption enhancement in the active material absorption spectrum. Given such optimal light absorption in active layers that are just 100 nm thick combined with fill factors that are close to 80%, further improvements in PCEs should rely mainly on material, layer morphology or cell configuration changes that have a direct impact on the V_{oc} . Synthesis of new acceptors with an elevated lowest unoccupied molecular orbital (LUMO) energy level is an effective way to achieve higher V_{oc} s. Indeed, emerging non-fullerene molecular or polymeric acceptors have been successfully employed to achieve higher V_{oc} s compared to those of analogous PC₇₁BM devices^{84,85,86,87,88,89,90,91}. However, many such high V_{oc} solar cells suffer from a reduced J_{sc} , which eventually limits the overall device performance.

To properly address the trade-off between V_{oc} and J_{sc} in high-performance polymer absorbers, most of the current strategies rely on molecular engineering^{14, 92, 93}, multicomponent blends control^{94,95} or device optimization⁹⁶. Such approaches have achieved a partial success and the PCE has been boosted to higher levels, but the

Chapter 3. High-performance flexible PSCs using a TRTC electrode

aforementioned strategies normally lack the desired level of generality. For instance, they are restricted to chemical modifications for optimizing the molecular energy level of acceptor materials. Therefore, a comprehensive approach that simultaneously encompasses photocurrent as well as V_{oc} enhancements is needed.

In this chapter we consider the use of the TRTC cavity presented in chapter 2 to reach a high short circuit current in cells fabricated using a high V_{oc} PBDBT:ITIC active blend. When one combines the TRTC with a ternary blend, one may achieve a broadband light absorption without a significant reduction in the photovoltage. Indeed, only a small loss in V_{oc} is seen when the ITIC electron acceptor is partially substituted with PC₇₁BM to enhance the TRTC effect leading to a broadband absorption. To reach the optimal balance between open circuit voltage and short circuit current, in Section 3.1 we study the optical properties of ITIC and PC₇₁BM and the evolution of PBDBT:ITIC:PC₇₁BM ternary blend films. Then, in Section 3.2 we implement the optimal ternary active layer into the TRTC and investigate the cavity effect on the PC₇₁BM addition. Finally, we consider the performance of such cells in other aspects besides the efficiency, which are very relevant to a possible technology transfer. In Section 3.3 the TRTC cell is fabricated on a PET substrate to obtain flexible cells and the results of mechanical bending stability tests are reported, while in Section 3.4 we study the thermal stability of the cells with and without PCBM doping.

3.1 Optical properties of ITIC and ternary PBDBT:ITIC:PC₇₁BM blend films

Unlike fullerene derivatives, ITIC acceptors⁸⁵ exhibit a very large extinction coefficient (k) peaked at ~705 nm, as seen in **Figure 3.1a**, which partially overlaps with the PBDBT polymer absorption in the 550–700 nm range. This leads to a strong and localized absorption in the red and near-infrared combined with a limited absorption on the blue side of the spectrum. For this reason, relatively high k values >

Chapter 3. High-performance flexible PSCs using a TRTC electrode

0.7 are expected on the red side of the spectrum for such non-fullerene blend, as seen in Figure 3.1b.

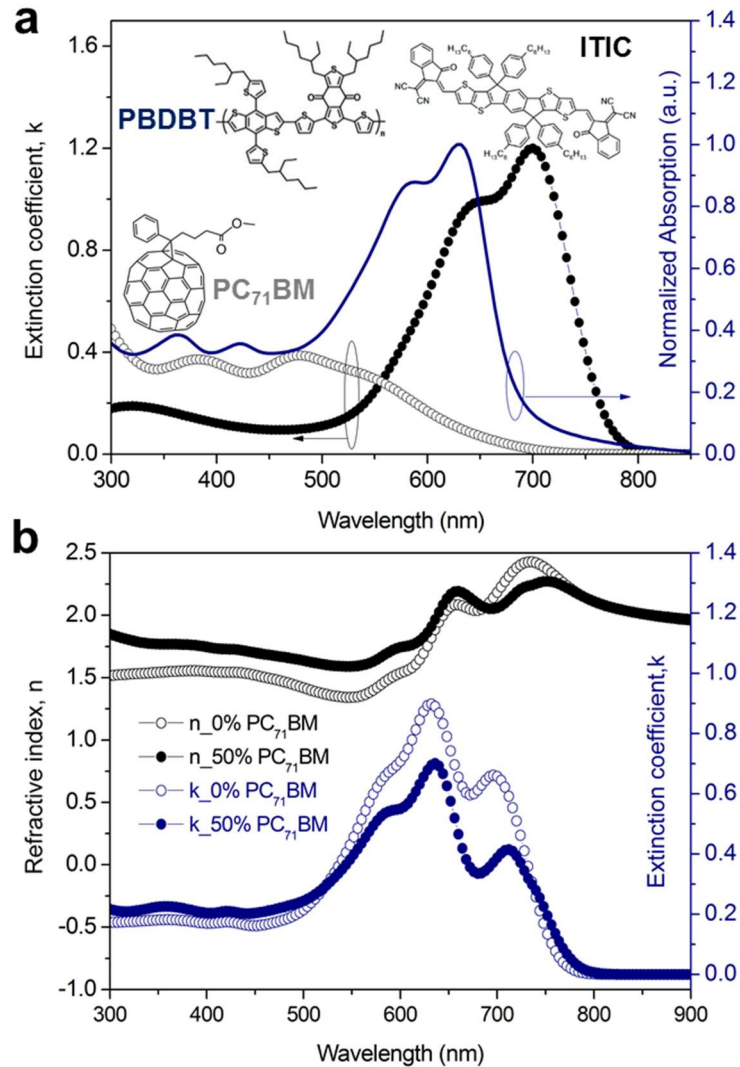


Figure 3.1. (a) Extinction coefficient (k) of PC₇₁BM (open circle) and ITIC (solid circle) and normalized absorption of PBDBT polymer (right axis). Inset is the molecular structure of the polymer and acceptors. (b) Optical constants for PBDBT:ITIC (non-PC₇₁BM) and PBDBT:ITIC:PC₇₁BM (1:0.5:0.5, 50% PC₇₁BM) blend films.

A relatively low k value on the blue side of the spectrum implies that integrating a PBDBT:ITIC in a TRTC would not provide the broadband absorption that is

Chapter 3. High-performance flexible PSCs using a TRTC electrode

characteristic of such optical cavity. To properly address this shortcoming, PC₇₁BM was introduced into the non-fullerene binary blend, while the donor/acceptor ratio was kept at 1:1. In such way the k value of the blend film could be finely tuned. The absorption evolution of the PBDBT:ITIC:PC₇₁BM ternary films with different PC₇₁BM contents is shown in **Figure 3.2a**.

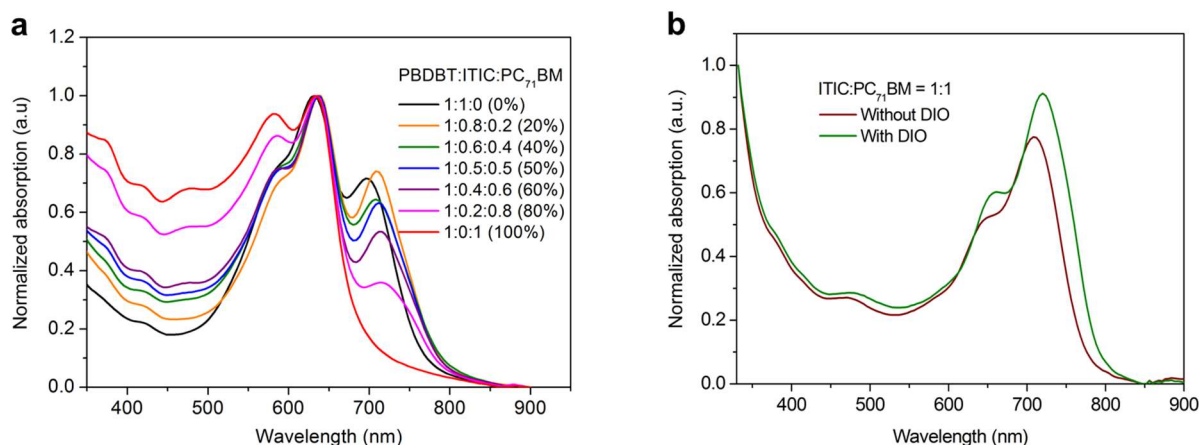


Figure 3.2. (a) Normalized absorption spectra of PBDBT:ITIC:PC₇₁BM ternary blend films with various PC₇₁BM fractions. (b) Normalized absorption of ITIC:PC₇₁BM films with and without 1% (vol %) DIO additive.

With increasing the PC₇₁BM fraction, the ternary blend absorption gradually enhances in the blue region, while it gets reduced in the near-infrared wavelengths. It is interesting to note that the PC₇₁BM-based blend absorption edges are red shifted relative to the non-fullerene one. This effect is attributed to the DIO additive-induced molecular interactions between ITIC and PC₇₁BM, as shown in **Figure 3.2b**. This provides a wider overlap with the solar spectrum and an enhanced infrared photon harvesting in the ternary devices. For the optimal ternary blend PBDBT:ITIC:PC₇₁BM = 1:0.5:0.5 (named "50% PC₇₁BM" from now on), k is clearly reduced in the 550-750 nm range compared to the non-fullerene blend film, and the maximum value decreases from 0.7 to 0.4, as can be seen in Figure 1b. All optical constants are shown in Appendix B.

3.2 High performance non-fullerene blend based TRTC cells.

The numerically computed short circuit currents as a function of the active layer thickness for both ITO and TRTC configurations are compared in **Figure 3.3a** when using non-fullerene and 50% PC₇₁BM blends. As expected, when a non-fullerene blend is used, a negligible gain in J_{sc} is achieved for the TRTC when compared to the ITO configuration. In contrast, numerical calculations show a J_{sc} increase by more than 1.2 mA/cm² for the ITO device (integrated J_{sc} =15.6 mA/cm²) when employing a 50% PC₇₁BM blend. As seen in Figure 3.4a, this current density can be further enhanced up to ~18 mA/cm² when employing the TRTC configuration. Note that the active layer thickness used for simulation purposes was kept under 140 nm in order to limit possible electrical losses common in organic cells when the active layer thickness departs significantly from 100 nm. The experimental EQEs shown in Figure 3.3b, as well as the integrated J_{sc} values given in **Table 3.1**, clearly demonstrate that the TRTC combined with a ternary blend having 50% PC₇₁BM leads to an optimal broadband light absorption.

Chapter 3. High-performance flexible PSCs using a TRTC electrode

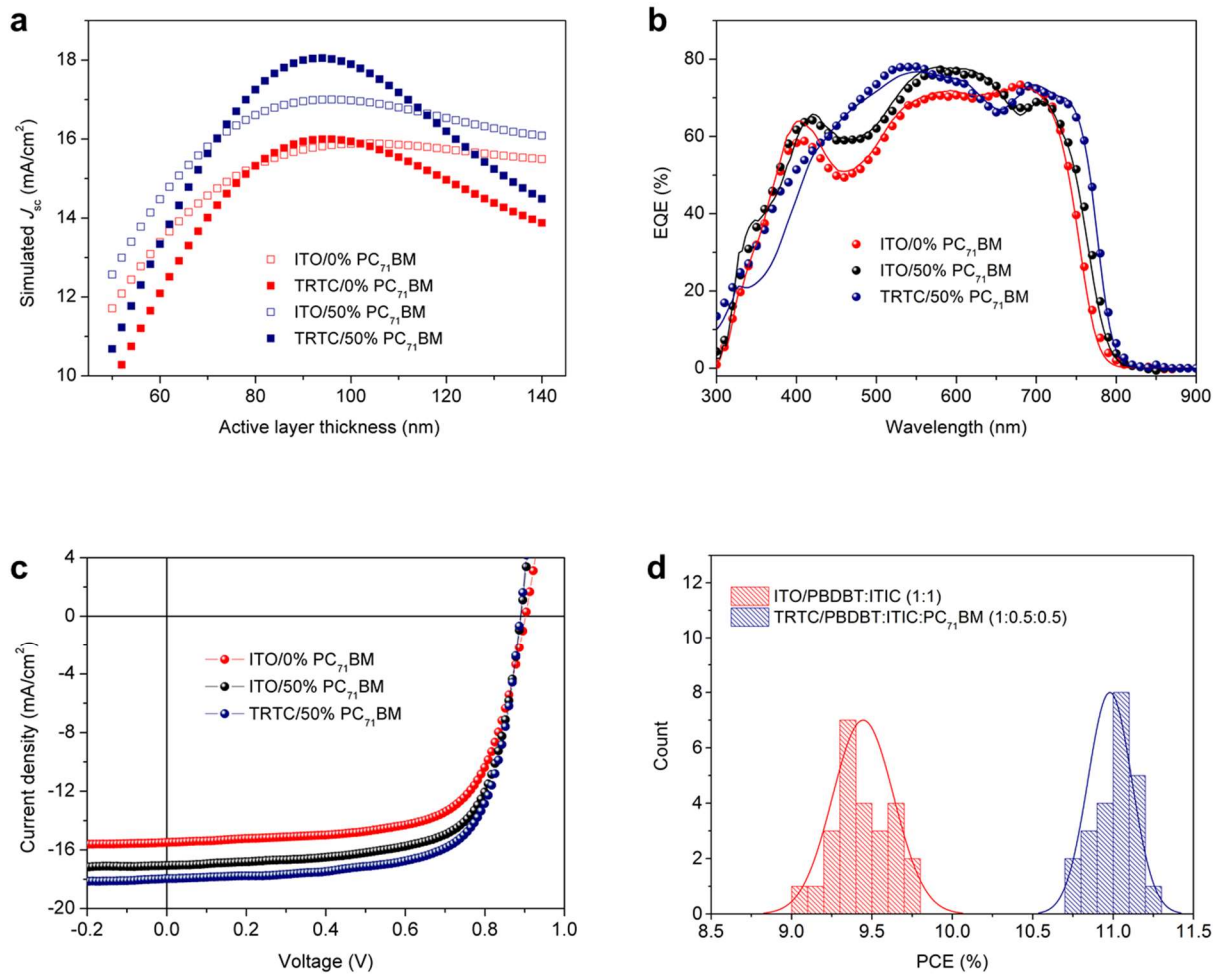


Figure 3.3. (a) Numerically computed J_{sc} under 100 mW/cm² illumination of AM 1.5G solar spectrum as function of active layer thickness for ITO and TRTC configurations using 0% and 50% PC₇₁BM blends, respectively. (b) Experimentally measured (dots) and computed (solid lines) EQEs for standard ITO cells with non-PC₇₁BM blends (red dots), 50% PC₇₁BM (black dots), and TRTC cells using 50% PC₇₁BM blends (blue dots). Note that the devices were fabricated according to the numerically computed cell architectures giving maximum J_{sc} . (c) Current density-voltage ($J-V$) curves of the corresponding cells measured under AM 1.5G illumination at 100 mW cm⁻². (d) PCE distribution for non-fullerene ITO devices (red bars) and 50% PC₇₁BM TRTC cells (blue bars) based on 30 devices for each. The solid lines represent the Gaussian distribution fittings. The TRTC cell configuration is MgF₂ (100 nm)/SK10 glass/TiO₂ (18nm)/ZnO (5 nm)/Ag (9 nm)/ZnO (3 nm)/SG-ZnO (10 nm)/active layer (95-100 nm)/MoO₃ (5 nm)/Ag (100 nm).

Chapter 3. High-performance flexible PSCs using a TRTC electrode

Table 3.1. Photovoltaic properties of inverted PBDBT:ITIC:PC₇₁BM ternary solar cells employing ITO and TRTC configurations under AM 1.5G solar illumination at 100 mW cm⁻².

Configuration	Active layer	J_{sc} (J_{EQE}) ^{a)} (mA cm ⁻²)	V_{oc} (V)	FF (%)	PCE ^{b)} (%)
ITO	PBDBT:ITIC (1:1)	15.44 ± 0.16 (15.60)	0.903 ± 0.002	67.7 ± 1.5	9.43 ± 0.21 (9.76)
ITO	PBDBT:ITIC:PC ₇₁ BM (1:0.5:0.5)	17.01 ± 0.12 (16.83)	0.886 ± 0.004	68.8 ± 0.6	10.37 ± 0.15 (10.65)
TRTC	PBDBT:ITIC:PC ₇₁ BM (1:0.5:0.5)	17.84 ± 0.12 (17.88)	0.882 ± 0.006	69.8 ± 0.5	10.98 ± 0.17 (11.22)

^{a)} Calculated from EQE spectra. ^{b)} The average values and standard deviations are obtained from over 20 devices and the best PCE values are shown in the parentheses. TRTC here presents MgF₂ (100nm)/SK10 glass /TiO₂ (18 nm)/ZnO (5 nm)/Ag (9 nm)/ZnO (3 nm).

Current density-voltage (J - V) characteristics of the ITO and TRTC based cells with different PCBM percentages, measured under AM1.5G illumination at 100 mW cm⁻², are shown in Figure 3.3c. The TRTC cell using 50% PC₇₁BM blend exhibited a 2.4 mA cm⁻² higher J_{sc} than its non-fullerene ITO counterpart. A best efficiency of 11.2% for the ternary TRTC cell was obtained, which is about 15% higher than the best non-fullerene ITO cell, as indicated in **Table 3.1**. To demonstrate the reproducibility of such approach, over 25 non-fullerene based ITO and 50% PC₇₁BM based TRTC cells were fabricated. The PCE distributions presented in Figure 3.3d demonstrate the good reliability and reproducibility of the approach.

To shed more light into the higher photocurrent of the 50% PC₇₁BM ternary blend compared to the non-fullerene one in the ITO configuration, the electrical field intensity ($|E|^2$) distribution inside the active layer and the internal quantum efficiency (IQE) were also evaluated. From the field intensity contour plot of **Figure 3.4a**, a

Chapter 3. High-performance flexible PSCs using a TRTC electrode

stronger field intensity or localization is clearly observed for the near-infrared and visible regions of the active layer.

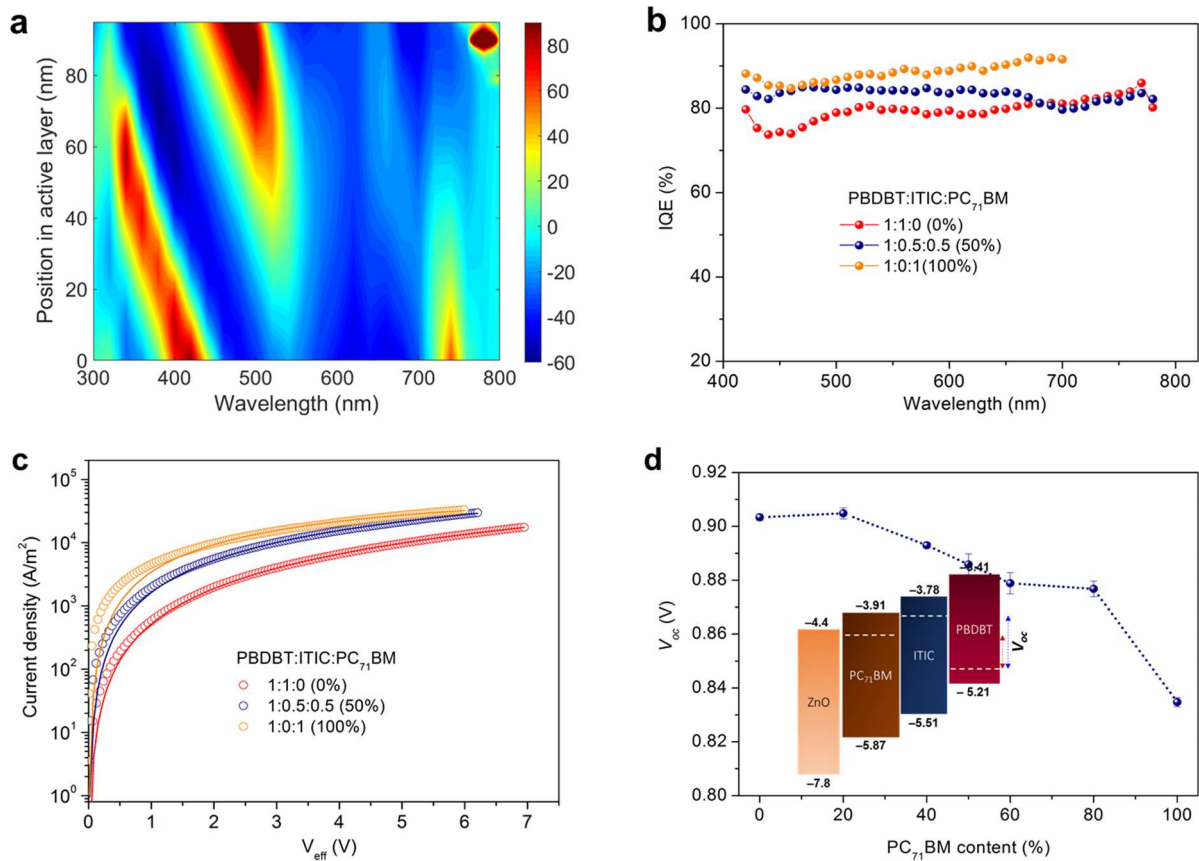


Figure 3.4. (a) Contour plot of the electrical field intensity ($|E|^2$) percentage change in the active layer for the 50% PC₇₁BM ternary and non-fullerene ITO devices. The vertical axis indicates the position in the active layer relative to the end of the SG-ZnO layer (0 nm) and the beginning of the MoO₃ layer (95 nm). (b) Measured IQEs for the PBDBT:ITIC:PC₇₁BM ternary ITO cells with various PC₇₁BM ratios. IQE here were obtained following the reported method^{20,97}. $IQE(\lambda) = \text{measured } EQE(\lambda) / (1 - R(\lambda) - A(\lambda))$, where $R(\lambda)$ is the reflectance of the device and $A(\lambda)$ is the parasitic absorption of non-active layers in the devices calculated by transfer matrix method. (c) Dark J - V curves of the ternary blend based electron-only devices and the solid lines present the best fittings for the measured data. (d) The V_{oc} evolution with PC₇₁BM fraction in the ternary ITO devices. Inset: energy level diagram of the used materials.

Chapter 3. High-performance flexible PSCs using a TRTC electrode

Such an enhancement is nicely reflected in the EQEs of Figure 3.3b, where the 50% PC₇₁BM cell outperforms its PCBM-free counterpart both in the visible region (< 650 nm, PC₇₁BM contribution) and in the near infrared range (730-800 nm, DIO contribution). The introduction of PC₇₁BM is also responsible for an increased IQE (Figure 3.4b): an approximate value of 0.88 was found throughout the whole measured range for the binary PBDBT:PC₇₁BM fullerene cell, while non-fullerene cells did not show IQE values higher than ~ 0.80 on average.

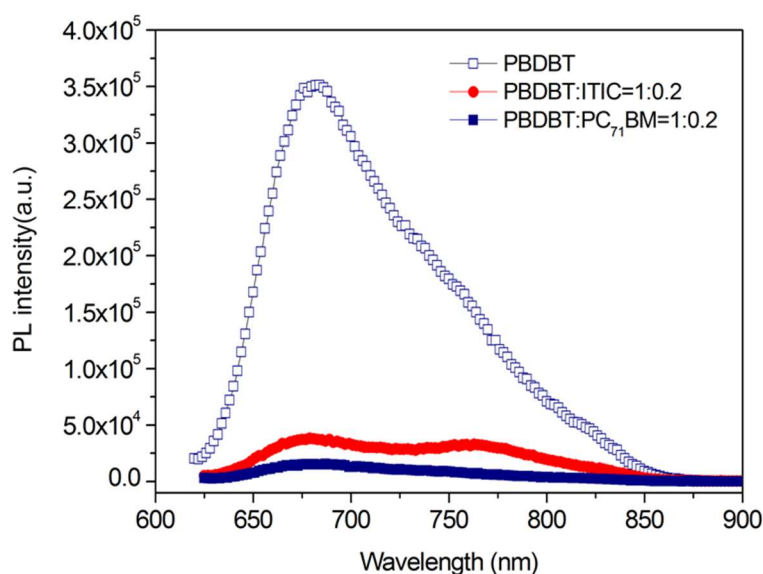


Figure 3.5. PL spectra of the thin films of the PBDBT polymer, PBDBT:ITIC(1:0.2 wt/wt) and PBDBT:PC₇₁BM (1:0.2 wt/wt). Excitation wavelength is 610 nm.

We ascribe such lower IQE values to the lower exciton dissociation and charge extraction efficiencies of the non-fullerene system. The photoluminescence quenching (**Figure 3.5**) and electron-only device experiments confirms such trend in the IQE. The electron mobility extracted from the dark I-V curves of Figure 3.4c using the space charge limited current (SCLC) method, is estimated to be $1.8 \times 10^{-4} \text{ cm}^2 \text{ V}^{-1} \text{ s}^{-1}$ for the non-fullerene electron-only device. This value is 4 times less than that of the 50% PC₇₁BM blend ($7.8 \times 10^{-4} \text{ cm}^2 \text{ V}^{-1} \text{ s}^{-1}$) and one order of magnitude lower than the

Chapter 3. High-performance flexible PSCs using a TRTC electrode

one relative to the 100% PC₇₁BM blend ($2.5 \times 10^{-3} \text{ cm}^2 \text{ V}^{-1} \text{ s}^{-1}$). The details for mobility calculation is shown in **Appendix C**.

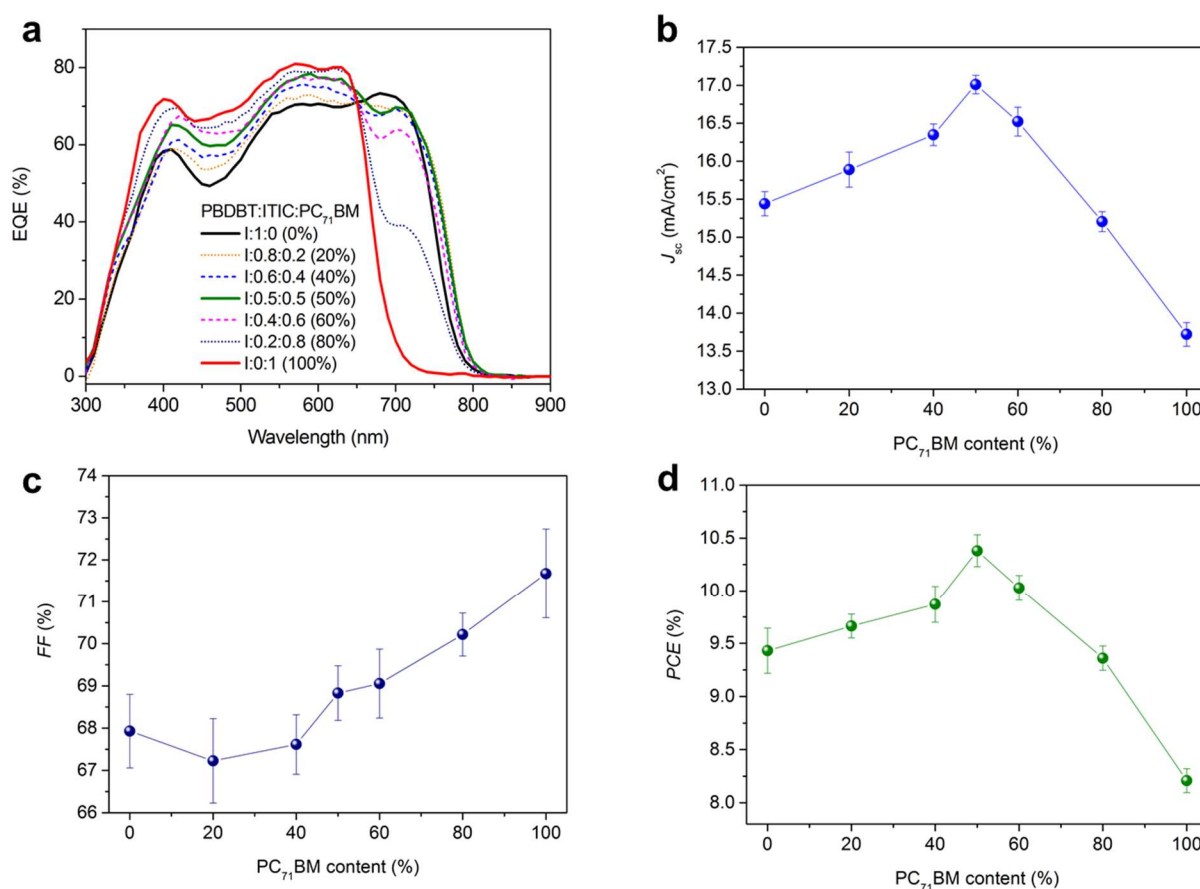


Figure 3.6. (a) EQE spectra of the inverted PBDBT:ITIC:PC₇₁BM ternary ITO cells with different PC₇₁BM fractions. Evolution of (b) J_{sc} , (c) FF and (d) PCE are shown for devices as function of PCBM content in the ternary blend.

The figures of merit (FOM) of the PBDBT:ITIC:PC₇₁BM ternary cell are presented in **Figure 3.6** and **Table 3.2**, as a function of the PC₇₁BM content. It clearly shows how PC₇₁BM addition up to a certain percentage, induces a boost of each FOM. PC₇₁BM here seems to provide another more efficient independent electron-transporting channel in the ternary blend systems, leading to a higher electron mobility and more balanced hole/electron mobility ratio. As a result, higher FF values in solar cells incorporating PC₇₁BM should be expected. An interesting observation on this system is that the V_{oc} tends to values close to those of the non-fullerene cell, as seen in Figure

Chapter 3. High-performance flexible PSCs using a TRTC electrode

3.4d. This suggests that after the exciton splitting, the electron quasi-Fermi level is more likely to be determined by the lowest unoccupied molecular orbital (LUMO) of the ITIC acceptor, as illustrated in the inset of Figure 3.4d.

Table 3.2. Photovoltaic properties of inverted PBDBT:ITIC:PC₇₁BM ternary solar cells under AM 1.5G solar illumination at 100 mW cm⁻².

PBDBT:ITIC: PC ₇₁ BM	DIO (Vol)	J_{sc} (mA/cm ²)	V_{oc} (V)	FF (%)	PCE (%)	Hole/electron mobility (cm ² /Vs)
1:1:0 (0%)	0.5 %	15.44 ± 0.16	0.903 ± 0.002	67.7 ± 1.5	9.43 ± 0.21 (9.76)	2.8×10 ⁻⁴ / 1.8×10 ⁻⁴
1:0.8:0.2 (20%)	1 %	16.21 ± 0.24	0.905 ± 0.002	67.2 ± 1.0	9.86 ± 0.11 (10.14)	
1:0.6:0.4 (40%)	1.0 %	16.59 ± 0.14	0.893 ± 0.001	67.6 ± 0.7	10.02 ± 0.17 (10.16)	
1:0.5:0.5 (50%)	1.0 %	17.01 ± 0.12	0.886 ± 0.004	68.8 ± 0.6	10.37 ± 0.15 (10.65)	1.3×10 ⁻³ / 7.8×10 ⁻⁴
1:0.4:0.6 (60%)	1.0 %	16.52 ± 0.19	0.879 ± 0.004	69.1 ± 0.8	10.03 ± 0.12 (10.24)	
1:0.2:0.8 (80%)	1.0 %	15.20 ± 0.13	0.877 ± 0.003	70.2 ± 0.5	9.36 ± 0.12 (9.54)	
1:0:1 (100%)	1.0 %	13.72 ± 0.16	0.835 ± 0.002	71.7 ± 1.1	8.21 ± 0.11 (8.39)	1.0×10 ⁻³ / 2.5×10 ⁻³

3.3 Integration of TRTC on PET substrates for high-performance flexible cells

The TRTC electrode was sequentially deposited at room temperature by a scalable sputtering technology, which allows for an easy implementation on polyethylene terephthalate (PET) or other plastic foil substrates. In contrast to the silver metal nanowires (AgNWs)^{98,99} or metal grids^{100,101} based flexible electrodes, such layered TRTC causes no disturbance to the active layer nano-morphology or the cell's electrical properties^{102,103}. The TRTC was successfully implemented on the highly flexible PET substrates using the same procedure as for the SK10 glass substrates, as

Chapter 3. High-performance flexible PSCs using a TRTC electrode

detailed in the experimental section. The PET substrate has a refractive index (1.58-1.62) similar to the SK10 glass, therefore to reduce the reflectance loss of the air/PET interface, we deposited a 100 nm MgF_2 anti-refraction coating (ARC) layer on the other side of the substrate (see **Figure 3.7a**).

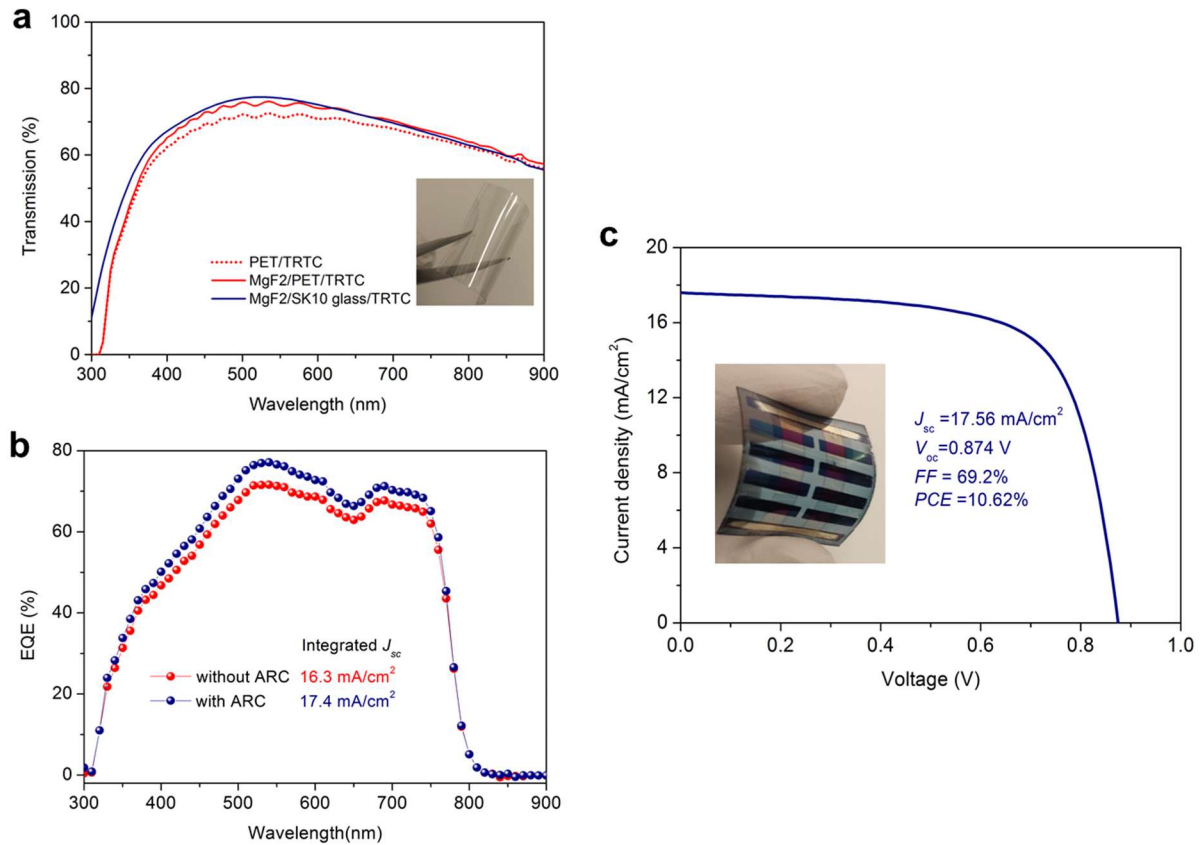


Figure 3.7. (a) Transmission spectra of PET/TRTC electrodes with and without a 100 nm MgF_2 layer. Here, TRTC is TiO_2 (18 nm)/ ZnO (5 nm)/Ag (9 nm)/ ZnO (3nm). For comparison, the transmission curve of MgF_2 /SK10 glass/TRTC is included. Inset is the flexible PET/TRTC electrode sample. (b) EQE spectra of flexible solar cells with configuration of PET substrate/TRTC/SG- ZnO (10 nm)/PBDBT:ITIC:PC₇₁BM (1:0.5:0.5, 95nm)/ MoO_3 (5 nm)/Ag (100 nm) without (red) and with (blue) a 100 nm MgF_2 ARC layer. (c) J - V curve of the best ARC coated PET-TRTC flexible cell. Inset: The photograph of flexible solar cells.

Chapter 3. High-performance flexible PSCs using a TRTC electrode

Figure 3.7b shows that by integrating the 50% PC₇₁BM blend based PET-TRTC cell with an ARC layer, a ~7% EQE increase can be reached, yet its performances are slightly lower than those of a SK10 glass-based counterpart, mainly due to the PET parasitic absorption and a slight difference in refractive index. A 10.6% best efficiency for a flexible cell was measured under AM1.5G 1-sun illumination, as shown in Figure 3.7c. It is worth noting that almost no loss in *FF* was observed for such flexible cells provided the measured sheet resistance of 8.8 Ω/sq for the flexible TRTC electrode is very similar to the 8.4 Ω/sq from the glass substrates.

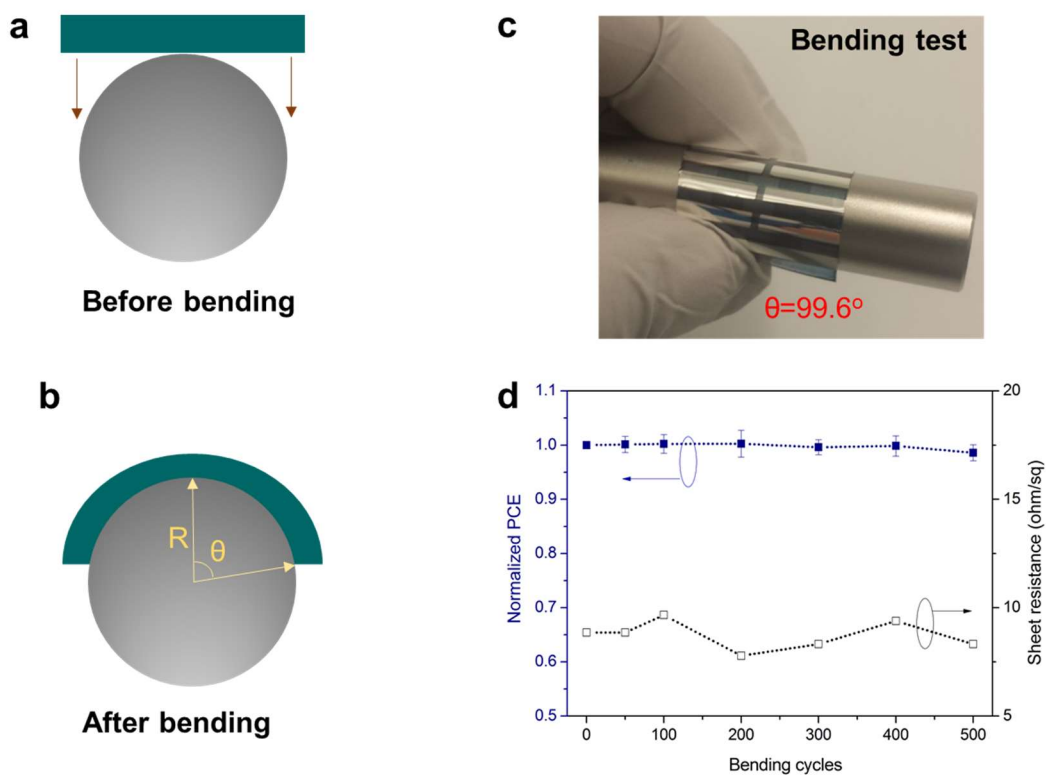


Figure 3.8. Schematic diagram of the bending tests of the PET-TRTC flexible electrode and solar cell, (a) before bending and (b) after bending. (c) Photograph of flexible devices under bending configuration. The nominal bending strain (ϵ) here is estimated to ~1.06% according to the equation of $\epsilon = h/2R$, where h is the thickness of PET substrate (125 μm) and R is the bending radius (~5.9 mm). (d) Mechanical flexibility test for PET-TRTC electrodes and solar cells.

Chapter 3. High-performance flexible PSCs using a TRTC electrode

Bending tests were performed on 50% PC₇₁BM flexible cells, as shown in **Figure 3.8**. No degradation was observed in the cell performance even after 500 bending cycles at a curvature radius of ~5.9 mm (calculation see Figure 3.8 a-c), demonstrating an excellent mechanical flexibility. This should be attributed to the non-brittleness nature of Ag metallic cavity layer (Figure 3.8d).

3.4 Impact of PC₇₁BM on thermal stability for ternary solar cells

Fullerene derivatives are known to have a tendency to aggregate in bulk-heterojunction blends under thermal treatment, causing a deterioration in the active layer nanomorphology and in the overall cell performance, in particular, in the presence of DIO or other small molecular additives^{58,104}. To obtain an intrinsically stable blend nanomorphology is a prerequisite for realizing long lifetime solar cells. It has been demonstrated that the use of non-fullerene alternatives eliminates light-induced burn-in and improves the cell stability⁶³. This is, however, not the only path to improve stability which can also be achieved by introducing a robust crystalline ordering in the fullerene phase. Indeed, very long lifetime solar cells using PTB7-Th:PC₇₁BM have been reported, too¹⁰⁵. This indicates that PC₇₁BM is still a good electron acceptor candidate for stable polymer solar cells. Thus, we examined the thermal stability of non-fullerene and 50% PC₇₁BM ternary blend based ITO cells. The devices were first encapsulated in a N₂-filled glovebox, and then they were thermally annealed at 85°C in air, according to the ISOS-D-1 protocol¹⁰⁶. Interestingly, as shown in **Figure 3.9**, both types of cells exhibited a similar degradation behavior with aging. A fast burn-in was observed during the first 5 hours of thermal aging and, after this initial ~ 20% relative loss, a steady plateau was reached with no major further losses. In other words, the PC₇₁BM addition does not cause any significant fullerene aggregation or nanomorphology change of the ternary films under temperature.

Chapter 3. High-performance flexible PSCs using a TRTC electrode

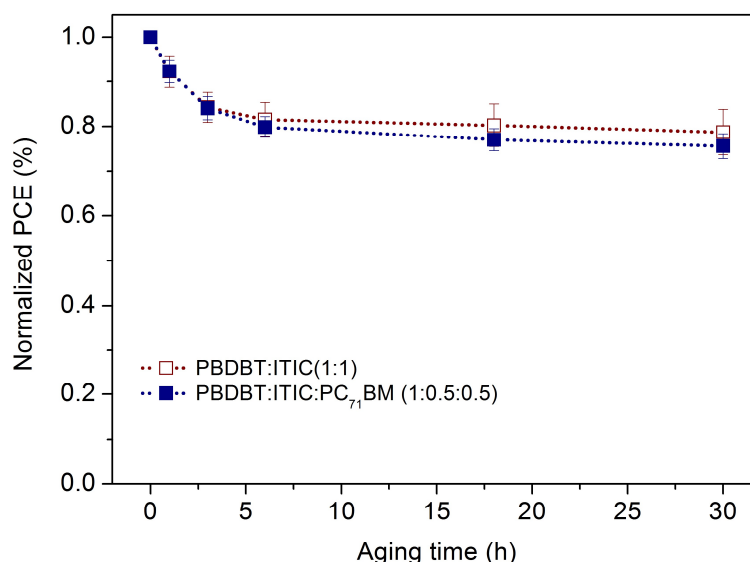


Figure 3.9. Normalized PCE evolution of the encapsulated cells under thermal annealing at 85 °C in air. Each data point presents the average value of over eight devices, and the error bars represent standard deviation of these data.

3.5 Conclusions

In summary, we demonstrated that the TRTC concept developed in chapter 2 is also applicable to find an optimal tradeoff between the J_{sc} and the V_{oc} . A significant enhancement in light absorption was seen for the TRTC cell when half of the ITIC acceptor in the active blend was replaced by PC₇₁BM. In that event, a high PCE cell is demonstrated while maintaining the open-circuit voltage as high as 0.882 V. On the other hand, the PC₇₁BM addition did not have any significant change on the device thermal stability. In addition, an almost negligible performance loss is observed compared to their glass counterparts when the TRTC device was implemented on flexible PET substrates. The approach presented may pave the ideal path to fabricate high-performance, large-area flexible solar panels for commercial applications.

Chapter 4

UV-induced molecular oxygen removal for enhanced stability

One of the major challenges that PSCs face is to prolong their operational lifetime. In this chapter, we study the photostability of one of the top performing polymer blends, PTB7-Th:PC₇₁BM, considered in Chapter 2 when employing a TRTC cavity⁸¹. Several studies have shown that PTB7- or PTB7-Th- based cells exhibit poor stability under different environmental conditions^{107,108,109}. The physics underlying the degradation dynamics is not fully understood, but molecular oxygen has been seen to be one of the corrosive agents that may strongly affect and degrade the composition of the blend active layer^{78,110,111,112}. A passive isolation from such corrosive elements has been shown to enhance the lifetime of the PSCs. However, an active removal of the oxygen has never been implemented to demonstrate a cell lifetime increase.

In this chapter, we provide an effective UV-induced removal of molecular oxygen chemisorbed on sol-gel ZnO electron transporting layer, to improve the photostability of PTB7:PC₇₁BM solar cells. Indeed, when such treatment is performed, the device lifetime under solar illumination is significantly prolonged, and device efficiency is

Chapter 4. UV-induced molecular oxygen removal for enhanced stability

improved as well. To study the molecular oxygen effect on device performance and photostability, in Section 4.1 we firstly investigate the photo degradation of the PTB7:PC₇₁BM photoactive material. Then, the mechanism of UV-induced chemisorbed oxygen removal is demonstrated in Section 4.2, and the device performance as function of UV treatment times are studied. Under optimal experimental condition, we study the long-term photostability of the UV-treated solar cells presented in Section 4.3. Finally, in Section 4.4 we discuss the recombination dynamics for the cells under light aging.

4.1 Device structure and photostability of PTB7-Th:PC₇₁BM active layer

In this section, we consider the performance and degradation dynamics of encapsulated cells under a continuous AM1.5G 1-sun illumination. Such device performance is strongly dependent on the electron-transporting and photoactive layers. In the inverted-architecture devices we fabricated, such layers were a 20 nm sol-gel deposited ZnO ETL and a 95 ± 5 nm thick bulk heterojunction blend of PTB7-Th:PC₇₁BM, as seen in **Figure 4.1**. In several of the fabricated devices, the interfacial properties of the ZnO layer were tailored with the UVN treatment described above. Unless otherwise specified, a glass-on-glass encapsulation was applied in the glovebox to all devices before testing them in ambient air. Additional details on the device fabrication procedure are given in Appendix B.

Chapter 4. UV-induced molecular oxygen removal for enhanced stability

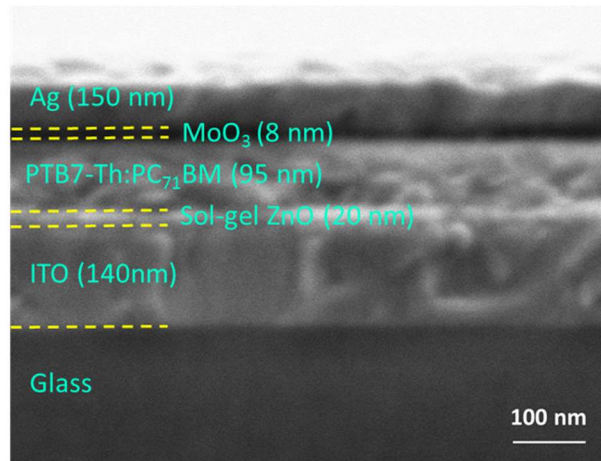


Figure 4.1. Scanning electron microscopy (SEM) image for the cross-section of the optimal inverted organic cell architecture used here: glass/ITO (140 nm)/sol-gel ZnO (20 nm)/PTB7-Th: PC₇₁BM (95 nm)/MoO₃ (8 nm)/Ag (150 nm).

Prior to such solar cell fabrication, and with the aim to evaluate the stability of the photoactive layer, we measured the optical transmittance of an ITO/photoactive film when irradiated under AM1.5G with 100 mW/cm² light intensity in ambient air, as shown in **Figure 4.2a**.

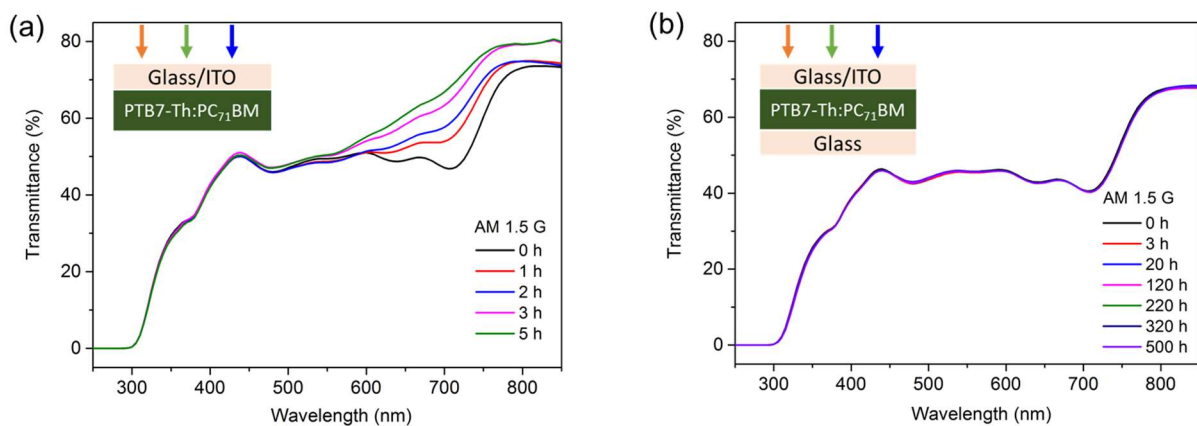


Figure 4.2. Transmittance evolution for ITO/PTB7-Th:PC₇₁BM photoactive films without (a) and with (b) glass encapsulation under AM1.5G 1 sun illumination in ambient atmosphere.

Chapter 4. UV-induced molecular oxygen removal for enhanced stability

After 5 h of continuous illumination, an increase in the transmittance spectra was seen in the 500–800 nm range, but no change was found in the 300–450 nm range; such wavelength ranges were ascribed to the PTB7-Th and PC₇₁BM components, respectively. Such an increase in transmission in the former wavelength range indicates that the π -conjugated PTB7-Th backbone is easily damaged by the combined exposure to air and light. However, such a conjugated backbone of the polymer showed an excellent photostability when encapsulated in the glovebox. As shown in Figure 4.2b, no change in the transmittance spectra was observed after 500 h of a continuous light-aging experiment. One may conclude that long-term photostable PTB7-Th:PC₇₁BM cells can be obtained if the oxygen content within the device is kept at an extremely low level.

4.2 Influence of UVN treatment on device performance.

In this section, we consider the removal of chemisorbed oxygen on the SG-ZnO ETL by applying a UV-treatment consisting on the ultraviolet (UV, 254nm) irradiation of the ZnO layer in a N₂-filled glovebox (hereafter the cells fabricated with such ZnO layers will be referred to UVN-treated cells). The reference cells without UV treatment is defines as non-UVN-treated cells. The J - V characteristics for UVN-treated and non-UVN-treated cells measured under AM1.5G solar illumination at 100 mW/cm² are shown in **Figure 4.3a**. The reference exhibited an average initial PCE of $8.94 \pm 0.16\%$, while the UVN-treated ZnO devices showed a 7% higher average efficiency of $9.54 \pm 0.16\%$, with 9.83% being the highest PCE obtained. The initial photovoltaic parameters for the reference and UVN-treated ZnO devices are shown in **Table 4.1**. The UVN-treated ZnO interlayer leads to a slight improvement in the FF and a significant enhancement in the J_{sc} . The latter one is confirmed by the external quantum efficiency (EQE) measurement, shown in Figure 4.3b, where UVN-treated ZnO cells exhibit an enhanced efficiency throughout the full spectral range.

Chapter 4. UV-induced molecular oxygen removal for enhanced stability

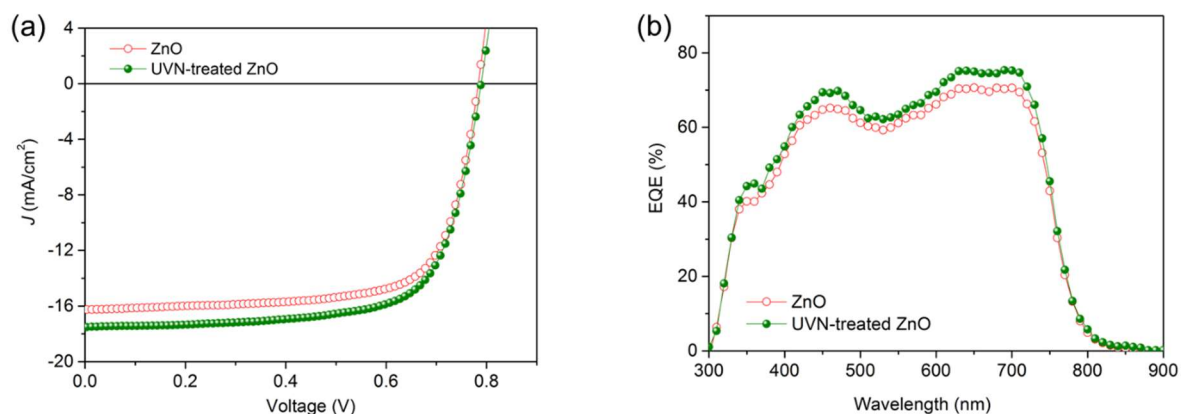


Figure 4.3. Effect of the UVN treatment on PTB7-Th:PC71BM solar cell performance. (a) Current density versus voltage (J – V) characteristics of UVN-treated ZnO (solid circles) and reference (open circles) solar cells measured under 1000 W m⁻² AM1.5G illumination. (B) External quantum efficiency (EQE) spectra of UVN-treated ZnO (solid circles) and reference (open circles) solar cells.

It is generally accepted that the surface of a ZnO film contains many oxygen vacancies (or Zn²⁺), which are deep, electron-donating sites¹¹³. The electrons in these sites (around 1eV below the conduction band) are likely to interact with molecular oxygen from the ambient air during film preparation, leading to the formation of chemisorbed O₂⁻ species, as schematically illustrated in **Figure 4.4a**¹¹⁴. This typically results in a high density of surface defects and thus an undesirable energy barrier for electron transport and extraction. We confirmed the presence of such an energy barrier for the untreated ZnO cells by illuminating them with a GG475-filtered AM1.5G source. In that event, an s-shape can be seen in the J – V curves shown in Figure 4.4b.

Chapter 4. UV-induced molecular oxygen removal for enhanced stability

Table 4.1. Initial (Fresh) and after a 500 h degradation photovoltaic parameters, decay constants and lifetime for reference, UVN treated ZnO, PFN, and no ETL devices.

ETL	Photovoltaic properties ^[a]				Decay constant and lifetime ^[b]		
		J_{sc} (mA/cm ²)	V_{oc} (V)	FF (%)	PCE (%)	τ (h)	T_{80} (h)
ZnO reference	Fresh	16.12 ± 0.20	0.79	70.2 ± 1.0	8.94 ± 0.16 (9.19)	1843.5	~ 190
	Degraded (500 h)	14.70 ± 0.23	0.78	53.8 ± 1.6	6.14 ± 0.24		
UVN- treated ZnO	Fresh	16.92 ± 0.37	0.79	71.5 ± 1.2	9.54 ± 0.16 (9.83)	4181.4	~ 540
	Degraded (500 h)	16.01 ± 0.07	0.79	59.6 ± 0.5	7.68 ± 0.09		
PFN	Fresh	16.80 ± 0.10	0.78	69.2 ± 1.6	9.07 ± 0.17 (9.22)	3215.1	~ 500
	Degraded (500 h)	15.31 ± 0.15	0.79	60.3 ± 0.9	7.26 ± 0.13		
Non-ETL	Fresh	16.37 ± 0.30	0.57	59.7 ± 0.6	5.63 ± 0.16 (5.86)	3071.9	~ 550
	Degraded (500 h)	13.55 ± 0.29	0.60	55.5 ± 2.2	4.52 ± 0.17		

^[a] The average values and standard deviations are obtained from over 20 devices for fresh cells and over 8 devices for degraded cells. The best PCE values are shown in parentheses.

^[b] Decay constants and lifetimes are extracted from double-exponential decay fittings of PCE evolution. Aging was carried out under a UV-filtered AM1.5G ($\lambda > 400$ nm) one-sun illumination. T_{80} corresponds to the time it takes for the cell PCE to drop to 80% of its initial value.

Upon illumination with UV light above the ZnO band gap, electron–hole pairs are generated and free holes are likely to migrate and recombine with the near trapped electrons. Consequently, the O_2^- species are neutralized and detached from the ZnO film^{115,116,117}. In the event that such UV-treated ZnO layers are placed again in ambient air, the reverse process occurs within minutes. We completed a cell with such a UVN-treated ZnO layer but placed in air and observed a performance no different than that of the reference cell. Therefore, to avoid oxygen reabsorption, we implemented the UV treatment in an inert atmosphere (O_2 content < 10 ppm) and kept the cells in this

Chapter 4. UV-induced molecular oxygen removal for enhanced stability

atmosphere until completed¹¹⁸. As shown in Figure 4.4c, no barrier is seen for such UVN-treated cells.

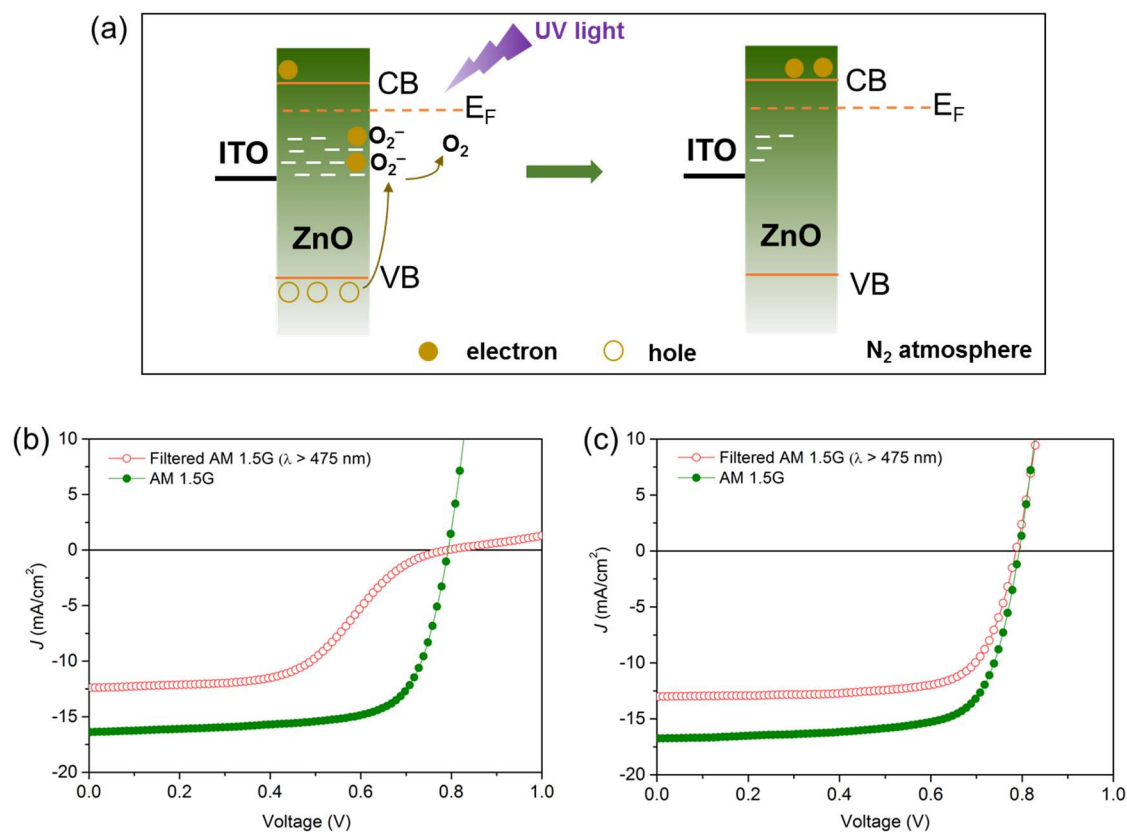


Figure 4.4. (a) Schematic diagram of the sol-gel ZnO film and UV illumination interaction in a N_2 atmosphere. J - V characteristics of inverted PTB7-Th: PC70BM solar cells under AM1.5G illumination with and without UV blocking filter ($\lambda > 475$ nm) employing (b) non-treated ZnO, and (c) UVN-treated ZnO as ETL.

Given the complexity of ZnO surfaces, the type of UV treatment applied may also result in the desorption of hydroxyl groups or the destruction of organic solvent residues^{119,120}. However, such changes may have a smaller effect on the degradation dynamics for the type of blend under consideration. Indeed, as was recently demonstrated, oxygen is a major source of destruction of the PTB7 polymer conjugation¹⁰⁸. In addition, it has been shown that the combined effects of light and oxygen strongly reduce electronic properties in the PC₇₁BM phase¹²¹.

Chapter 4. UV-induced molecular oxygen removal for enhanced stability

We investigated the effect of the UVN exposure time on the device performance. As shown in **Figure 4.5a**, the largest improvement in FF was obtained for a 20 min exposure, while enhancements in J_{sc} were observed for all UVN-treated devices when compared to J_{sc} values of reference cells. Provided that the V_{oc} did not change, except for exposure times larger than 20 min, as seen in Figure 4.5b, we concluded that the 20 min UVN treatment led to the largest PCE, as seen in **Table 4.2**. Such optimal performance was attributed to the enhanced conductivity of the ZnO ETL and the reduced interface recombination^{20,122}, which was confirmed by the I–V conductivity measurements from diode devices of ITO/ZnO (without UVN treatment) (100 nm)/Al, as shown in Figure 4.5c.

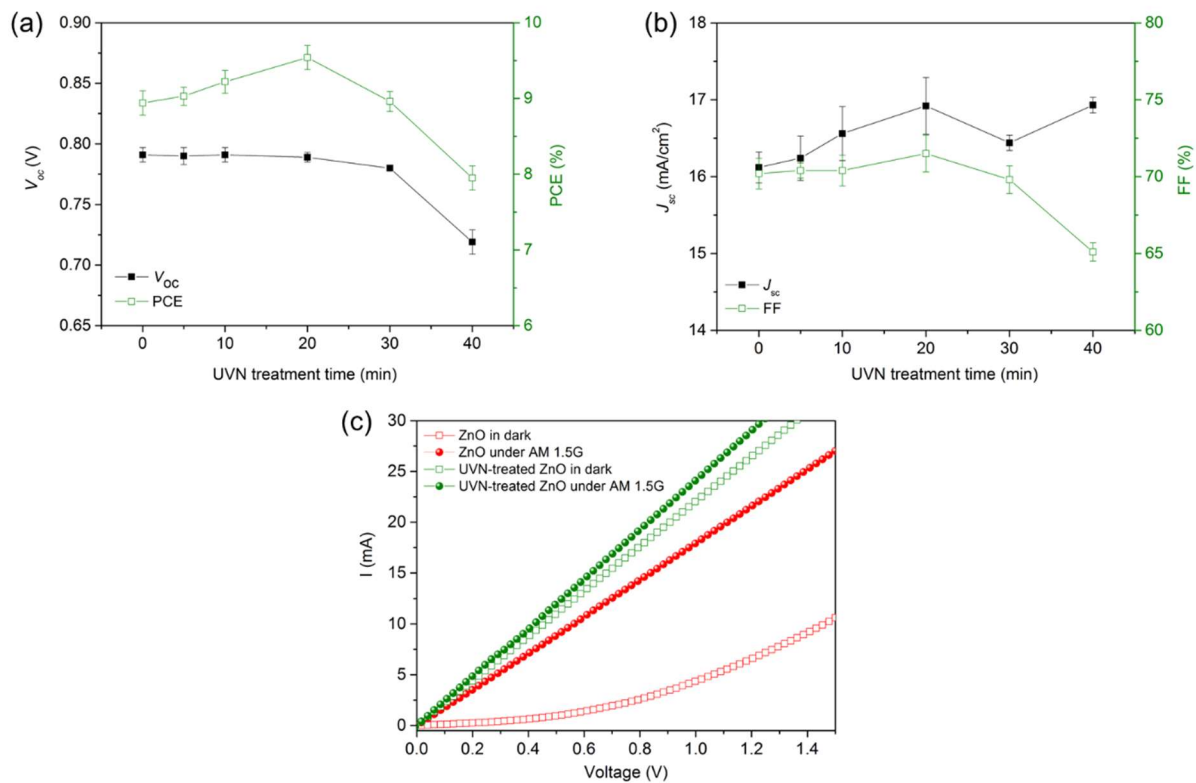


Figure 4.5. V_{oc} and PCE (a) J_{sc} and FF (b) and as a function of the UVN exposure time on the ZnO interlayer. Each data point represents the average over 20 devices and the error bars represent the standard deviation of these data. (c) I–V curves of the devices for ITO/with and without 20 min UVN-treated ZnO (100 nm)/Al in the dark and under AM1.5G one-sun illumination.

Chapter 4. UV-induced molecular oxygen removal for enhanced stability

Table 4.2. Photovoltaic performance for PTB7-Th: PC₇₁BM devices using ZnO as ETL with various UVN treatment times under AM1.5G illumination at 100 mW/cm².

UVN treatment	J_{sc} (mA/cm ²)	V_{oc} (V)	FF (%)	PCE (%)	R_s (Ohm·cm ²)
None	16.12 ± 0.20	0.79	70.2 ± 1.0	8.94 ± 0.16 (9.19)	4.46 ± 0.35
5 min	16.24 ± 0.29	0.79	70.4 ± 0.5	9.03 ± 0.12 (9.27)	4.38 ± 0.33
10 min	16.56 ± 0.35	0.79	70.4 ± 1.0	9.22 ± 0.15 (9.48)	4.36 ± 0.23
20 min	16.92 ± 0.37	0.79	71.5 ± 1.2	9.54 ± 0.16 (9.83)	4.30 ± 0.34
30 min	16.44 ± 0.10	0.78	69.8 ± 0.9	8.96 ± 0.13 (9.10)	5.05 ± 0.10
40 min	16.93 ± 0.10	0.72	65.1 ± 0.6	7.95 ± 0.16 (8.25)	7.38 ± 0.59

The electrical conductivity under illumination for UVN-treated ZnO film was $\sim 4.16 \times 10^{-4}$ S/m, about 1.5 times higher than the one from as-prepared ZnO film. The current in UVN-treated ZnO film increased by ~ 22 -fold at 1 V in the dark compared to as-prepared ZnO. Such features indicate that the chemisorbed O_2^- defects on ZnO surface were significantly reduced by UVN treatment, which led to the enhancement in electron concentration in the ZnO conduction band. However, one should note that UV exposures longer than 20 min increased the carrier concentration in the ZnO ETL to a level where carrier selectivity was lost and the cell's electrical properties degraded¹²³. This led to the reduction in FF and V_{oc} seen in Figure 4.5, and to the increase in the series resistance seen in Table 4.2. The UV-induced shunt recombination caused by such very high n-doping ZnO resulted in the tunneling of holes from the adjacent PTB7-Th valence band into the ZnO conduction band¹⁶. Note also that, as seen in Figure 4.4c, the UVN-pretreated ZnO cells did not require a UV activation to reach optimal performance, similar to the Al-doped ZnO (AZO) devices¹²⁴.

Chapter 4. UV-induced molecular oxygen removal for enhanced stability

4.3 Effect of UVN treatment on device photostability.

As indicated, the finished reference and UVN-treated ZnO devices were subjected to a continuous UV filtered AM1.5G 1 sun aging in an open-circuit configuration in air. The UV light at wavelengths below 400 nm was filtered out using a GG400 filter in order to reduce the undesirable photochemical reactions and burn-in loss^{47,61}. An in-depth study on the burn-in degradation dynamics for PTB7-Th:PC₇₁BM-based inverted cells will be given in Chapter 5. Beyond 100 h of light exposure, when the burn-in loss effect becomes marginal, we observe (**Figure 4.6a** and **Table 4.1**) that the performance of UVN-treated cells degrades more than two times slower than the reference cells. The V_{oc} of the reference and UVN-treated ZnO devices was stable within the time scale of degradation considered.

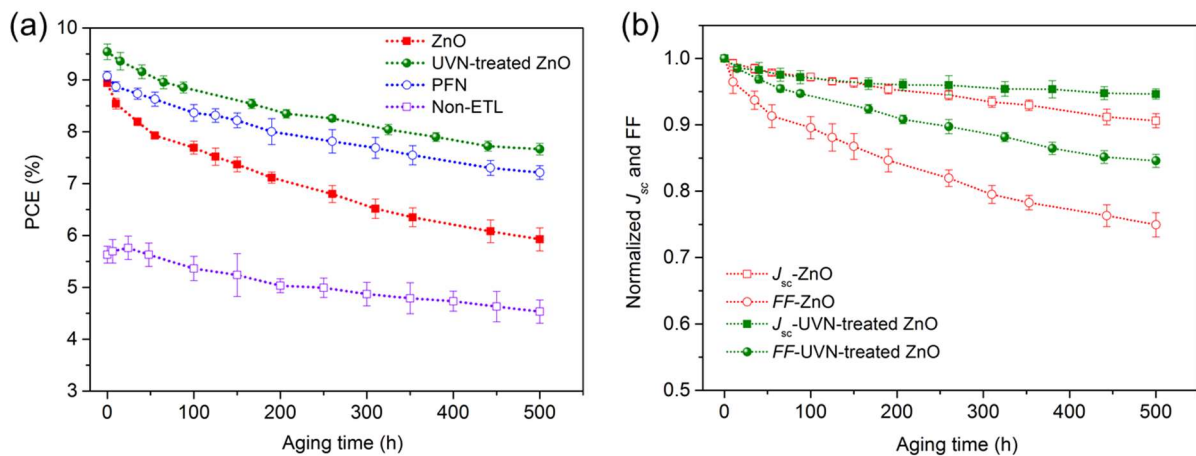


Figure 4.6. (a) Normalized PCE time evolution for encapsulated reference, UVN-treated ZnO, PFN, and no-ETL devices subject to a continuous UV-filtered AM1.5G illumination ($\lambda > 400$ nm, 100 mW/cm²) at 40 ± 5 °C. (b) Normalized J_{sc} and FF evolution for reference and UVN-treated ZnO devices. Each data point represents the average over six devices, and the error bars represent the standard deviation of these data.

The major PCE loss originates from the J_{sc} and FF decays, as shown in Figure 4.6b. One may confirm the effectiveness of the active oxygen removal induced by the UV

Chapter 4. UV-induced molecular oxygen removal for enhanced stability

light by comparing the decay dynamics of the UVN-treated cell with that of cells fabricated using an oxygen-free ETL such as PFN. In both cases, as seen in Figure 4.6a, the measured decay time beyond 100 h is close to the one measured for the UVN-treated cell. Indeed, beyond the effect of the burn-in, for all four cases under consideration, the device evolution dynamics can be adjusted to a single exponential decay, as seen in **Figure 4.7**. The decay time for the reference cell was determined to be less than 2000 h while for the other three cells the decay time is about 2 times larger, the decay time for the UVN-treated device being the largest one. The decay times were extracted from the best fittings of the normalized PCE degradation curves using a two-exponential decay function, as seen in **Appendix D**. The three cells with a molecular-oxygen free ETL exhibited T_{80} lifetimes in the 500–550 h range, while that for the reference was close to 2.5 times shorter, as seen in Table 4.1.

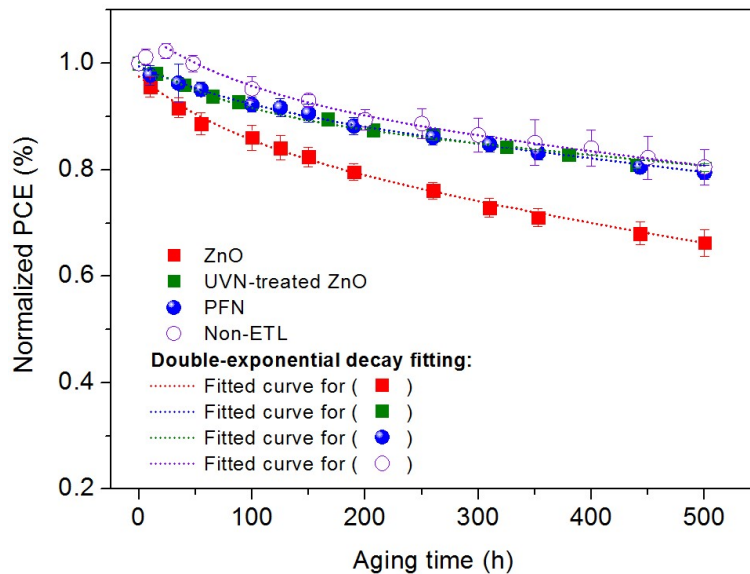


Figure 4.7. Normalized PCE fitting curves using double-exponential decay function¹⁰⁶ of $PCE(t) = A_1 \cdot e^{-t/\tau_{\text{Burn-in}}} + A_2 \cdot e^{-t/\tau}$ for encapsulated devices with ZnO, UVN-treated ZnO and PFN as ETL and Non-ETL are shown under continuous AM 1.5G illumination ($\lambda > 400$ nm, 100 mW/cm^2).

4.4 Discussion of UVN treatment on intensity dependence of the V_{oc}

To shed some light into what the effect of the molecular oxygen removal is, in this section we investigated the V_{oc} dependence on light intensity, shown in **Figure 4.8**. The slopes of the V_{oc} versus the natural logarithm of the light intensity are similar for the fresh reference and UVN-treated ZnO devices, implying that a similar mechanism of bimolecular recombination is dominant in fresh cells¹²⁵. After 500 h of illumination, the slope of the degraded reference cell increased by 1.25, whereas the increase for the UVN-treated ZnO cell was only 1.15. The higher slope seems to indicate a larger increase in the number of Shockley–Read–Hall (SRH) or trap-assisted recombination sites in the reference cells than in the cells where the UVN treatment is applied. Ascribing the larger slope seen for the aged reference cell to oxygen-induced traps is one possibility¹²², but alternative explanations based on an increase in the density of states disorder may be plausible, too¹²⁶.

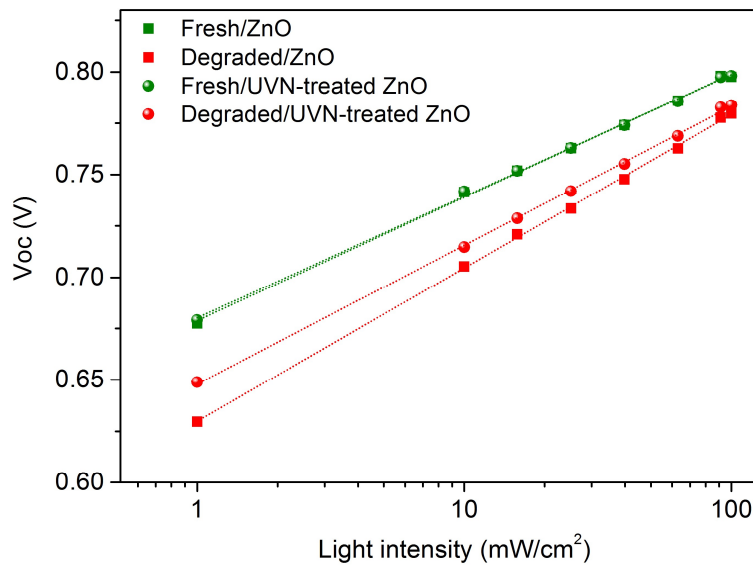


Figure 4.8. Measured V_{oc} of UVN-treated and reference cells before and after a 500 h degradation cycle as a function of light intensity (symbols), together with linear fittings of the data (dotted lines).

Chapter 4. UV-induced molecular oxygen removal for enhanced stability

It is also worth noting that the oxygen removal approach we implemented for the PTB7-Th:PC₇₁BM cells can also be successfully applied to other high-performance low-band-gap photoactive materials. Simultaneous enhancement of the PCE and photostability was also demonstrated for PffBT4TOD: PC₇₁BM inverted cells¹²⁷ when the UVN-treated ZnO ETL was incorporated. UVN-treated ZnO devices showed an enhanced average PCE of 9.5% compared to 9.1% for the reference devices without further optimization (see **Table 4.4**). An enhanced photostability, indicating a 45% PCE loss for the treated cell over a 60% loss for the untreated one, was seen under UV-filtered illumination for 120 h, as shown in **Figure 4.9**.

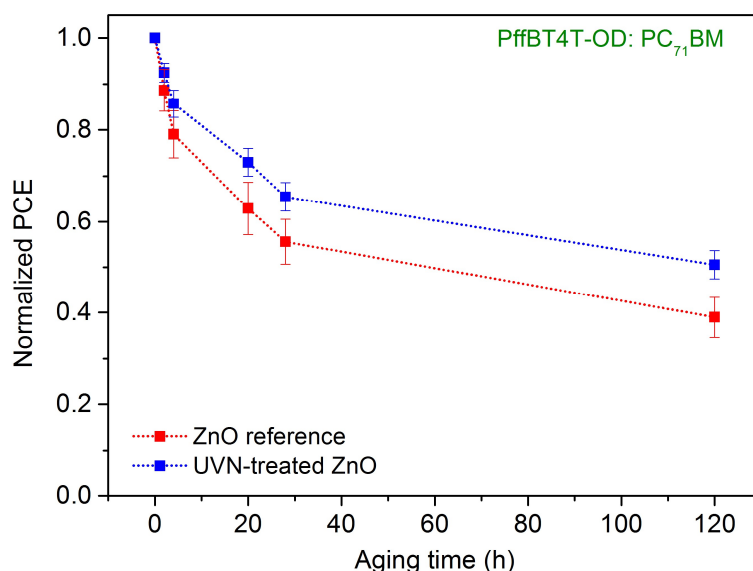


Figure 4.9. Normalized PCE evolution for inverted PffBT4T-OD: PC₇₁BM based solar cells using ZnO and UVN-treated ZnO ETLs over 120 h of continuous AM1.5G 1-sun illumination with GG400 UV-filter. Each data point represents the average over 8 devices and the error bars represent standard deviation of these data.

Chapter 4. UV-induced molecular oxygen removal for enhanced stability

Table 4.4. Photovoltaic properties from inverted devices using PffBT4T-2OD:PC₇₁BM BHJ with various ETL under AM1.5G one sun illumination.

ETL	J_{sc} (mA/cm ²)	V_{oc} (V)	FF (%)	PCE (%)	PCE_{max} (%)
ZnO	17.52 ± 0.033	0.74	68.2 ± 0.89	8.86 ± 0.09	9.06
UVN-treated ZnO	17.96 ± 0.032	0.75	68.4 ± 2.62	9.20 ± 0.21	9.51

4.4 Conclusions

In this chapter, we have demonstrated that PTB7-Th polymer based cells have the potential to become very stable, provided that finished devices are not under the action of strong oxidizing elements like oxygen. We have shown that the light transmission spectrum from an encapsulated PTB7-Th:PC₇₁BM blend layer remains unaltered, even when under continuous 1-sun illumination. However, for the long-term stability of such polymer solar devices, isolation from corrosive elements may not be sufficient. An active removal of such elements, which may be embedded in small quantities in the finished device during the fabrication process, must be implemented. We demonstrated that the active removal of oxygen molecules adsorbed on the ETL and photoactive material interface increases the lifetime of high-performance low-band-gap polymer cells with improved initial photovoltaic parameters for the device. Finally, it is worth mentioning that the oxygen removal procedure considered is simple, and a low cost implementation for the large-scale production of polymer solar panels should be feasible.

Chapter 5

Circumventing light-induced PCBM disorder for long lifetime PSC

In Chapter 4, we demonstrated that the photostability of PTB7-Th:PC₇₁BM cells can be enhanced by actively removing the chemisorbed oxygen¹²⁸. However, a rapid decrease in performance can still be seen for such oxygen-free devices under AM1.5G 1-sun illumination. For the most studied case of PSCs, different experimental results have demonstrated that the rapid decrease in device performance when exposed to light, known as burn-in⁴⁷, can be linked to a rapid degradation of the electron transport, while the transport of holes appears to be unaffected.¹²⁹ This burn-in is thought to lead to a degradation of the nano-morphology of the blend¹³⁰, to the formation of trapped states¹³¹, to a broadening of the density of states¹²⁶, or to the forming of persistent free radicals in fullerene derivatives¹³². These effects have been shown to reduce the J_{sc} and other photovoltaic parameters.

When organic devices are isolated from such aggressive corrosive agents, the major source of cell degradation rests with UV photon exposure^{133,134}. Indeed, a short exposure to UV photons is sufficient to induce a decrease in efficiency close to 50% for some devices¹³⁵. The degradation dynamics directly linked to the absorption of UV

Chapter 5. Circumventing light-induced PCBM disorder for long lifetime PSC

photons, which in the absence of any oxidative elements leads to a dramatic irreversible change in the nano-morphology of the fullerene acceptor phase, are still not known. Understanding why the absorption of low momentum particles leads to a major material re-organization is essential to circumvent this problem.

In this chapter, we propose a new explanation to the light-induced burn-in in PTB7-Th:PC₇₁BM solar cells, which we show to be intrinsic to the absorption of UV photons in the PC₇₁BM acceptor phase. We also demonstrate that it is possible to circumvent this degradation path when a highly ordered PC₇₁BM phase is formed in the active layer. In that latter case, the burn-in loss is significantly suppressed and a long device lifetime is achieved. In section 5.1 we demonstrate how a spin flip occurring at the PC₇₁BM/active layer interface leads to a destruction of a weakly bonded nanomorphological order of PC₇₁BM phase. Then, in Section 5.2 we experimentally confirm that the burn-in is caused by UV-induced PC₇₁BM phase disorder. To address this problem, a robust nanocrystalline ordering in PC₇₁BM phase must be introduced in the active layer prior to sun illumination. In Section 5.3, we combine an optimized DIO-free blend with a thermal treatment to achieve such highly ordered PC₇₁BM phase while keeping high device efficiency. Finally, we perform the long term photostability test for the cells under AM1.5G 1-sun illumination.

5.1 Light-induced burn-in in PTB7-Th:PC₇₁BM polymer solar cells

In this study, we consider standard PTB7-Th:PC₇₁BM (1:1.5, by weight) inverted solar cells where the blend is prepared in the chlorobenzene (CB) and 3 vol% 1,8 diiodooctane (DIO) binary solvent. The device configuration is depicted in **Figure 5.1a**, used as a reference throughout the chapter. An initial high average PCE of 9.6% was achieved for the reference cell, but all the PV parameters degrade very fast under AM 1.5G full spectrum one-sun illumination, being the J_{sc} the parameter that exhibited the strongest decay, as shown in Figure 5.1b.

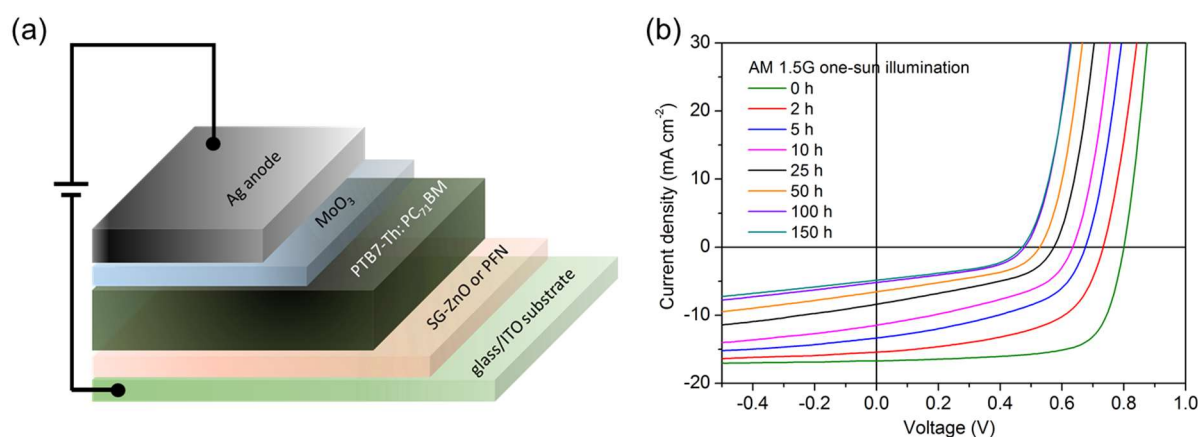


Figure 5.1. (a) Device structure of the inverted polymer solar cells in this study: glass substrate/ITO/ZnO or PFN/PTB7-Th:PC₇₁BM BHJ/MoO₃/Ag cathode. (b) Typical *J*-*V* evolution under AM 1.5G one-sun light stress.

At the interface between the donor and acceptor components, excitons generated by photon absorption are separated into electrons and holes. Excitons are generated in both the donor and acceptor phases. Photon absorption in the PC₇₁BM phase peaks at 470, 380 and below 300 nm. In a measurement of the PC₇₁BM photoluminescence at 5K, performed by Dyakonov and co-workers¹³⁶, the S₁ to S₀, T₁ to S₀, and T₂ to T₁ transitions were identified to be at 710, 800, and 900 nm, respectively. The estimated positions of these levels in an energy diagram are indicated in **Figure 5.2a**. Note that the exact S₂ to S₀ transition energy is not known and S₂ is pictured with an undefined position in the energy level diagram in Figure 5.2a.

After diffusion, excitons created in the PC₇₁BM phase reach the PTB7-Th/PC₇₁BM interface and access an intermolecular charge transfer (CT) state. In the CT state the binding energy is reduced and excitons are prone to dissociate^{137,138}. Depending on the absorbed photon energy, the CT states may be of S₂ or S₁ type. A larger electron-hole separation for the S₂ type CT state results in an even weaker binding energy, which combined with a similar energy for the S₂ and T₂ levels, provides an effective path for a spin flip to occur. Because of a forbidden T₁ to S₀ transition the PC₇₁BM anion of

Chapter 5. Circumventing light-induced PCBM disorder for long lifetime PSC

triplet type will live longer than an equivalent one of singlet type. A repulsive Coulombic interaction among several of such long-lived anions will favor a destruction of the order in the acceptor phase.

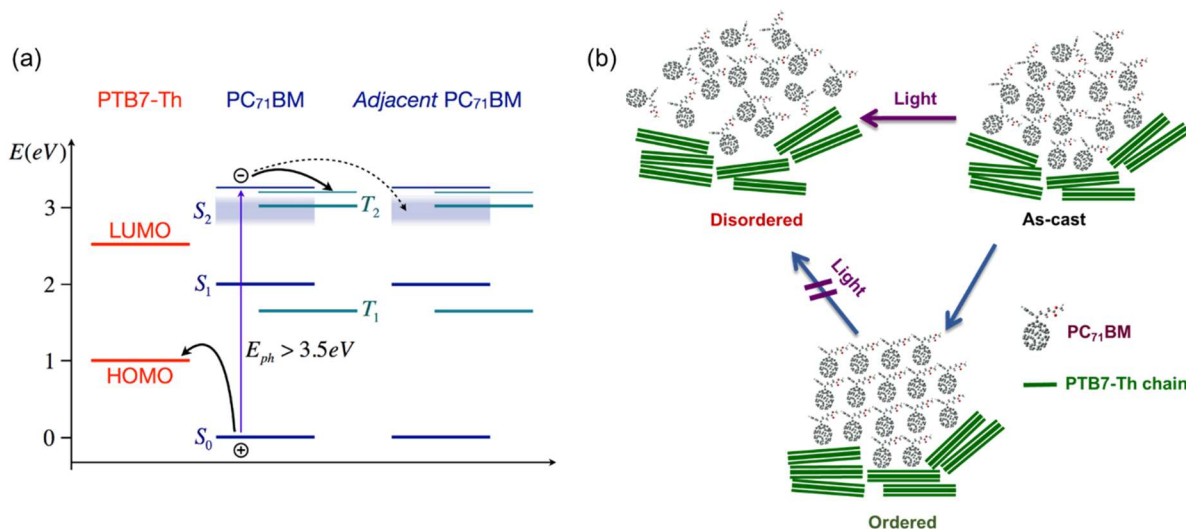


Figure 5.2. (a) Schematic illustration of the relevant electronic states in PTB7-Th:PC₇₁BM blends. PC₇₁BM ground states (S_0), singlet excited states (S_1 and S_2), and triplet states (T_1 and T_2) are indicated. Two possible paths for electrons in the acceptor domains after the splitting of high energy excitons are indicated. (b) Schematic drawing of two possible paths for the nanomorphology evolution in the PC₇₁BM acceptor phase: in the top one light induces disorder and in the bottom one light induced disorder is prevented in a highly crystalline configuration of the PC₇₁BM molecules.

Indeed, a continuous illumination with UV photons leads to a rapid and irreversible destruction of the acceptor phase order, as schematically shown in Figure 5.2b. The electrostatic potential energy that is accumulated in the acceptor phase cannot be easily channeled to the cathode when the anions are of triplet character, causing a stress in the blend morphology. Blends with a higher degree of crystallinity are more likely to withstand the pressure to release such electrostatic potential energy.

Chapter 5. Circumventing light-induced PCBM disorder for long lifetime PSC

To confirm that the degradation dynamics is triggered by the UV photon absorption, we studied the evolution of the PV parameters from encapsulated cells subject to a filtered 1-sun illumination. We used different UV longpass filters with cut-off wavelengths at 455 nm, 400 nm, 370 nm and 320 nm. As seen in **Figure 5.3a**, the normalized PCE evolutions can be adjusted to a double exponential decay with one large and one small time constant. All time constants and amplitudes used to fit the data are given in **Table 5.1**.

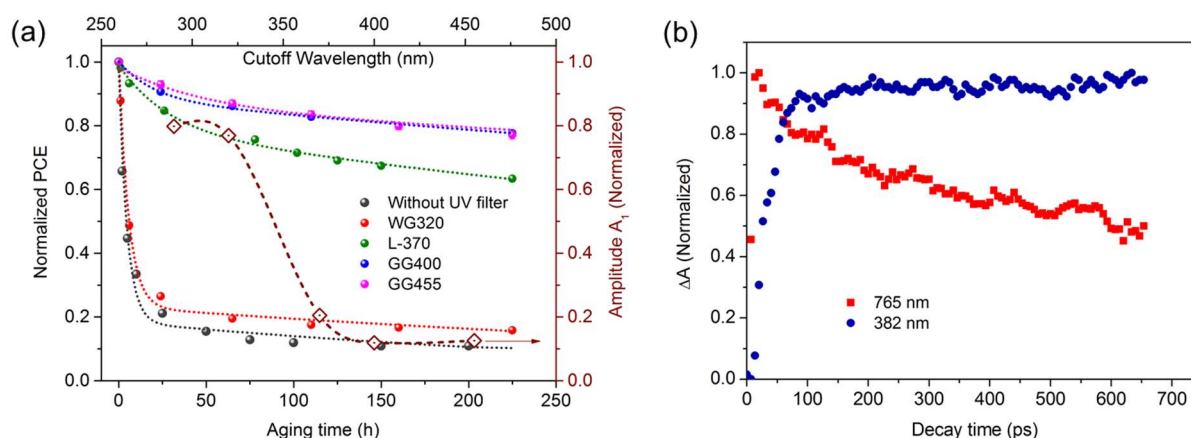


Figure 5.3. (a) UV-induced disorder in PC₇₁BM nano domains. Left and bottom axes: normalized experimental PCE evolutions (solid dots) under a UV filtered AM 1.5G 1-sun illumination and solid lines present the best double-exponential decay fittings. Top and right axes: Normalized amplitude for the first exponential in terms of the cut-off wavelength of the filter used. The cut-off wavelength of the long-pass UV filters is indicated dependent. (b) Transient absorption measurements on glass/PTB7-Th:PC₇₁BM films prepared from reference blends.

Chapter 5. Circumventing light-induced PCBM disorder for long lifetime PSC

Table 5.1 Double-exponential decay fitting parameters for the normalized PCE decay profiles of SG-ZnO reference devices under AM 1.5G one-sun illumination.

UV filter	A_1	τ_1 (h)	A_2	τ_2 (h)
Without UV filter	0.79856	4.70857	0.18534	356.135
WG320	0.7699	5.60372	0.23217	565.07798
L-370	0.20547	28.05524	0.78465	1041.72463
GG400	0.11947	20.27826	0.88113	1780.83405
GG455	0.12667	48.73345	0.8555	2639.82364

When the amplitude (A_1) corresponding to the short time exponential decay, which is directly linked to the burn-in, is plotted against the cut-off filter wavelength, as shown in **Figure 5.3a**, one observes a sharp transition occurring between 320 and 370 nm. This links the burn-in degradation threshold to transitions from the ground state to higher electronic states beyond the S_0 to S_1 electronic transition. As indicated above, when the higher energy excitations are in the CT state, a spin flip is likely to occur leading to the formation of PC₇₁BM triplet anions. The expected longer lifetimes for such triplet anions are confirmed in a time-resolved transient absorption experiment probing a 100 nm reference blend film deposited on fused silica glass substrate. The experimental setup and details of the transient absorption measurements are given in **Appendix E**.

This layer is probed using a 765 nm 120 fs pulse and pumped either with a pulse at the same wavelength or its second harmonic at 382.5 nm. As shown in **Figure 5.3b**, when the layer is pumped with the UV pulse at 382.5 nm, normalized absorption of the probe decreases if the probe and pump pulses overlap and remains unchanged, even when the probe pulse is delayed to the maximum time allowed by the set-up. On the contrary, when a device is pumped with an infrared pulse tuned at 765 nm, we observe a ~200 ps time constant decay which is close to the typical nano- or sub nano-

Chapter 5. Circumventing light-induced PCBM disorder for long lifetime PSC

second time constant decays seen in the allowed singlet to singlet molecular transitions.

5.2 UV-induced degradation of exciton diffusion and charge mobility in PC₇₁BM nano domains

The destruction of the order in the acceptor phase can be visualized in the external quantum efficiency (EQE) spectra as well as in single-polar devices. After aging the cells for 150 hours of non-UV-filtered AM1.5G 1-sun illumination, the EQE shown in the inset of **Figure 5.4a** exhibits a large reduction on the side of the PC₇₁BM absorption band (300-550 nm) while the side of the PTB7-Th absorption band (550-800 nm) remains relatively unchanged. These relative differences in the normalized EQE, seen in Figure 5.4a, clearly indicate that exciton diffusion in the PC₇₁BM phase is severely hindered provided that no change in the absorption wavelength dependence is seen¹²⁸. In other words, in the degraded cell, excitons created in the acceptor phase have more difficulties in reaching the interface. Electron-only devices fabricated from the reference active blends, indicate a dramatically diminished electron mobility with respect to light aging time, as shown in Figure 5.4b.

Chapter 5. Circumventing light-induced PCBM disorder for long lifetime PSC

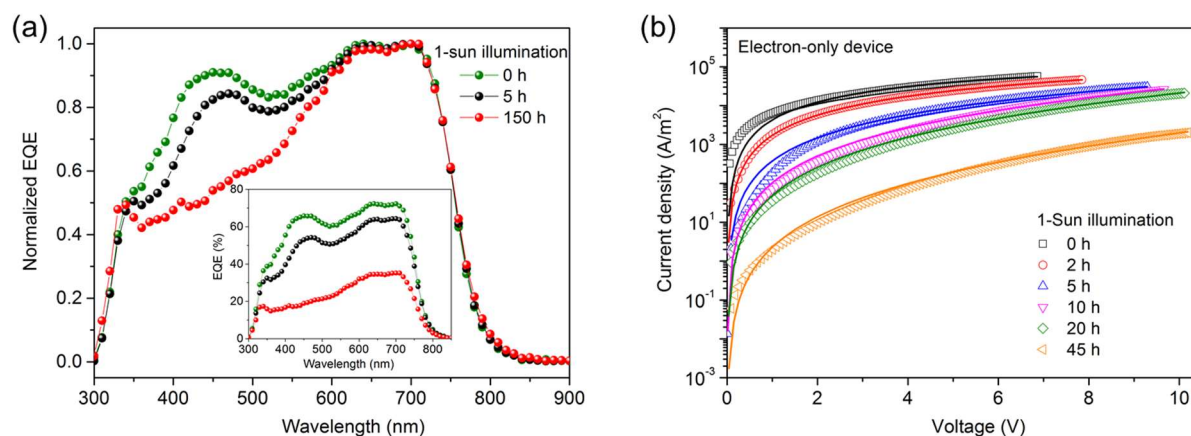


Figure 5.4. (a) Normalized external quantum efficiency (EQE) evolution under AM 1.5G 1-sun illumination. Inset: Absolute EQE spectra evolution. (b) Semi-log plot of the J - V characteristics for the ITO (135 nm)/SG-ZnO (20 nm)/PTB7-Th:PC₇₁BM (CB+3%DIO, 100 nm)/LiF (1 nm)/Al (100 nm) electron-only devices with respect to aging time under non-UV-filtered AM 1.5G illumination at 100 mWcm^{-2} . The solid lines present the best fittings using the SCLC modified Mott-Gurney model^{139,140}.

The electron mobility measured by the space-charge-limited current method was decreased by four orders of magnitude after 45 hours of AM 1.5G non-UV-filtered 1-sun illumination, from $2.43 \times 10^{-3} \text{ cm}^2/\text{Vs}$ to $2.16 \times 10^{-7} \text{ cm}^2/\text{Vs}$. In contrast, the transport of holes in PTB7-Th phase was slightly reduced by less than one order of magnitude, shown in **Figure 5.5a**. Note that such fast degradation in electron mobility can be greatly alleviated by filtering UV photons, as seen in Figure 5.5b, confirming that UV-induced disruption of the electron transport channel in the PC₇₁BM phase is the primary source of burn-in triggering. Contrary to what happens with PC₆₀BM based photovoltaic cells^{59, 141, 142}, there is no evidence of PC₇₁BM fullerene dimerization after light-soaking^{143,144}, which is confirmed by the transmittance and Raman spectra comparing fresh and light-aged PC₇₁BM samples, seen in **Figure 5.6**.

Chapter 5. Circumventing light-induced PCBM disorder for long lifetime PSC

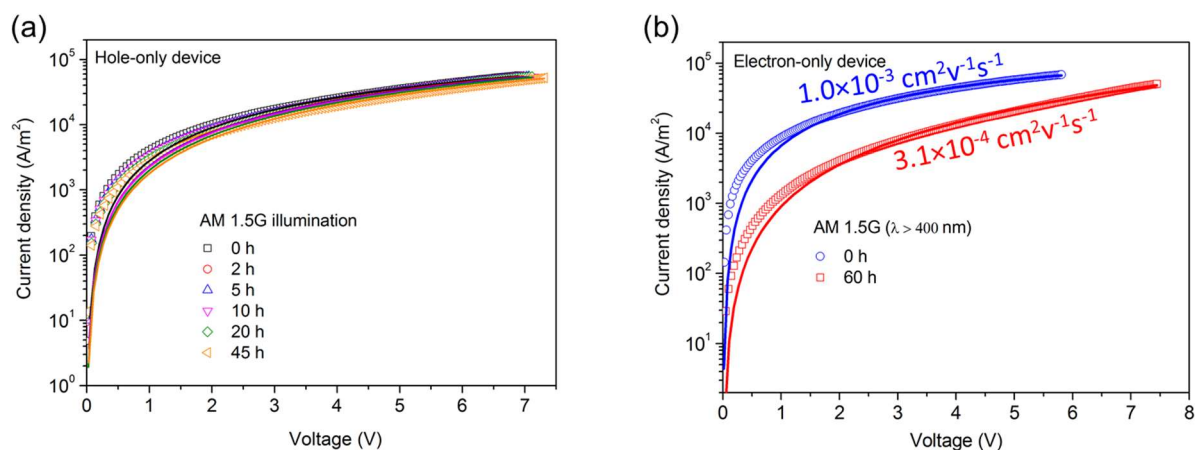


Figure 5.5. (a) Hole mobility evolution with respect to aging time under non-UV-filtered AM 1.5G 1-sun illumination. Hole-only device structure is ITO/PEDOT:PSS/PTB7-Th:PC₇₁BM (1:1.5 wt%, CB+3%DIO)/MoO₃/Ag. (b) Electron mobility change before and after 60 hours of UV filtered ($\lambda > 400 \text{ nm}$) AM 1.5G 1-sun illumination. Electron-only device structure is ITO (135 nm)/SG-ZnO (20 nm)/PTB7-Th:PC₇₁BM (1:1.5 wt%, CB+3%DIO, 100 nm)/LiF (1 nm)/Al (100 nm).

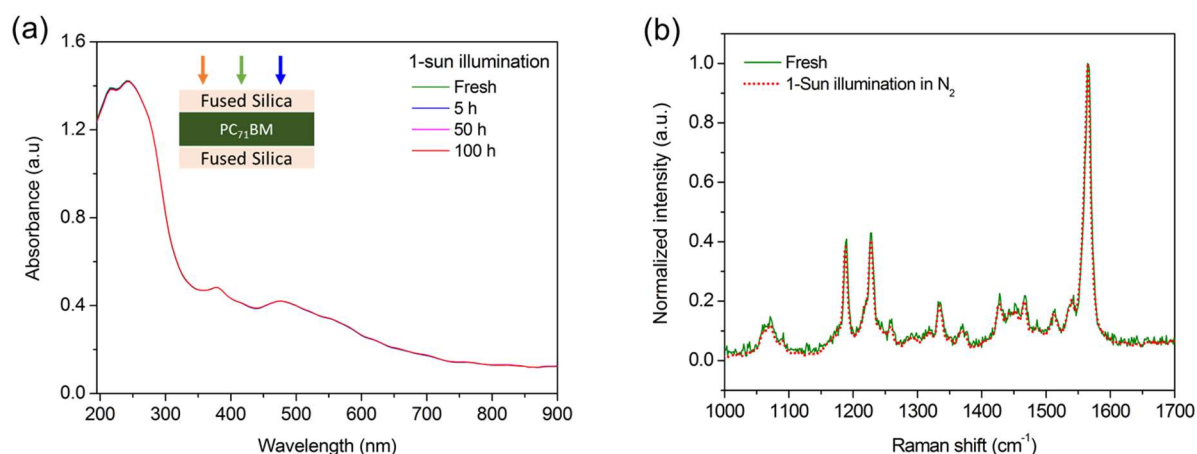


Figure 5.6. (a) Absorption spectral changes during non-UV-filtered AM 1.5G 1-sun illumination of a PC₇₁BM film encapsulated with fused silica glasses indicate no or very slight formation of fullerene dimers. (b) Raman spectra of an ITO/PC₇₁BM sample before and after 15 hours of one-sun light soaking in N₂-filled glovebox.

Chapter 5. Circumventing light-induced PCBM disorder for long lifetime PSC

The transfer of the photon energy to a CT state of triplet character is intrinsic to the acceptor phase at the donor-acceptor interface. However, once the energy has been converted into electrical potential energy the acceptor phase morphology, as well as the surrounding environment, play a fundamental role in the degradation of the electrical performance of the PSC. Consequently, using the same acceptor, PC₇₁BM, but a different donor polymer, a second stage in the UV light-induced aging may be markedly different. The relevant role played by the acceptor environment was confirmed when the burn-in was reduced by confining the acceptor domains in between polymer domains of increased crystallinity⁶⁰ or with higher molecular weight polymer chains⁶¹.

5.3 Circumventing PCBM disorder to achieve highly stable cells with high efficiency

To circumvent such powerful UV-induced PC₇₁BM disorder without having to replace PTB7-Th by a less efficient polymer that would better confine or immobilize the PC₇₁BM molecules, one must implement a set of procedures to freeze-in the morphological order in the blend, particularly in the acceptor domains. In addition to an obvious filtering of high energy photons, measures must be taken to limit the PC₇₁BM anion mobility. The use of DIO was eliminated since this additive may promote the penetration of PC₇₁BM into the polymer domains, thus facilitating the acceptor morphological disorder¹⁴⁵. We also eliminated other oxidant sources, such as the ZnO buffer layer, which may accelerate the degradation dynamics¹³, and we applied a thermal annealing, prior to light soaking, to increase the active layer crystalline order, particularly, in the PC₇₁BM domains.

The latter treatment combined with the absence of DIO requires an optimization of the blend composition. Solar cells prepared without DIO were fabricated with PTB7-Th:PC₇₁BM blends using 1,2-dichlorobenzene (DCB) as the solvent and PFN as ETL

Chapter 5. Circumventing light-induced PCBM disorder for long lifetime PSC

(hereafter referred as DIO-free cells). Using the donor/acceptor weight ratio of 1:1.5 of the reference cells, the DIO-free cells exhibited an inferior performance with the PCE and FF averaging 7.82% and 65%, respectively. By increasing PC₇₁BM loading in the blends, an optimal performance for such DIO-free cells was obtained for a 1:2.0 weight ratio which had a best PCE of 9.6%, as seen in **Figure 5.7** and detailed photovoltaic parameters are summarized in **Table 5.2**. The improved FF and J_{sc} in higher PC₇₁BM fraction blends should be ascribed to the increased donor/acceptor interface area and the formation of ideal electron transporting channels.

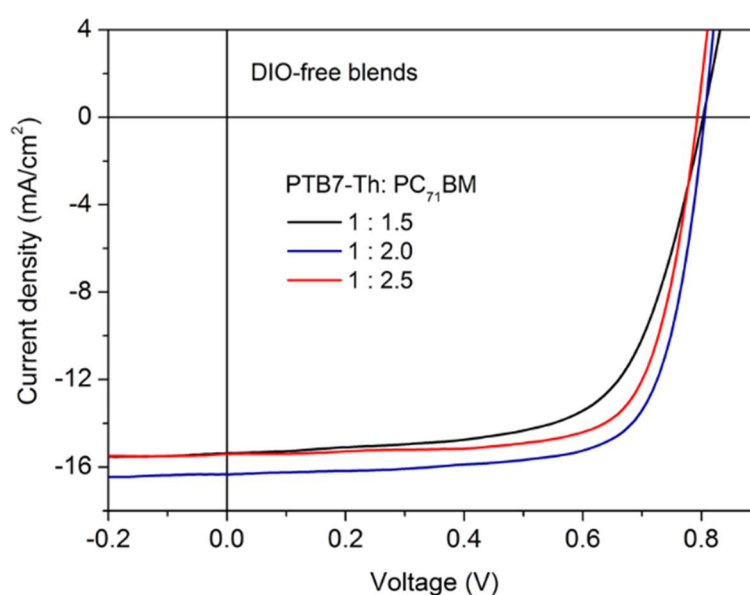


Figure 5.7. J - V curves for DIO-free cells with various PTB7-Th:PC₇₁BM ratios.

Table 5.2 Photovoltaic properties of inverted DIO-free devices fabricated with different PC₇₁BM content under AM 1.5G solar illumination at 100 mW cm⁻².

Solvent	PTB7-Th:PC ₇₁ BM (wt/wt)	J_{sc} (mA cm ⁻²)	V_{oc} (V)	FF (%)	PCE (%)
	1 : 1.5	14.93±0.29	0.802±0.003	65.28±0.60	7.82±0.17 (8.10)
DCB	1 : 2	16.01±0.22	0.802±0.002	72.28±0.78	9.28±0.17 (9.59)
	1 : 2.5	15.13±0.30	0.791±0.002	72.18±0.77	8.64±0.18 (8.94)

Chapter 5. Circumventing light-induced PCBM disorder for long lifetime PSC

As shown in **Figure 5.8a**, when a thermal annealing is applied on the completed cells, DIO-free cells exhibited excellent short-circuit current stability. In contrast, a 10% J_{sc} drop was observed in the DIO cells. DIO-free cells also show an improved PCE stability relative to reference blends, shown in **Figure 5.8b**, due to a more stable blend nano-morphology. The stable J_{sc} was confirmed by the evolution of the EQE under this treatment, shown in **Figure 5.9**.

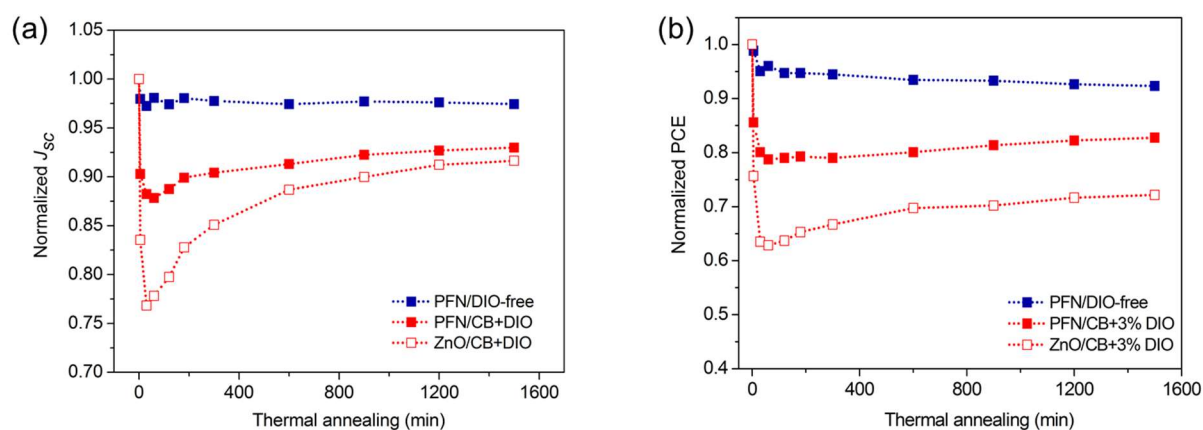


Figure 5.8 Normalized J_{sc} (a) and PCE (b) evolution for ZnO reference, PFN reference and DIO-free devices during a 25 h of thermal annealing at 85 °C in air and room light.

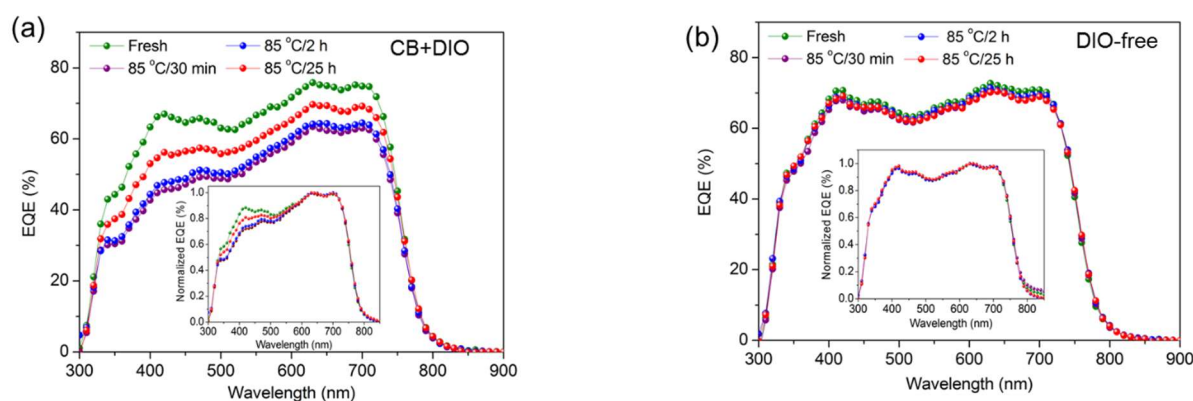


Figure 5.9. EQE evolution for (a) ITO/PFN/PTB7-Th:PC₇₁BM (1:1.5 wt%, CB+3%DIO)/MoO₃/Ag devices and (b) ITO/PFN/PTB7-Th:PC₇₁BM (1:2 wt%, DCB)/MoO₃/Ag devices with different annealing time at 85 °C.

Chapter 5. Circumventing light-induced PCBM disorder for long lifetime PSC

We observe for thermally treated DIO-free a small wavelength-independent reduction in the EQE, while a larger decrease in 340-450 nm PC₇₁BM region can be found in EQE of the reference devices. Note that the reference cell, when using SG-ZnO as ETL exhibited a large ~30% reduction in J_{sc} , when the a thermal annealing is applied only for a short period of time. When the annealing is applied for 25 hours, such reference cells are stabilized with just a 10% reduction in J_{sc} . Why there is such a large difference between the short and long annealing for the reference cell remains unclear, but the better performance of a reference cell fabricated with PFN instead of SG-ZnO may be ascribed to a stronger molecular interaction between PFN and PC₇₁BM, which further limits the mobility of PC₇₁BM molecules during the annealing process.

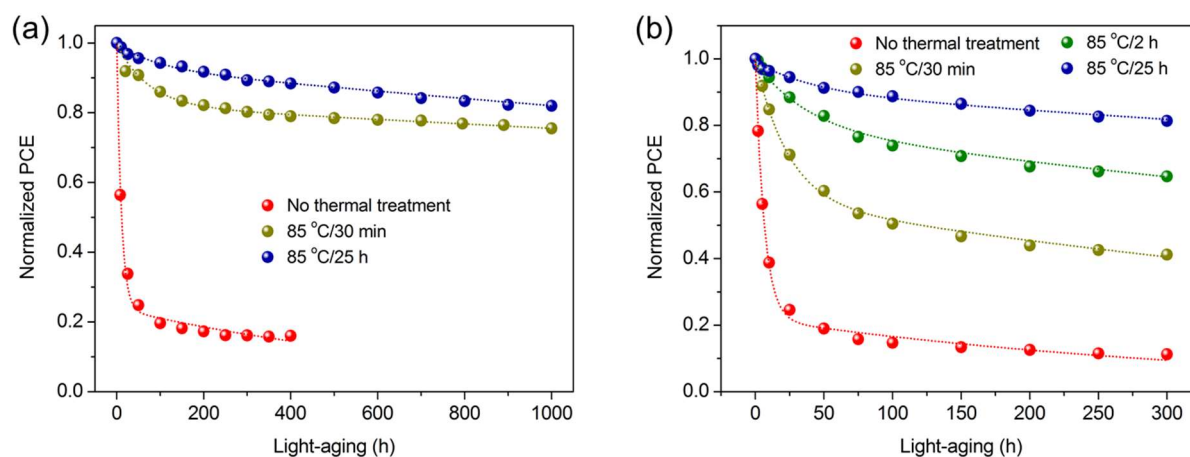


Figure 5.10 (a) Normalized PCE evolution under non-UV-filtered AM 1.5G 1-sun illumination of DIO-free devices for three different thermal annealing times. (b) Normalized PCE evolution for PFN reference devices under non-UV-filtered AM 1.5G 1-sun illumination for four different thermal annealing times.

When considering the DIO-free cells, we observe, as shown in **Figure 5.10a** and **Table 5.3**, a decreasing sensitivity to light stress as the time for thermal annealing is increased. For the longest 25 hour annealing time, the PCE versus light soaking time dynamics can be adjusted to a single exponential, indicating an almost complete

Chapter 5. Circumventing light-induced PCBM disorder for long lifetime PSC

elimination of the burn-in degradation. Indeed, the amplitude A_1 for the fast exponential decay was reduced by more than one order of magnitude. For the PFN-reference cells, we observed a similar trend when considering the normalized PCE degradation evolution under light soaking at different annealing times, as can be seen in Figure 5.10b. V_{oc} , J_{sc} and FF evolutions are also shown in **Figure 5.11**.

Table 5.3. Double-exponential decay fitting parameters for the normalized PCE profiles of ITO/PFN/PTB7-Th: PC₇₁BM/MoO₃/Ag cells under thermal annealing.

Solvent	Thermal treatment	A_1	τ_1 (h)	A_2	τ_2 (h)
CB+3%DIO	No	0.774	6.5	0.219	356.7
	85 °C/30 min	0.427	23.9	0.572	868.9
	85 °C/2 h	0.199	38.1	0.791	1471.6
	85 °C/25 h	0.089	42.2	0.902	3065.4
DIO-free	No	0.754	10.6	0.238	807.5
	85 °C/30 min	0.175	72.2	0.821	11949.7
	85 °C/25 h	0.068	94.6	0.928	8069.8

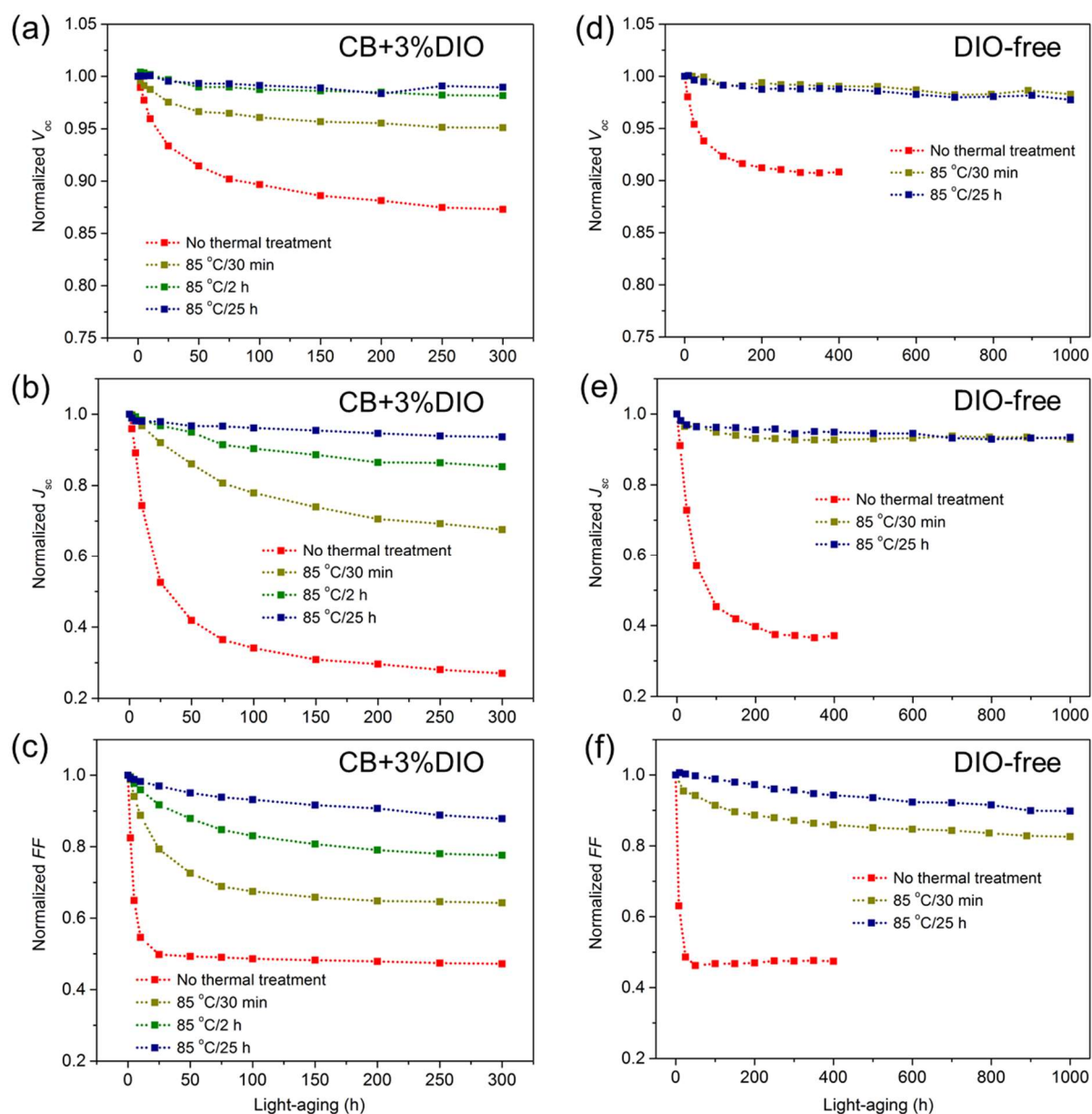


Figure 5.11. Normalized photovoltaic parameter evolutions under non-UV-filtered AM1.5G 1-sun illumination for PFN-reference cells: (a) V_{oc} , (b) J_{sc} and (c) FF , and DIO-free cells: (d) V_{oc} , (e) J_{sc} and (f) FF .

This clearly indicates that the thermal annealing is directly acting on the blend rather than on any of the buffer layers. It is worth noting that after the optimal thermal treatment, both PFN-reference cells and DIO-free cells show very stable V_{oc} even under full sun illumination and FF dominates the decay process, indicating that UV

Chapter 5. Circumventing light-induced PCBM disorder for long lifetime PSC

light induced PC₇₁BM phase disorder has been suppressed and interfacial degradation may become dominating.

To gain insight into the PC₇₁BM nano-morphology order with respect to thermal annealing, we consider grazing incidence wide-angle X-ray diffraction (GIXD) measurements on the blend films^{146,147}. The two-dimensional GIXD patterns of DIO-free blend film prior and after the 25 h thermal annealing are shown in **Figure 5.12a** and **b**, respectively. The as-cast blend film exhibited a diffuse diffraction arc at $q = 1.35 \text{ \AA}^{-1}$ with no azimuthal dependence, which suggested that the PC₇₁BM, if crystalline, were poorly ordered and randomly oriented^{143,148}. After a 25 h thermal annealing, an intense diffraction arc was visible over the whole PC₇₁BM region, indicative of a high degree of PC₇₁BM crystalline ordering. To quantify the level of order achieved, we considered, the in-plane and out-of-plane line cuts, shown in **Figure 5.12c**, and a multi-peak fitting to analyze the diffraction in the 0.9-2.2 \AA^{-1} region. A weak reflection peak (010) observed at around 1.61 \AA^{-1} in the out-of-plane direction corresponds to the PTB7-Th polymer π - π stacking. No change was observed in the full width at half maximum for either the PC₇₁BM or the PTB7-Th, indicating that their respective crystal sizes did not change after the thermal treatment. However, the relative peak areas of PC₇₁BM ($q = 1.35 \text{ \AA}^{-1}$ and $q = 1.89 \text{ \AA}^{-1}$) in the out-of-plane direction significantly increased suggesting an increase in PC₇₁BM ordering in the annealed blends. It is worth noting that a more pronounced PTB7-Th (100) peak was seen in the in-plane direction at 0.3 \AA^{-1} (**Figure 5.12c**), indicating a large number of face-on oriented crystals in the annealed sample. Moreover, a slight increase in the out-of-plane PTB7-Th (010) peak relative area was also observed after thermal annealing. Both suggest that thermal annealing promotes the crystalline order in the PTB7-Th domains, preventing large changes in the PC₇₁BM molecules positions.

Chapter 5. Circumventing light-induced PCBM disorder for long lifetime PSC

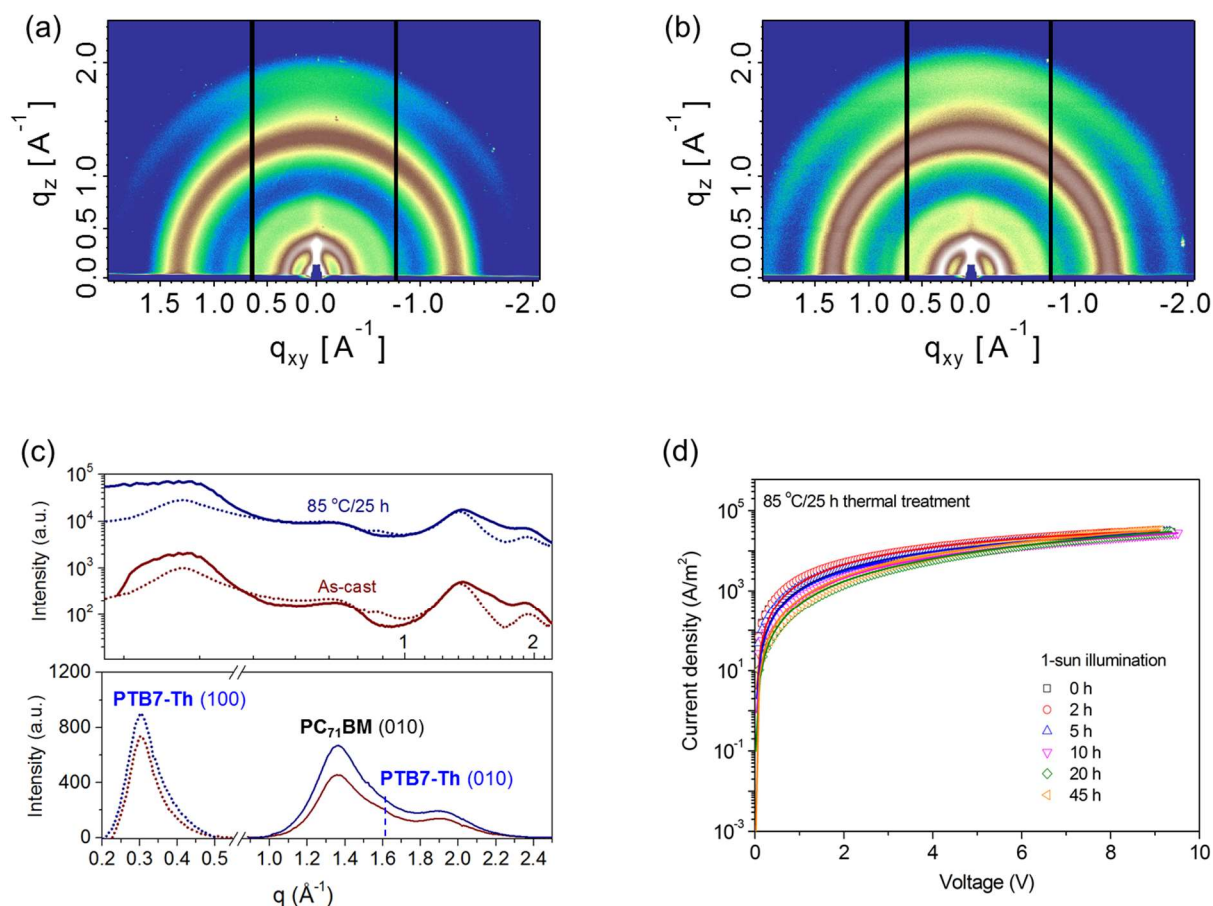


Figure 5.12. Crystalline morphology in PC₇₁BM phase. Two-dimensional GIXD patterns of the Si substrate/PFN/DIO-free active layer (a) without annealing and (b) with 25 h thermal annealing in N₂-filled glovebox. (c) Top: 1-D in-plane (dotted lines) and out-of-plane (solid lines) X-ray line-cut profiles extracted from GIXD and bottom: line-cut profiles after subtracting the baseline. (d) J - V evolution of 25 h thermally annealed ITO (135 nm)/PFN (10 nm)/PTB7-Th:PC₇₁BM (DIO-free, 100 nm)/LiF (1 nm)/Al (100 nm) electron-only devices under non-UV-filtered AM 1.5G one sun illumination.

With increased order, the PC₇₁BM anions are better confined and the excess electrostatic potential energy after photon absorption is released by a more effective charge collection at the cathode from electrons coming from singlet character anions generated directly from singlet type excitons or from triplet type anions converted into singlets by thermal excitation. In agreement with this, thermally annealed electron-

Chapter 5. Circumventing light-induced PCBM disorder for long lifetime PSC

only DIO-free devices show an excellent stability against light-stress, as seen in Figure 5.12d, confirming that electron transport channels are not destructed by full sun illumination once a high level of crystalline ordering in the PC₇₁BM domains is achieved by the thermal treatment in DIO-free blends, as schematically depicted in Figure 5.2b.

To reach high performance long lifetime cells and to further reduce the burn-in effect without any significant reduction in performance, one may filter out high energy UV photons from a Xenon light source using a GG400 filter. After re-calibration of the light intensity to 100 mW/cm² the cells exhibited an initial average PCE of 8.87% as indicated in **Table 5.4**. We monitored the performance of these cells under continuous light exposure up to 2300 h and, as shown in **Figure 5.13a**, the cells retained more than 92% of their initial PCE. In contrast, as seen in Figure 5.12a, for the non-thermally treated PFN reference cells their performance dropped by more than 20% after 500 h of light soaking.

Table 5.4 Photovoltaic parameters of inverted ITO/PFN/PTB7-Th:PC₇₁BM/MoO₃/Ag devices under AM 1.5G solar illumination at 100 mWcm⁻² and lifetimes.

<i>Solar cell type</i>		J_{sc} (mA cm ⁻²)	V_{oc} (V)	FF (%)	PCE (%)	A_1	T_{80} (h) ^a
ZnO- reference	Fresh	16.85 ± 0.15	0.801 ± 0.009	70.27 ± 0.53	9.49 ± 0.12 (9.72)	0.7985	<1
DIO-free	Fresh	16.01±0.22	0.802 ± 0.002	72.28 ± 0.78	9.28 ± 0.17 (9.59)	0.7537	~ 4
DIO-free	85 °C/ 25 h	15.70 ± 0.32	0.815 ± 0.001	68.65 ± 0.50	8.87 ± 0.19 (9.07)	0.0628 0.0327 ^c	~1500 ~ 14250 ^c

^a Lifetime T_{80} is determined by fitting normalized PCE evolutions under AM1.5G 1-sun illumination using a double-exponential decay function $PCE(t) = A_1 \cdot \exp(-t/\tau_1) + A_2 \cdot \exp(-t/\tau_2)$, where A_1 and A_2 are the amplitudes for each exponential function. τ_1 and τ_2 are the respective lifetime constants of the exponential decays. ^c A_1 and T_{80} are derived from normalized PCE decay under UV-filtered AM1.5G (GG400, $\lambda > 400$ nm) 1-sun illumination.

Chapter 5. Circumventing light-induced PCBM disorder for long lifetime PSC

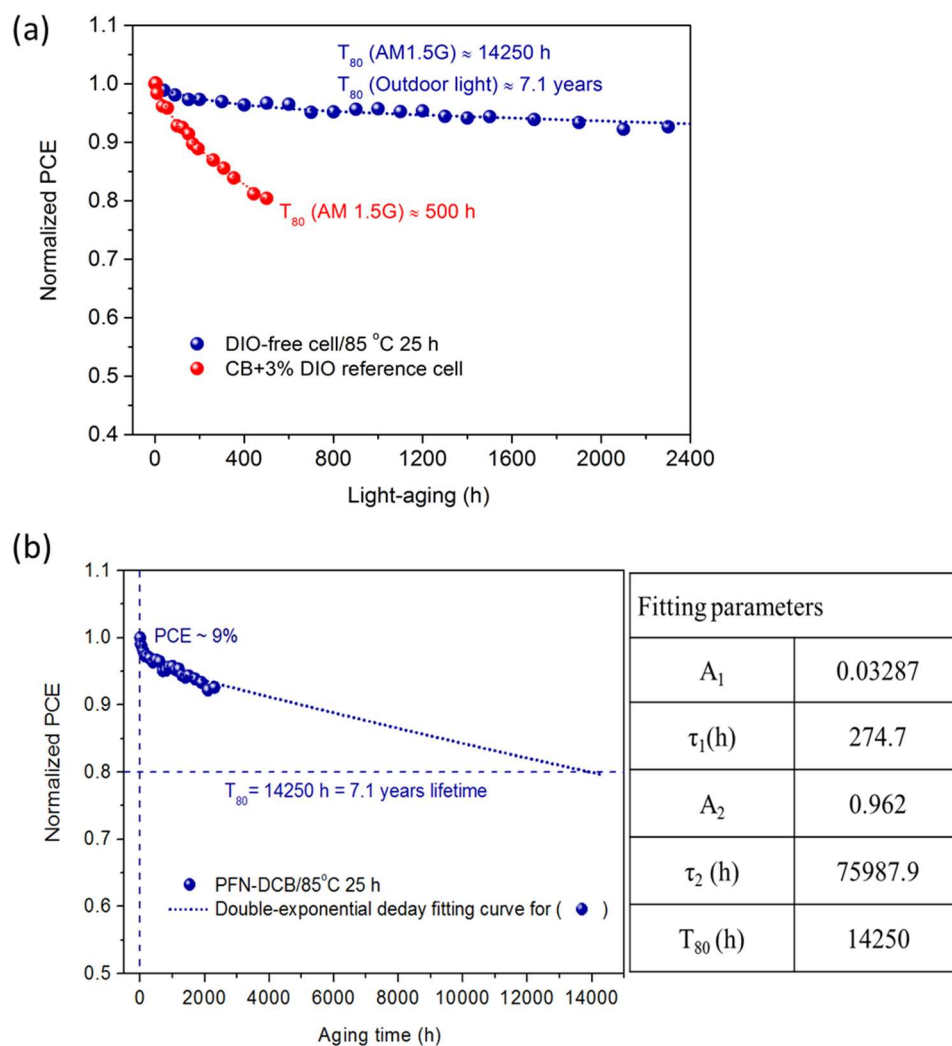


Figure 5.13. (a) Experimental (solid dots) and double exponential decay fittings (dashed lines) of normalized PCE evolutions for a 25 h thermally annealed DIO-free (blue) and a PFN reference (red) cells under a continuous UV-filtered ($\lambda > 400$ nm) AM 1.5G illumination at 100 mWcm^{-2} . Each point represents the average over six individual cells. (b) Extrapolated lifetime for the long-term light-aged cell using a double-exponential decay fitting equation.

When we extrapolated the cell performance to later times by fitting a double exponential decay to the normalized PCE evolution measured, as Seen in Figure 5.13b, we can predict a T_{80} lifetime of more than 7 years assuming that 5.5 h of continuous full sun simulator illumination correspond to one day of outdoor light soaking. Provided that when left in the dark the encapsulated cells we fabricated suffer

Chapter 5. Circumventing light-induced PCBM disorder for long lifetime PSC

virtually no degradation, for the case of vertical applications in building integrated photovoltaics where sun irradiation is reduced by approximately a 0.67 factor, the corresponding lifetime would be longer than 10 years.

5.4 Conclusions

To summarize, our results in this chapter demonstrate that in encapsulated devices, fully isolated from corrosive elements, the absorption of high-energy photons by the electron transporting PCBM molecules leads to a degradation of exciton diffusion and charge mobility in the fullerene phase. Time resolved transient absorption measurements combined with UV wavelength cut-off degradation experiments indicate that the burn-in may be triggered by a spin flip at the donor/acceptor interface, creating PC₇₁BM anions of triplet type, which result in the accumulation of electrostatic potential energy. This energy can only be dissipated through a disordering of the nano-morphology, mostly in the acceptor domains near the donor/acceptor interface. We propose a path to circumvent this problem by enhancing nano-crystalline ordering and its robustness, demonstrating that one may use high performance photovoltaic polymers and obtain very stable organic cells. We conclude that PTB7-Th:PC₇₁BM cells, with an initial PCE close to 9%, exhibit T₈₀ lifetimes as long as 7 years when under full sun light illumination. This is the longest lifetime ever reported for one sun illuminated polymer solar cells and may forge a way for the actual application of such technology. Finally, the route we provide to circumvent a degradation path intrinsic to the PC₇₁BM/donor interface may lead to an increased stability applicable to any organic or hybrid technology that uses PC₇₁BM or fullerene derivatives as an electron-transporting layer or material.

Conclusions

In the current thesis, we achieved the double goal of obtaining an optimal light absorption in PSCs without a reduction of the other photovoltaic parameters, as well as, understanding the physics behind one of the most prominent degradation paths for such type of cells to finally obtain long lifetime devices.

In Chapter 2, we demonstrated that we can construct an optical cavity to reach an optimal confinement for broadband electromagnetic waves. The combination of an insulator with a good conductor leads to the formation of an optical cavity that can be made to have a resonant character at two non-harmonic frequencies. The increase in energy storage capacity relies, precisely, in the inharmonicity of the electromagnetic field propagation within such cavity. We demonstrated that the energy confinement capacity seen remains even when the material composition is changed or the thickness of the active layer is increased, and can, in principle, be applied to reach efficiency limit performances for any kind of thin film photovoltaic device. When a high-performance PTB7-Th:PC₇₁BM blend was integrated with such optical cavity configuration, a high efficiency over 11% was achieved.

In Chapter 3, we demonstrated that the cavity concept developed in Chapter 2 is also applicable to find an optimal tradeoff between the J_{sc} and the V_{oc} . A significant enhancement in light absorption was seen for the cavity cell when half of the ITIC acceptor in the active blend was replaced by PC₇₁BM. In that event, a high efficiency

Conclusions

cell was demonstrated while maintaining the open-circuit voltage. On the other hand, the PC₇₁BM addition did not have any significant change on the device thermal stability. In addition, an almost negligible performance loss was observed compared to their glass counterparts when the TRTC device was implemented on flexible PET substrates. The approach presented may pave the ideal path to fabricate high-performance, large-area flexible solar panels for commercial applications.

PTB7-Th polymer based cells have the potential to become very stable, provided that finished devices are not under the action of strong oxidizing elements like oxygen. In Chapter 4, we showed that no degradation was observed in the light transmission spectrum from an encapsulated PTB7-Th:PC₇₁BM blend layer, even when under long-term continuous 1-sun illumination. However, for the long-term stability of such polymer solar devices, isolation from corrosive elements may not be sufficient. We demonstrated that the active removal of oxygen molecules adsorbed on the ZnO ETL and photoactive material interface increases the lifetime of high-performance low-band-gap polymer cells with improved initial photovoltaic parameters for the device.

In Chapter 5, we systematically studied the degradation dynamics of PTB7-Th:PC₇₁BM cells under different conditions. The results obtained indicate that the light-induced burn-in may be triggered by a spin flip at the donor/PC₇₁BM interface, creating PC₇₁BM anions of triplet type, which result in the accumulation of electrostatic potential energy. This energy can only be dissipated through a disordering of the nanomorphology, mostly in the PC₇₁BM domains near the donor/acceptor interface. We proposed a path to circumvent this problem by enhancing nanocrystalline ordering in the fullerene phase and its robustness, demonstrating that one may use high performance photovoltaic polymers and obtain very stable organic cells. Finally, the route we provide to circumvent a degradation path intrinsic to the PC₇₁BM/donor interface may lead to an increased stability applicable to any organic or hybrid technology that uses PC₇₁BM or fullerene derivatives as an electron-transporting layer or material.

Appendix A

Modelling sunlight harvesting in planar thin film solar cells.

The propagation of light through 1-D thin film cell stacks can be modeled by using the transfer matrix formalism (TMF). This is the model that we have used in the current thesis to estimate or analyze light absorption in the cell devices we considered.

In the TMF model, all the layers in the stack are considered homogeneous and isotropic, and interfaces between adjacent layers are assumed optically smooth. In order to correctly analyze a solar, incorporating an anti-reflection coating (ARC) formed with one or several nanometer thick layers on the front side of the glass substrate, we implemented a TMF model in two parts. We consider a coherent superposition of the fields between the second substrate interface and the back electrode and within the ARC. Two such coherent propagations are connected by a thick glass substrate, where we sum over the intensities instead of amplitudes, as seen in **Figure A.1**.

To determine the electromagnetic field distribution, the numerical computation is performed backwards, i.e. starting from the interface between the air and the last layer

Appendix A. Modelling sunlight harvesting in planar thin film solar cells

of the stack. Boundary conditions are also shown in Figure 1.8, where the forward electric field E_F^+ in the medium adjacent to the last cell layer is set to 1 and the backward electric field E_F^- is set to zero, provided that no light enters from the right-hand side of the structure. Then, the electric fields for each subsequent layer are calculated in a sequential manner using the following matrix:

$$\begin{pmatrix} A & B \\ C & D \end{pmatrix} = \frac{0.5}{k_{z,n-1}} \begin{bmatrix} (k_{z,n-1} + k_{z,n})e^{-ik_{z,n-1}d_{n-1}} & (k_{z,n-1} - k_{z,n})e^{-ik_{z,n-1}d_{n-1}} \\ (k_{z,n-1} - k_{z,n})e^{ik_{z,n-1}d_{n-1}} & (k_{z,n-1} + k_{z,n})e^{ik_{z,n-1}d_{n-1}} \end{bmatrix} \quad (\text{A.1})$$

$$\begin{pmatrix} E_{n-1}^+ \\ E_{n-1}^- \end{pmatrix} = \begin{pmatrix} A & B \\ C & D \end{pmatrix} \begin{pmatrix} E_n^+ \\ E_n^- \end{pmatrix} \quad (\text{A.2})$$

where $k_{z,n}$ is the complex wavenumber and d_n the thickness for the n layer. From the field amplitudes E_0^+ and E_0^- , one can obtain their corresponding intensities $|E_0^+|^2$ and $|E_0^-|^2$, respectively, which are used to determine the incident and transmitted intensities at the substrate-ARC interface. Note that these two intensities should be treated separately and multiple reflections within the substrate must be properly accounted for. Once $|E_{AS}^+|^2$ and $|E_{AS}^-|^2$ are known, one may again apply the TMF within the ARC, and finally obtain the incident and reflected fields of the entire structure including the cell, substrate and ARC. Once the field amplitudes for the electric fields within the active layer are determined one may easily compute the absorbed energy¹⁴⁹ and finally the short circuit current using equations 1.2 and 1.4 in Section 1.2.

Appendix A. Modelling sunlight harvesting in planar thin film solar cells

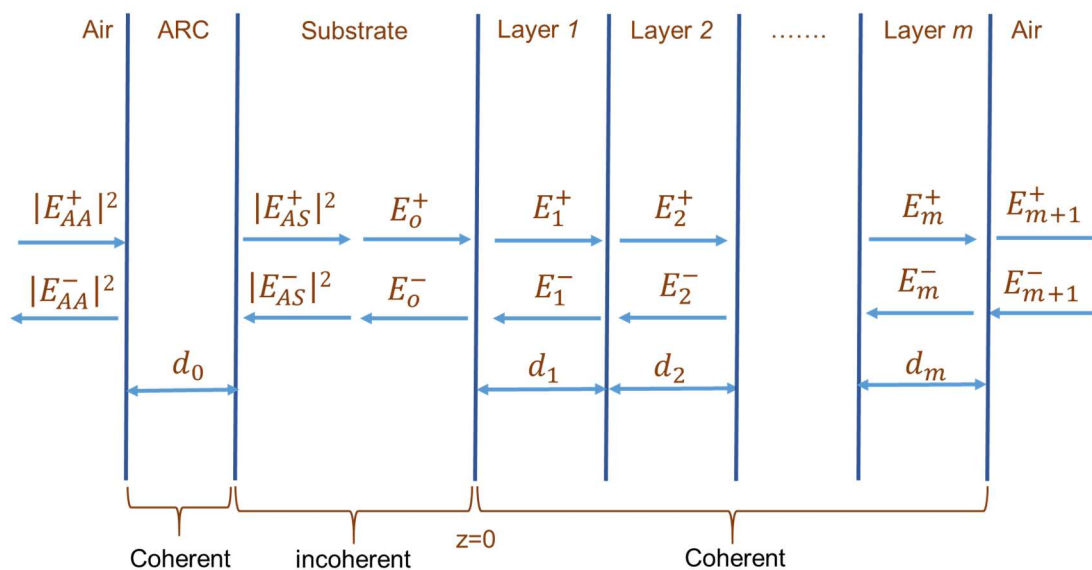


Figure A.1. Forward- and backward-propagating electric field amplitudes (E) to determine light absorption in the organic solar cell stack with. The substrate normally corresponds to a thick glass (1.1 mm) and light propagation within it is treated as incoherent. Light propagation within the cell and the layer in front of the glass, considered as an ARC, is treated as coherent.

As will be indicated below in all the optical simulations reported in the current thesis, we only consider the case of perpendicular incidence. When estimating the optimal cell architecture, we followed an inverse integration approach where a large set of possible solutions was numerically computed for a given group of input parameters, such as a range of thicknesses and/or optical constants for some of the layers. The target solution was the one maximizing the photocurrent of the solar cell and was selected from the set of all possible solutions.

Appendix B


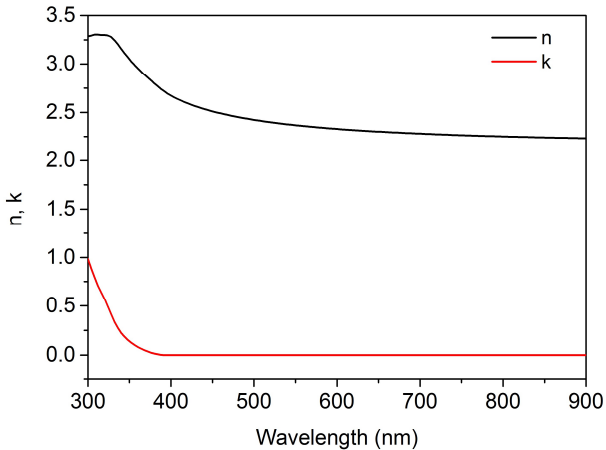
Materials and methods

This appendix summarizes most of the critical materials used in the thesis, including transparent TRTC conductive electrodes, photoactive materials, electron transporting materials and anti-reflection coating, as well as their corresponding deposition methods. The fundamental properties and optical constants of the materials are also shown in the below tables.


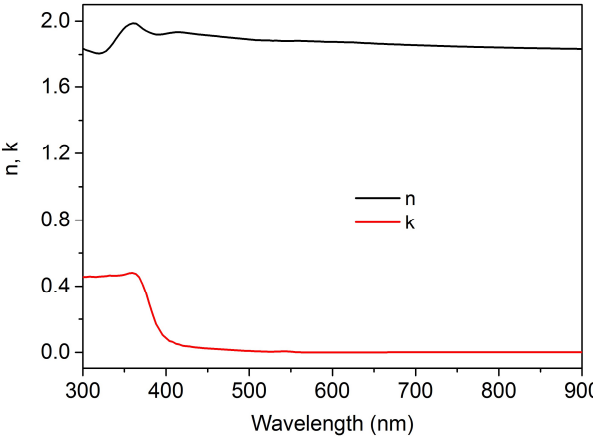
B.1 TRTC electrodes

TRTC electrodes consisting of DCL (TiO₂, ZnO, MoO₃, or Al₂O₃)/ZnO (5 nm)/MCL (Ag)/ZnO (3 or 5 nm) multilayers were sequentially deposited by magnetron sputtering (Aja International Inc.) at room temperature. The sputtering chamber was initially evacuated to a base pressure of $\sim 10^{-6}$ mtorr. The target-to-substrate distance was maintained at 30 cm and the holder was rotated at a speed of 60 rpm. TiO₂ and ZnO were sputtered using a RF power supply in a pure Ar atmosphere, while Al₂O₃, MoO₃ and Ag were deposited using a DC power supply in a mixture of Ar/O₂ with different flux ratios. The details are shown in below tables.

Appendix B. Materials and methods

Titanium dioxide (TiO ₂)																					
																					
<p>Kurt J. Lesker, TiO₂ target 2.00" Dia. × 0.250" Thick, 99.99%</p>																					
<p>Deposition method: RF sputtering</p> <p>Deposition details: TiO₂ dielectric cavity layer was fabricated on pre-cleaned fused silica (n=1.45) or N-SK10 (n=1.62) glass substrates, or PET flexible plastic substrates. TiO₂ layers were deposited in a pure Ar atmosphere using 2-inch TiO₂ target. The deposition power and rate are 80 W and 0.05 Å/s, respectively.</p> <p>Recipe:</p> <table border="1"> <thead> <tr> <th>Deposition temperature (°C)</th> <th>Room temperature</th> </tr> </thead> <tbody> <tr> <td>Target-to-substrate distance (cm)</td> <td>30</td> </tr> <tr> <td>Deposition gas/flow (sccm)</td> <td>Ar /20</td> </tr> <tr> <td>Power strike (W)</td> <td>40</td> </tr> <tr> <td>Pressure strike (mTorr)</td> <td>40</td> </tr> <tr> <td>Ramp up (sec)</td> <td>10</td> </tr> <tr> <td>Deposition power (W)</td> <td>80</td> </tr> <tr> <td>Deposition pressure (mTorr)</td> <td>3</td> </tr> <tr> <td>Deposition rate (Å/s)</td> <td>0.05</td> </tr> <tr> <td>Ramp down (sec)</td> <td>30</td> </tr> </tbody> </table>		Deposition temperature (°C)	Room temperature	Target-to-substrate distance (cm)	30	Deposition gas/flow (sccm)	Ar /20	Power strike (W)	40	Pressure strike (mTorr)	40	Ramp up (sec)	10	Deposition power (W)	80	Deposition pressure (mTorr)	3	Deposition rate (Å/s)	0.05	Ramp down (sec)	30
Deposition temperature (°C)	Room temperature																				
Target-to-substrate distance (cm)	30																				
Deposition gas/flow (sccm)	Ar /20																				
Power strike (W)	40																				
Pressure strike (mTorr)	40																				
Ramp up (sec)	10																				
Deposition power (W)	80																				
Deposition pressure (mTorr)	3																				
Deposition rate (Å/s)	0.05																				
Ramp down (sec)	30																				

Appendix B. Materials and methods

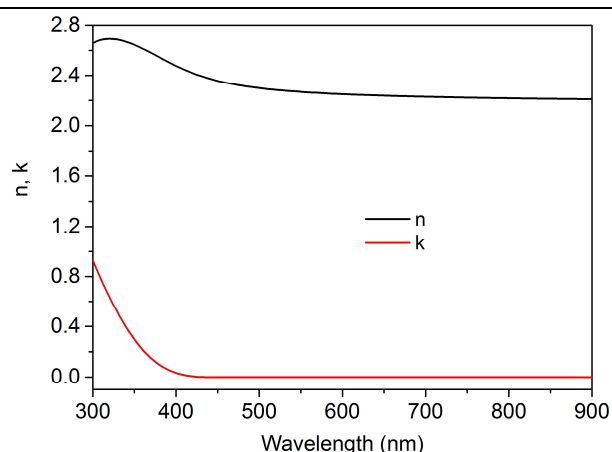
Zinc Oxide (ZnO)																					
 <p>Kurt J. Lesker, ZnO target 2.00" Dia. × 0.250" Thick, 99.999%</p>																					
<p>Deposition method: RF sputtering</p>																					
<p>Deposition details: ZnO was fabricated on the top and bottom of Ag metallic cavity layer by RF magnetron sputtering. ZnO layers were deposited in a pure Ar atmosphere using 2-inch ZnO target. The deposition power and rate are 50W and 0.11 Å/min, respectively.</p>																					
<p>Recipe:</p>																					
<table border="1"> <tr> <td>Deposition temperature (°C)</td> <td>Room temperature</td> </tr> <tr> <td>Target-to-substrate distance (cm)</td> <td>30</td> </tr> <tr> <td>Deposition gas/flow (sccm)</td> <td>Ar /20</td> </tr> <tr> <td>Power strike (W)</td> <td>40</td> </tr> <tr> <td>Pressure strike (mTorr)</td> <td>40</td> </tr> <tr> <td>Ramp up (sec)</td> <td>10</td> </tr> <tr> <td>Deposition power (W)</td> <td>50</td> </tr> <tr> <td>Deposition pressure (mTorr)</td> <td>3</td> </tr> <tr> <td>Deposition rate (Å/min)</td> <td>0.11</td> </tr> <tr> <td>Ramp down (sec)</td> <td>10</td> </tr> </table>	Deposition temperature (°C)	Room temperature	Target-to-substrate distance (cm)	30	Deposition gas/flow (sccm)	Ar /20	Power strike (W)	40	Pressure strike (mTorr)	40	Ramp up (sec)	10	Deposition power (W)	50	Deposition pressure (mTorr)	3	Deposition rate (Å/min)	0.11	Ramp down (sec)	10	
Deposition temperature (°C)	Room temperature																				
Target-to-substrate distance (cm)	30																				
Deposition gas/flow (sccm)	Ar /20																				
Power strike (W)	40																				
Pressure strike (mTorr)	40																				
Ramp up (sec)	10																				
Deposition power (W)	50																				
Deposition pressure (mTorr)	3																				
Deposition rate (Å/min)	0.11																				
Ramp down (sec)	10																				
<table border="1"> <tr> <td>Target-to-substrate distance (cm)</td> <td>30</td> </tr> </table>	Target-to-substrate distance (cm)	30																			
Target-to-substrate distance (cm)	30																				
<table border="1"> <tr> <td>Deposition gas/flow (sccm)</td> <td>Ar /20</td> </tr> </table>	Deposition gas/flow (sccm)	Ar /20																			
Deposition gas/flow (sccm)	Ar /20																				
<table border="1"> <tr> <td>Power strike (W)</td> <td>40</td> </tr> </table>	Power strike (W)	40																			
Power strike (W)	40																				
<table border="1"> <tr> <td>Pressure strike (mTorr)</td> <td>40</td> </tr> </table>	Pressure strike (mTorr)	40																			
Pressure strike (mTorr)	40																				
<table border="1"> <tr> <td>Ramp up (sec)</td> <td>10</td> </tr> </table>	Ramp up (sec)	10																			
Ramp up (sec)	10																				
<table border="1"> <tr> <td>Deposition power (W)</td> <td>50</td> </tr> </table>	Deposition power (W)	50																			
Deposition power (W)	50																				
<table border="1"> <tr> <td>Deposition pressure (mTorr)</td> <td>3</td> </tr> </table>	Deposition pressure (mTorr)	3																			
Deposition pressure (mTorr)	3																				
<table border="1"> <tr> <td>Deposition rate (Å/min)</td> <td>0.11</td> </tr> </table>	Deposition rate (Å/min)	0.11																			
Deposition rate (Å/min)	0.11																				
<table border="1"> <tr> <td>Ramp down (sec)</td> <td>10</td> </tr> </table>	Ramp down (sec)	10																			
Ramp down (sec)	10																				

Appendix B. Materials and methods

Molybdenum Oxide (MoO₃)



Kurt J. Lesker, Mo target
2.00" Dia. × 0.250" Thick, 99.95%




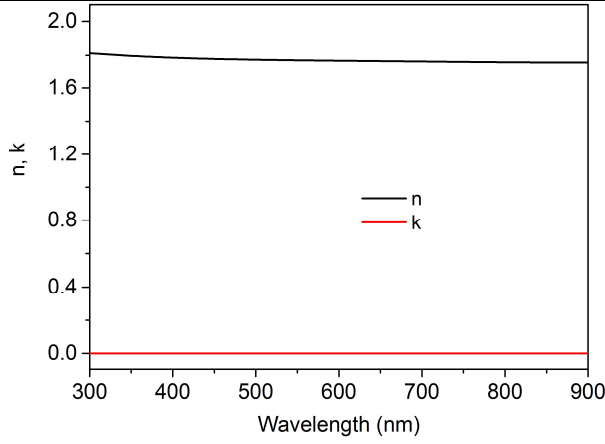
Deposition method: DC reactive sputtering

Deposition details: MoO₃ DCL was fabricated on the top of pre-cleaned fused silica substrates by DC reactive magnetron sputtering. MoO₃ layers were deposited in a O₂: Ar (20:5) atmosphere using 2-inch Mo target and also assisted by RF bias of 50W. The deposition power and rate are 150W and 0.67 Å/min, respectively.

Recipe:

Deposition temperature (°C)	Room temperature
Target-to-substrate distance (cm)	30
Deposition gas/flow (sccm)	Ar:O ₂ /5:20
Power strike (W)	40
Pressure strike (mTorr)	10
Ramp up (sec)	10
Deposition power (W)	150
RF bias (W)	50
Deposition pressure (mTorr)	3
Deposition rate (Å/min)	0.26
Ramp down (sec)	50

Appendix B. Materials and methods

Aluminum Oxide (Al ₂ O ₃)																					
																					
<p>Kurt J. Lesker, Al target 2.00" Dia. × 0.250" Thick, 99.99%</p>																					
<p>Deposition method: DC reactive sputtering</p> <p>Deposition details: Al₂O₃ DCL was fabricated on the top of pre-cleaned fused silica substrates by DC reactive magnetron sputtering. Al₂O₃ layers were deposited in a Ar: O₂ (20:6) atmosphere using 2-inch Al target. The deposition power and rate are 150W and 2.0 Å/min, respectively.</p> <p>Recipe:</p> <table border="1"> <tbody> <tr> <td>Deposition temperature (°C)</td> <td>Room temperature</td> </tr> <tr> <td>Target-to-substrate distance (cm)</td> <td>30</td> </tr> <tr> <td>Deposition gas/flow (sccm)</td> <td>Ar:O₂/20:6</td> </tr> <tr> <td>Power strike (W)</td> <td>40</td> </tr> <tr> <td>Pressure strike (mTorr)</td> <td>10</td> </tr> <tr> <td>Ramp up (sec)</td> <td>10</td> </tr> <tr> <td>Deposition power (W)</td> <td>150</td> </tr> <tr> <td>Deposition pressure (mTorr)</td> <td>3</td> </tr> <tr> <td>Deposition rate (Å/min)</td> <td>2.0</td> </tr> <tr> <td>Ramp down (sec)</td> <td>50</td> </tr> </tbody> </table>		Deposition temperature (°C)	Room temperature	Target-to-substrate distance (cm)	30	Deposition gas/flow (sccm)	Ar:O ₂ /20:6	Power strike (W)	40	Pressure strike (mTorr)	10	Ramp up (sec)	10	Deposition power (W)	150	Deposition pressure (mTorr)	3	Deposition rate (Å/min)	2.0	Ramp down (sec)	50
Deposition temperature (°C)	Room temperature																				
Target-to-substrate distance (cm)	30																				
Deposition gas/flow (sccm)	Ar:O ₂ /20:6																				
Power strike (W)	40																				
Pressure strike (mTorr)	10																				
Ramp up (sec)	10																				
Deposition power (W)	150																				
Deposition pressure (mTorr)	3																				
Deposition rate (Å/min)	2.0																				
Ramp down (sec)	50																				

Appendix B. Materials and methods

B.2 Photoactive materials

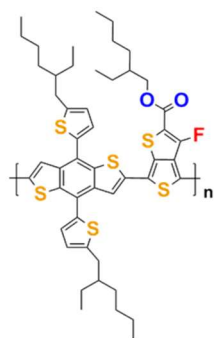
In this thesis, we consider BHJ blends of polymer donor: small molecular acceptor as photoactive layers, which are fabricated by a spin-coating technique. The experimental details and their optical constants are shown below.

Appendix B. Materials and methods

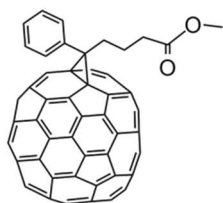
PTB7-Th: PC₇₁BM BHJ blend:

Poly[4,8-bis(5-(2-ethylhexyl)thiophen-2-yl)benzo[1,2-b;4,5-b']dithiophene-2,6-diyl-alt-(4-(2-ethylhexyl)-3-fluorothieno[3,4-b]thiophene-)-2-carboxylate-2-6-diyl]

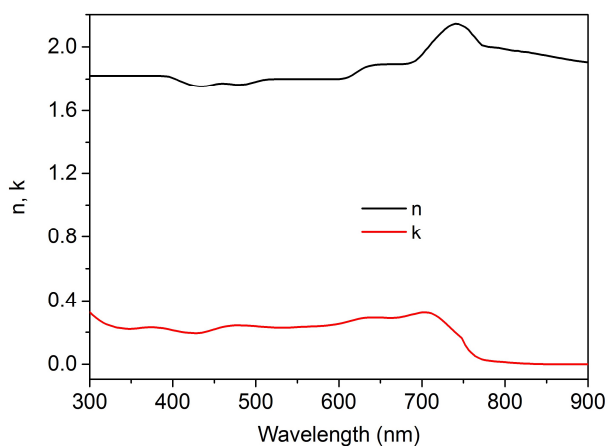
(PTB7-Th): [6,6]-phenyl C₇₁ butyric acid methyl ester (PC₇₁BM)



PTB7-Th



PC₇₁BM



Deposition method: Spin-coating

Deposition details: The polymer PTB7-Th (1-material) and PC₇₁BM (purity > 99%, American Dye Source) were used as received without further purification. Solutions of PTB7-Th: PC₇₁BM (1.0:1.5 by weight) with a total concentration of 25 mg/mL were prepared in chlorobenzene and stirred at 60 °C overnight in N₂-filled glovebox and additive 1, 8-Diiodooctane (DIO, 3 % Vol) or 1, 6-Diodohexane (DIH, 3.5% Vol) was added one hour prior to spin-coating.

Recipe guide:

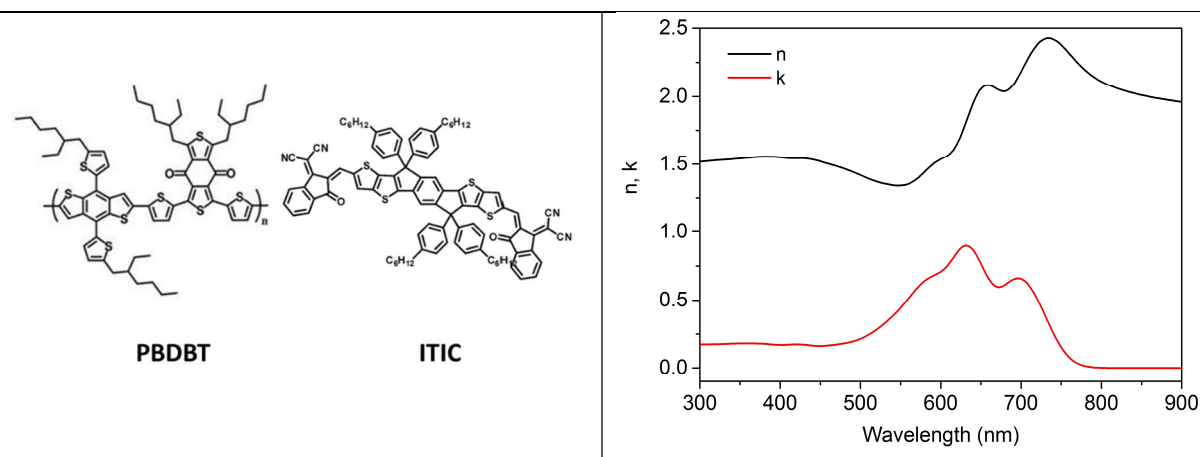
Ramp 1 (sec)	1	1	1
Speed 1 (rpm)	2000	1400	1000
Dwell 1 (sec)	60	60	60
Thickness (nm)	~95-100	~120	~140

After spin-coating, the resulting photoactive films with controlled thickness were dried in vacuum ($< 5 \times 10^{-6}$ mbar) for at least one hour to remove additive and residue solvent. For the stable blend, PTB7-Th: PC₇₁BM = 1:2 wt/wt were dissolved in DCB with total concentration of 36 mg/mL. Spin-coating such blends at speed of 1250 rpm will give around 100 nm thick active layer.

Appendix B. Materials and methods

PBDBT:ITIC BHJ blend:

Poly[(2,6-(4,8-bis(5-(2-ethylhexyl)thiophen-2-yl)-benzo[1,2-b:4,5-b']dithiophene))-alt-(5,5-(1',3'-di-2-thienyl-5',7'-bis(2-ethylhexyl)benzo[1',2'-c:4',5'-c']dithiophene-4,8-dione)] (PBDBT): 3,9-bis(2-methylene-(3-(1,1-dicyanomethylene)-indanone))-5,5,11,11-tetrakis(4-hexylphenyl)-dithieno[2,3-d:2',3'-d']-s-indaceno[1,2-b:5,6-b']dithiophene (ITIC)



Deposition method: Spin-coating

Deposition details: The polymer PBDBT and ITIC were purchased from 1-material and used as received without further purification. Solutions of PBDBT: ITIC (1.0:1.0 by weight) with a total concentration of 20 mg/mL were prepared in chlorobenzene and stirred at 50 °C overnight in N₂-filled glovebox and additive 1, 8-Diiodooctane (DIO, 0.5 % Vol) was added one hour prior to spin-coating.

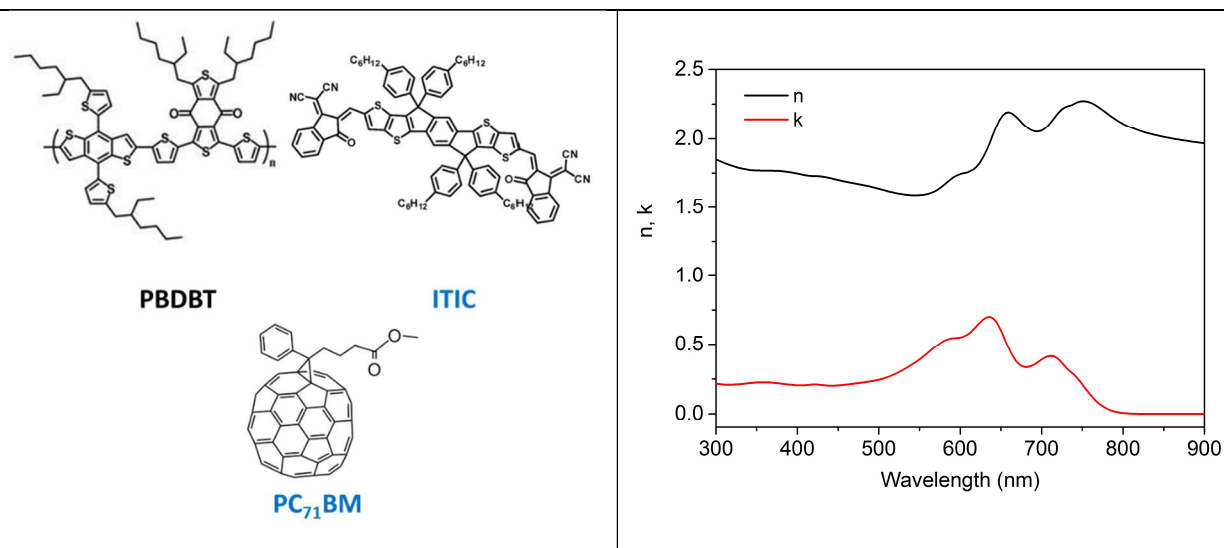
Recipe guide:

Ramp 1 (sec)	1	1
Speed 1 (rpm)	2000	1500
Dwell 1 (sec)	60	60
Thickness (nm)	~95-100	~120

After spin-coating, the resulting photoactive films with controlled thickness were dried in vacuum ($< 5 \times 10^{-6}$ mbar) for at least one hour and afterwards, thermally annealed at 140 °C for 10 min.

Appendix B. Materials and methods

PBDBT:ITIC:PC₇₁BM (1:0.5:0.5) ternary BHJ blends:



Deposition method: Spin-coating

Deposition details:

Solutions of PBDBT:ITIC:PC₇₁BM (1.0:0.5:0.5 by weight) with a total concentration of 20 mg/mL were prepared in chlorobenzene and stirred at 50 °C overnight in N₂-filled glovebox and additive 1, 8-Diiodooctane (DIO, 1.0 % Vol) was added one hour prior to spin-coating.

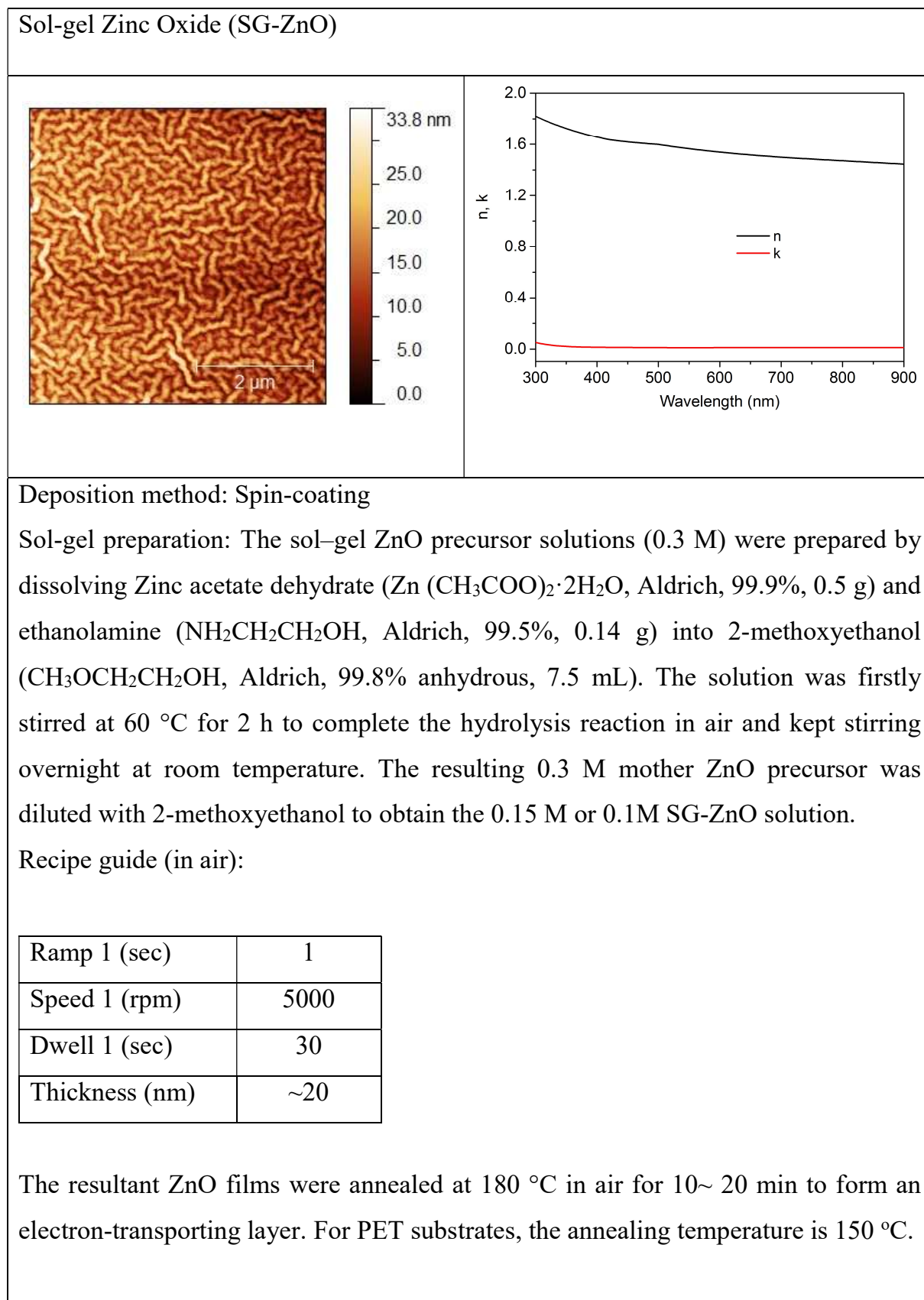
Recipe guide:

Ramp 1 (sec)	1
Speed 1 (rpm)	2000
Dwell 1 (sec)	60
Thickness (nm)	~95-100

After spin-coating, the resulting photoactive films with controlled thickness were dried in vacuum ($< 5 \times 10^{-6}$ mbar) for at least one hour and afterwards, thermally annealed at 80 °C for 10 min.

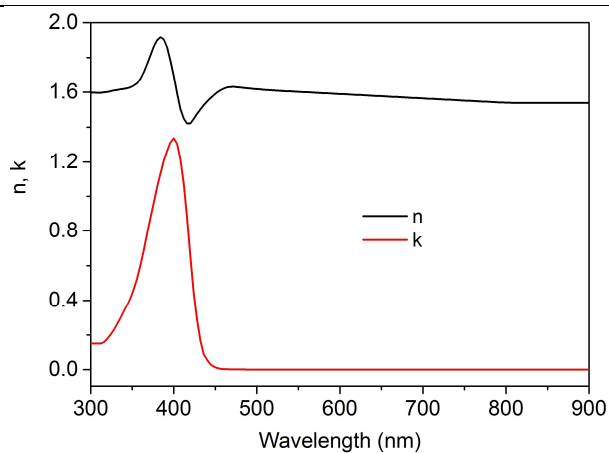
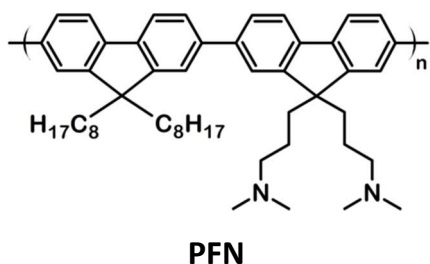
Appendix B. Materials and methods

B.3 Electron-transporting layers



Appendix B. Materials and methods

Poly[(9,9-bis(3'-(N,N-dimethylamino)propyl)-2,7-fluorene)-alt-2,7-(9,9-dioctylfluorene)] (PFN)



Deposition method: Spin-coating

Solution preparation: PFN (1-Material) was dissolved in methanol (1.0 mg mL⁻¹) in the presence of small amount of acetic acid (10 μL mL⁻¹), which was filtered with 0.45 μm PTFE filter prior to use.


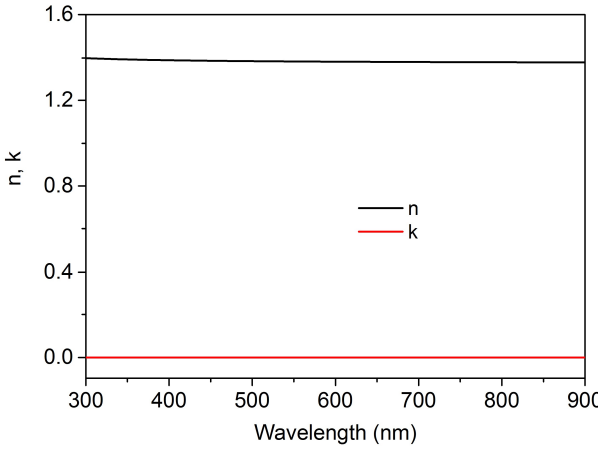
Recipe guide (in glovebox):

Ramp 1 (sec)	3
Speed 1 (rpm)	3000
Dwell 1 (sec)	60
Thickness (nm)	~10

The PFN film was annealed at 70 °C for 5 min in glovebox and the resulting thickness of the layer was around 10 nm.

Appendix B. Materials and methods

B.4. Anti-reflection coating (ARC)

Magnesium Fluoride (MgF_2)	
	
Kurt J. Lesker, MgF_2 pellets 3mm - 6mm Pieces, 99.9%	
Deposition method: Thermal evaporation	
Deposition details: ~100 nm thick MgF_2 layers were thermal evaporated on the top of TCE glass substrates to form ARC to reduce the glass reflectance.	
Recipe guide:	
Power 1 (%)	7
Ramp 1 (sec)	30
Soak time 1 (sec)	100
Power 2 (%)	14
Ramp 2 (sec)	30
Soak time 2 (sec)	200
Deposition Rate ($\text{\AA}/\text{s}$)	0.8~1.0
Tooling factor (%)	28

Appendix C

Single-carrier device fabrication and characterization

Hole- and electron-only device fabrication: configurations of ITO/PEDOT: PSS/PTB7-Th: PC₇₁BM/MoO₃/Ag and ITO/ZnO (or PFN)/PTB7-Th: PC₇₁BM/LiF/Al were used for hole-only and electron-only devices in this thesis, respectively. PEDOT:PSS (AI 4083, ~40 nm) was spin-coated on precleaned ITO substrates at 4000 rpm with 700 rpm acceleration for 40 s, and annealed in air at 140 °C for 20 min. LiF (1 nm) and Al (100 nm) were deposited by thermal evaporation with deposition rate of 0.1 Å/s and 1 Å/s, respectively. The processing conditions for other materials were identical to those of corresponding solar cells.

Characterization: The mobilities were extracted by fitting the dark J - V characteristics of single charge carrier devices using the SCLC Mott–Gurney model^{140,141},

$$J = \frac{9}{8} \varepsilon_r \varepsilon_0 \mu_0 \frac{(V - V_{bi})^2}{L^3} \exp\left(\beta \sqrt{\frac{V - V_{bi}}{L}}\right)$$

Appendix C. Single-carrier device fabrication and characterization

Where ϵ_0 is the permittivity of free space (8.8542×10^{-12} F/m), ϵ_r is the relative permittivity of the PTB7-Th photoactive material (assumed to be 3.5), V_{bi} is the built-in voltage (determined to be 0.1 V for the hole-only device and 0.1 V for the electron-only device, respectively). L is the thickness of the active layer (100 nm) and the sheet resistance of ITO substrates is $\sim 15 \Omega$. μ_0 the zero-field mobility, and β the field activation factor.

Appendix D

Two-exponential PSC degradation dynamics

Under illumination, most of the currently studied state of the art PSCs exhibit a large performance loss in the initial aging stages and reduced decay over longer timescales, as schematically seen in **Figure D.1**. One may introduce a two-exponential function, which can describe the time-dependent changes in solar cell performance and can be used to estimate the approximate lifetime.

$$\text{Normalized PCE}(t) = A_1 \cdot \exp(-t/\tau_1) + A_2 \cdot \exp(-t/\tau_2)$$

where A_1 and A_2 are the amplitudes for each exponential function, while τ_1 and τ_2 are the respective lifetime constants of the exponential decays. The sum of A_1 and A_2 should be equal to unity at the starting time $t = 0$. By fitting the experimental decay under AM1.5G 1-sun illumination to this double exponential behavior, the corresponding amplitudes and decay times can be determined. Then, one may estimate the, T_{80} lifetime, which is the time for the PCE to degrade to 80% of its initial value.

Appendix D. Two-exponential PSC degradation dynamics

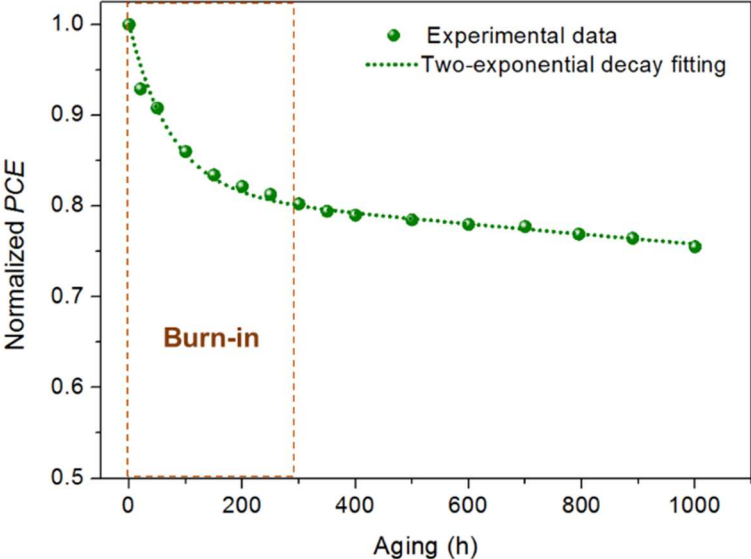


Figure D.1. Typical normalized PCE decay for an encapsulated organic solar cell under continuous light illumination. The dotted line represents the best fit to the experimental data using a two-exponential decay function.

Appendix E

Transient absorption measurement

Time resolved transient absorption measurements were performed with a non-colinear femtosecond pump-probe setup. A simplified scheme of this setup is shown in **Figure E.1**. Laser pulses with a 765 nm wavelength, a 120 fs duration and a 1 kHz repetition rate were emitted by a Coherent Legend F regenerative amplifier which used a diode-pumped, intra-cavity doubled Coherent Evolution 15 laser (527 nm, 200 ns, 1kHz) as seed, and a titanium sapphire Coherent Mira 900 F laser (765 nm, 200 fs, 76 MHz) as pump. The Mira 900 F laser was pumped by a continuous-wave diode-pumped Coherent Verdi V6 laser (532 nm). These four components form the laser setup labelled (1) on Figure E.1.

Appendix E. Transient absorption measurement

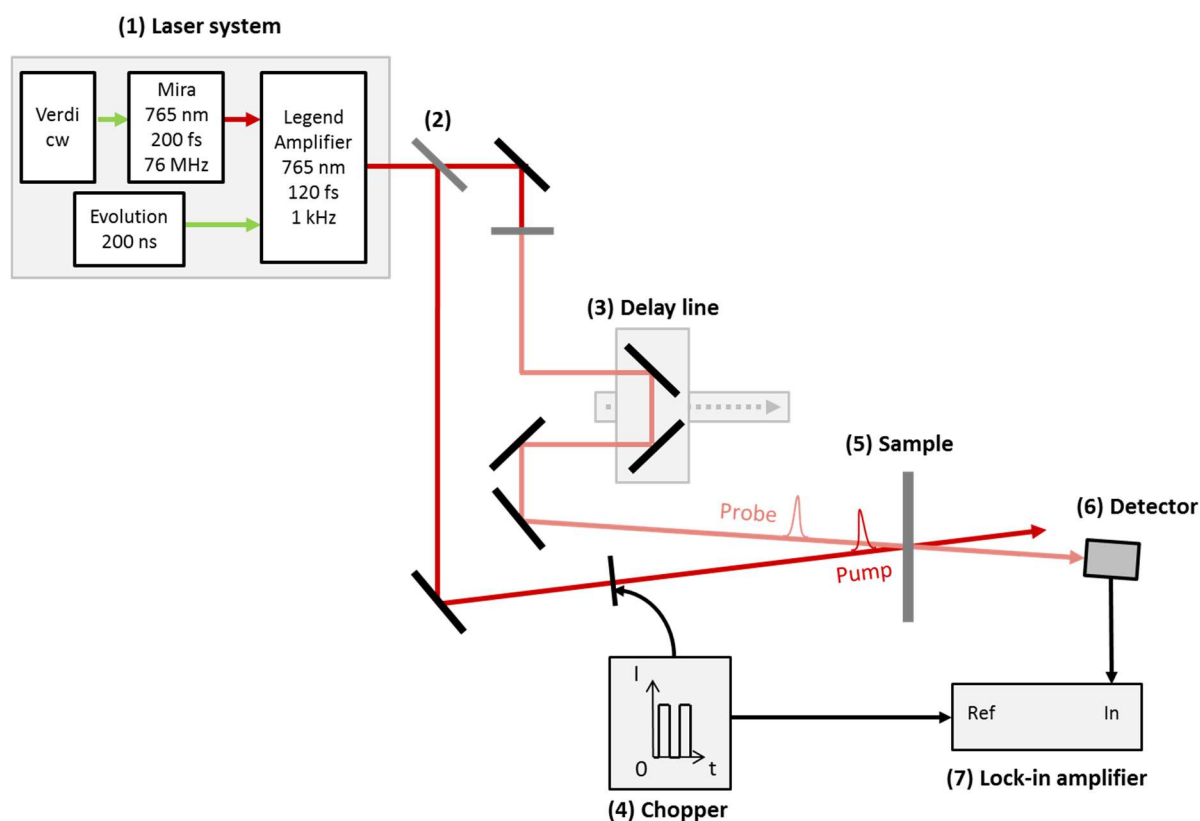


Figure E.1. Simple scheme of the pump-probe setup

The light emitted by the regenerative amplifier was separated with a beam splitter (2) into a pump beam and a probe beam. These two beams crossed at the sample surface after the probe beam was passed through a mechanical delay line with an adjustable length (3). This allowed to control the delay between the probe and pump pulses at the sample surface with a resolution in the range of 10 ps. The pump beam was modulated before it reached the sample with a mechanical chopper (4) at a 500 Hz frequency. The probe light transmitted by the sample (5) was detected by a silicon photodiode (6) connected to a lock-in amplifier (7) which used as reference the mechanical chopper. Using this detection configuration, the change in the absorption of the probe beam induced by the pump was measured for a given delay between them, and the measurement was repeated for different positions of the delay line so that the temporal profile of the sample's transient absorption could be captured. Note that, in order to minimize the parasitic detection of scattered pump light, a waveplate was placed

Appendix E. Transient absorption measurement

across the pump beam before it reaches the sample, and a polarizer was placed at the photodiode window.

In our experimental setup, the probe and pump beams had, by default, the same wavelength as the light emitted by the regenerative amplifier (765 nm). In order to pump the sample at a UV wavelength (382.5 nm) instead of a 765 nm wavelength (probing being still done at a 765 nm wavelength), a non-linear doubler crystal was placed across the beam, and the remaining 765 nm radiation in the pump beam was stopped before it reaches the sample using a low pass filter. The pump pulses impinging onto the sample had an energy of 2 μJ for both the 765 nm and 382.5 nm pump wavelengths.

Reference

- ¹ Earth's CO₂ Home Page. <https://www.co2.earth>.
- ² OECD Environmental Outlook to 2050: The consequences of inaction. organisation for economic co-operation and development (OECD) (2012). <http://dx.doi.org/10.1787/9789264122246-en>.
- ³ BP energy outlook (2017). <http://www.bp.com/en/global/corporate/energy-economics/energ-outlook.html>.
- ⁴ Renewables 2016 Global Status Report. <http://www.ren21.net/status-of-renewables/global-status-report>.
- ⁵ NREL (2017), http://www.nrel.gov/pv/assets/images/efficiency_chart.jpg.
- ⁶ Yang, W. S. et al. Iodide management in formamidinium-lead-halide-based perovskite layers for efficient solar cells. *Science*, **356**, 1376–1379 (2017).
- ⁷ Søndergaard, R., Hösel, M., Angmo, D., Larsen-Olsen, T. T. & Krebs, F. C. Roll-to-roll fabrication of polymer solar cells. *Mater. Today* **15**, 36–49 (2012).
- ⁸ Yao, H. et al. Molecular design of benzodithiophene-based organic photovoltaic materials. *Chem. Rev.* **116**, 7397–7457 (2016).
- ⁹ Huang, Y., Kramer, E. J., Heeger, A. J. & Bazan, G. C. Bulk heterojunction solar cells: Morphology and performance relationships. *Chem. Rev.* **114**, 7006–7043 (2014).
- ¹⁰ An, Q. et al. Versatile ternary organic solar cells: a critical review. *Energy Environ. Sci.* **9**, 281–322 (2016).
- ¹¹ Yin, Z., Wei, J. & Zheng, Q. Interfacial materials for organic solar cells: recent advances and perspectives. *Adv. Science* **3**, 1500362 (2016).

Reference

- ¹² Ou, Q. D., Li, Y. Q. & Tang, J. X. Light manipulation in organic photovoltaics. *Adv. Sci.* **3**, 1600123 (2016).
- ¹³ Zhao, J. *et al.* Efficient organic solar cells processed from hydrocarbon solvents. *Nat. Energy* **1**, 15027 (2016).
- ¹⁴ Li, S. *et al.* Energy-Level Modulation of Small-Molecule Electron Acceptors to Achieve over 12% Efficiency in Polymer Solar Cells. *Adv. Mater.* **28**, 9423–9429 (2016).
- ¹⁵ Janssen, R. & Nelson, J. Factors limiting device efficiency in organic photovoltaics. *Adv. Mater.* **25**, 1847–1858 (2012).
- ¹⁶ Cheng, P. & Zhan, X. Stability of organic solar cells: challenges and strategies. *Chem. Soc. Rev.* **45**, 2544–2582 (2016).
- ¹⁷ Yu, G., Gao, J., Hummelen, J. C., Wudl, F. & Heeger, A. J. Polymer photovoltaic cells: enhanced efficiencies via a network of internal donor-acceptor heterojunctions. *Science.* **270**, 1789–1791 (1995).
- ¹⁸ Liao, *et al.* Additives for morphology control in high-efficiency organic solar cells. *Mater. Today* **16**, 326–336 (2013).
- ¹⁹ Dibb, G. F. A. *et al.* Influence of doping on charge carrier collection in normal and inverted geometry polymer:fullerene solar cells. *Sci. Rep.* **3**, 3335 (2013).
- ²⁰ Armin, A. *et al.* Quantum efficiency of organic solar cells: electro-optical cavity considerations. *ACS Photonics* **1**, 173–181 (2014).
- ²¹ Heeger, A. 25th anniversary article: bulk heterojunction solar cells: understanding the mechanism of operation. *Adv. Mater.* **26**, 10–28 (2013).
- ²² Shockley, W. Queisser, H. J. Detailed balance limit of efficiency of p-n junction solar cells. *J. Appl. Phys.* **32**, 510–519 (1961).
- ²³ Tang, Z., Tress, W. & Inganäs, O. Light trapping in thin film organic solar cells. *Mater. Today* **17**, 389–396 (2014).
- ²⁴ Cao, W. & Xue, J. Recent progress in organic photovoltaics: device architecture and optical design. *Energy Environ. Sci.* **7**, 2123 (2014).

Reference

- ²⁵ Betancur, R. *et al.* Optical interference for the matching of the external and internal quantum efficiencies in organic photovoltaic cells. *Sol. Energy Mater. Sol. Cells* **104**, 87–91 (2012).
- ²⁶ Park, S. H. *et al.* Bulk heterojunction solar cells with internal quantum efficiency approaching 100%. *Nat. Photonics* **3**, 297–302 (2009).
- ²⁷ Loser, S. *et al.* High-efficiency inverted polymer photovoltaics via spectrally tuned absorption enhancement. *Adv. Energy Mater.* **4**, 1301938 (2014).
- ²⁸ Martínez-Otero, A., Elias, X., Betancur, R. & Martorell, J. High-performance polymer solar cells using an optically enhanced architecture. *Adv. Opt. Mater.* **1**, 37–42 (2013).
- ²⁹ Chen, K. S. *et al.* Strong photocurrent enhancements in highly efficient flexible organic solar cells by adopting a microcavity configuration. *Adv. Mater.* **26**, 3349–3354 (2014).
- ³⁰ Betancur, R. *et al.* Transparent polymer solar cells employing a layered light-trapping architecture. *Nat. Photonics*. **7**, 995–1000 (2013).
- ³¹ Yu, W. *et al.* Highly efficient semitransparent polymer solar cells with color rendering index approaching 100 using one-dimensional photonic crystal. *ACS Appl. Mater. Interfaces* **7**, 9920–9928 (2015).
- ³² Zhang, *et al.* Colorful semitransparent polymer solar cells employing a bottom periodic one-dimensional photonic crystal and a top conductive PEDOT:PSS layer. *J. Mater. Chem. A*, **4**, 11821–11828 (2016).
- ³³ Martínez-Otero, A., Liu, Q., Mantilla-Perez, P., Bajo, M. M. & Martorell, J. An extremely thin and robust interconnecting layer providing 76% fill factor in a tandem polymer solar cell architecture. *J. Mater. Chem. A* **3**, 10681–10686 (2015).
- ³⁴ Zhou, H. *et al.* Polymer homo-tandem solar cells with best efficiency of 11.3%. *Adv. Mater.* **27**, 1767–1773 (2015).
- ³⁵ Chen, S. *et al.* An all-solution processed recombination layer with mild post-treatment enabling efficient homo-tandem non-fullerene organic solar cells. *Adv. Mater.* **29**, 1604231 (2017)

Reference

- ³⁶ Mariano, M., Rodríguez, F. J., Romero-Gomez, P., Kozyreff, G. & Martorell, J. Light coupling into the whispering gallery modes of a fiber array thin film solar cell for fixed partial sun tracking. *Sci. Rep.* **4**, 4959 (2014).
- ³⁷ Chen, J. D. *et al.* Single-junction polymer solar cells exceeding 10% power conversion efficiency. *Adv. Mater.* **27**, 1035–1041 (2015).
- ³⁸ Cho, C. *et al.* Toward perfect light trapping in thin-film photovoltaic cells: full utilization of the dual characteristics of light. *Adv. Opt. Mater.* **3**, 1697–1702 (2015).
- ³⁹ Zhou, L. *et al.* Light manipulation for organic optoelectronics using bio-inspired moth's eye nanostructures. *Sci. Rep.* **4**, 4040 (2015).
- ⁴⁰ Lan, W. *et al.* Broadband light absorption enhancement in moth's eye nanostructured organic solar cells. *AIP Adv.* **5**, 57164 (2015).
- ⁴¹ Atwater, H. A. & Polman, A. Plasmonics for improved photovoltaic devices. *Nat. Mater.* **9**, 865–865 (2010).
- ⁴² Gan, Q., Bartoli, F. J. & Kafafi, Z. H. Plasmonic-enhanced organic photovoltaics: Breaking the 10% efficiency barrier. *Adv. Mater.* **25**, 2385–2396 (2013).
- ⁴³ Cheng, P.-P. *et al.* Plasmonic backscattering enhancement for inverted polymer solar cells. *J. Mater. Chem.* **22**, 22781 (2012).
- ⁴⁴ Pastorelli, F., Bidault, S., Martorell, J. & Bonod, N. Self-assembled plasmonic oligomers for organic photovoltaics. *Adv. Optical Mater.* **2**, 171–175 (2014).
- ⁴⁵ Choi, H. *et al.* Multipositional silica-coated silver nanoparticles for high-performance polymer solar cells. *Nano Lett.* **13**, 2204–8 (2013).
- ⁴⁶ Choi, H. *et al.* Versatile surface plasmon resonance of carbon-dot-supported silver nanoparticles in polymer optoelectronic devices. *Nat. Photonics.* **7**, 732–738 (2013).
- ⁴⁷ Peters, C. *et al.* The mechanism of burn-in loss in a high efficiency polymer solar cell. *Adv. Mater.* **24**, 663–668 (2011).
- ⁴⁸ Jørgensen, M. *et al.* Stability of polymer solar cells. *Adv. Mater.* **24**, 580–612 (2012).
- ⁴⁹ Mateker, W. R. & McGehee, M. D. Progress in understanding degradation mechanisms and improving stability in organic photovoltaics. *Adv. Mater.* **29**, 1603940 (2017).

Reference

- ⁵⁰ Schaffer, C. *et al.* A direct evidence of morphological degradation on a nanometer scale in polymer solar cells. *Adv. Mater.* **25**, 6760-6764 (2013).
- ⁵¹ Rumer, J. W. & McCulloch, I. Organic photovoltaics: Crosslinking for optimal morphology and stability. *Mater. Today* **18**, 425–435 (2015).
- ⁵² Kim, B. J., Miyamoto, Y., Ma, B. & Fréchet, J. M. J. Photocrosslinkable polythiophenes for efficient, thermally stable, organic photovoltaics. *Adv. Funct. Mater.* **19**, 2273–2281 (2009).
- ⁵³ Griffini, G. *et al.* Long-term thermal stability of high-efficiency polymer solar cells based on photocrosslinkable donor-acceptor conjugated polymers. *Adv. Mater.* **23**, 1660–1664 (2011).
- ⁵⁴ Cheng, Y. J., Hsieh, C. H., Li, P. J. & Hsu, C. S. Morphological stabilization by in situ polymerization of fullerene derivatives leading to efficient, thermally stable organic photovoltaics. *Adv. Funct. Mater.* **21**, 1723–1732 (2011).
- ⁵⁵ He, D., Du, X., Zhang, W., Xiao, Z. & Ding, L. Improving the stability of P3HT/PC61BM solar cells by a thermal crosslinker. *J. Mater. Chem. A* **1**, 4589-4594 (2013).
- ⁵⁶ Rumer, J. W. *et al.* Dual function additives: A small molecule crosslinker for enhanced efficiency and stability in organic solar cells. *Adv. Energy Mater.* **5**, 1401426 (2015).
- ⁵⁷ Kim, W. *et al.* Conflicted effects of a solvent additive on PTB7:PC₇₁BM bulk heterojunction solar cells. *J. Phys. Chem. C*, **11**, 5954–5961 (2015).
- ⁵⁸ Dkhil, S. B. *et al.* Toward high-temperature stability of PTB7-based bulk heterojunction solar cells: impact of fullerene size and solvent additive. *Adv. Energy Mater.* **7**, 1601486 (2017).
- ⁵⁹ Li, Z. *et al.* Performance enhancement of fullerene-based solar cells by light processing. *Nat. Commun.* **4**, 2227 (2013).
- ⁶⁰ Heumueller, T. *et al.* Reducing burn-in voltage loss in polymer solar cells by increasing the polymer crystallinity. *Energy Environ. Sci.* **7**, 2974–2980 (2014).
- ⁶¹ Kong, J. *et al.* Long-term stable polymer solar cells with significantly reduced burn-in loss. *Nat. Commun.* **5**, 5688 (2014).

Reference

- ⁶² Cha, H. *et al.* An efficient, ‘burn in’ free organic solar cell employing a nonfullerene electron acceptor. *Adv. Mater.* **29**, 1701156 (2017).
- ⁶³ Gasparini, N. *et al.* Burn-in free nonfullerene-based organic solar cells. *Adv. Energy Mater.* **7**, 1700770 (2017).
- ⁶⁴ Ko, D. H. *et al.* Photonic crystal geometry for organic solar cells. *Nano Lett.* **9**, 2742–2746 (2009).
- ⁶⁵ Liu, Y. *et al.* Effects of nano-patterned versus simple flat active layers in upright organic photovoltaic devices. *J. Phys. D: Appl. Phys.* **46**, 024008 (2013).
- ⁶⁶ Hsiao, Y.S. *et al.* Facile transfer method for fabricating light-harvesting systems for polymer solar cells. *J. Phys. Chem. C* **115**, 11864–11870 (2011).
- ⁶⁷ Na, S.I. *et al.* Efficient polymer solar cells with surface relief gratings fabricated by simple soft lithography. *Adv. Funct. Mater.* **18**, 3956–3963 (2008).
- ⁶⁸ Nalwa, K. S., Park, J. M., Ho, K. M. & Chaudhary, S. On realizing higher efficiency polymer solar cells using a textured substrate platform. *Adv. Mater.* **23**, 112–116 (2011).
- ⁶⁹ Yu, X. *et al.* Effective light trapping enhanced near-UV/blue light absorption in inverted polymer solar cells via sol–gel textured Al-doped ZnO buffer layer. *Sol. Energ. Mater. Sol. Cells* **121**, 28–34 (2014).
- ⁷⁰ Grandidier, J., Callahan, D. M., Munday, J. N. & Atwater, H. A. Light absorption enhancement in thin-film solar cells using whispering gallery modes in dielectric nanospheres. *Adv. Mater.* **23**, 1272–1276 (2011).
- ⁷¹ Yao, Y. *et al.* Broadband light management using low-Q whispering gallery modes in spherical nanoshells. *Nat. Commun.* **3**, 664 (2012).
- ⁷² Wang, X. *et al.* Aligned ZnO/CdTe core-shell nanocable arrays on indium tin oxide: synthesis and photoelectrochemical properties. *ACS Nano*, **4**, 3302–3308 (2010).
- ⁷³ Wu, J. L. *et al.* Surface plasmonic effects of metallic nanoparticles on the performance of polymer bulk heterojunction solar cells. *ACS Nano* **5**, 959–967 (2011).
- ⁷⁴ Lu, L., Luo, Z., Xu, T. & Yu, L. Cooperative Plasmonic Effect of Ag and Au Nanoparticles on Enhancing Performance of Polymer Solar Cells. *Nano Lett.* **13**, 59–64 (2012).

Reference

- ⁷⁵ Li, X. *et al.* Dual Plasmonic Nanostructures for High Performance Inverted Organic Solar Cells. *Adv. Mater.* **24**, 3046–3052 (2012).
- ⁷⁶ Adachi, M. M. *et al.* Broadband solar absorption enhancement via periodic nanostructuring of electrodes. *Sci. Rep.* **3**, 2928 (2013).
- ⁷⁷ Pastorelli, F. *et al.* Enhanced light harvesting in semitransparent organic solar cells using an optical metal cavity configuration. *Adv. Energ. Mater.* **5**, 1400614 (2015).
- ⁷⁸ Romero-Gomez, P. *et al.* Enhanced stability in semi-transparent PTB7/PC71BM photovoltaic cells. *Sol. Energy Mater. Sol. Cells* **137**, 44–49 (2015).
- ⁷⁹ Romero-Gómez, P. *et al.* Semi-transparent polymer solar cells. *J. Photonics Energy* **5**, 57212 (2015)
- ⁸⁰ Liao, S. H., Jhuo, H. J., Cheng, Y. S. & Chen, S. A. Fullerene Derivative-Doped Zinc Oxide Nanofilm as the Cathode of Inverted Polymer Solar Cells with Low-Bandgap Polymer (PTB7-Th) for High Performance. *Adv. Mater.* **25**, 4766–4771(2013).
- ⁸¹ Liu, Q. *et al.* A Two-Resonance Tapping Cavity for an Optimal Light Trapping in Thin-Film Solar Cells. *Adv. Energy Mater.* **7**, 1700356 (2017).
- ⁸² Wang, W. *et al.* Transparent Ultrathin Oxygen-Doped Silver Electrodes for Flexible Organic Solar Cells. *Adv. Funct. Mater.* **24**, 1551–1561(2014).
- ⁸³ Ghosh, D. S. *et al.*, Highly flexible transparent electrodes containing ultrathin silver for efficient polymer solar cells. *Adv. Funct. Mater.* **25**, 7309–7316 (2015).
- ⁸⁴ Holliday, S. *et al.* A Rhodanine Flanked Nonfullerene Acceptor for Solution-Processed Organic Photovoltaics. *J. Am. Chem. Soc* **137**, 898–904 (2015).
- ⁸⁵ Zhao, W. *et al.* Fullerene-Free Polymer Solar Cells with over 11% Efficiency and Excellent Thermal Stability. *Adv. Mater.* **28**, 4734–4739 (2016).
- ⁸⁶ Zhang, G. *et al.* Efficient Nonfullerene Polymer Solar Cells Enabled by a Novel Wide Bandgap Small Molecular Acceptor. *Adv. Mater.* **29**, 1606054 (2017).
- ⁸⁷ Zhao, J. *et al.* High-efficiency non-fullerene organic solar cells enabled by a difluorobenzothiadiazole-based donor polymer combined with a properly matched small molecule acceptor. *Energy Environ. Sci.* **8**, 520–525 (2015).

Reference

- ⁸⁸ Baran, D. *et al.* Reduced voltage losses yield 10% efficient fullerene free organic solar cells with >1 V open circuit voltages. *Energy Environ. Sci.* **9**, 3783–3793 (2016).
- ⁸⁹ Cheng, P. *et al.* Realizing Small Energy Loss of 0.55 eV, High Open-Circuit Voltage >1 V and High Efficiency >10% in Fullerene-Free Polymer Solar Cells via Energy Driver. *Adv. Mater.* **29**, 1605216 (2017).
- ⁹⁰ Zhang, Y. *et al.* Nonfullerene Polymer Solar Cells based on a Perylene Monoimide Acceptor with a High Open-Circuit Voltage of 1.3 V. *Adv. Funct. Mater.* **27**, 1603892 (2017).
- ⁹¹ Wang C., *et al.* Low Band Gap Polymer Solar Cells With Minimal Voltage Losses. *Adv. Energy Mater.* **6**, 1600148 (2017).
- ⁹² Lin, Y. *et al.* Mapping Polymer Donors toward High-Efficiency Fullerene Free Organic Solar Cells. *Adv. Mater.* **29**, 1604155 (2016).
- ⁹³ Yang, Y. *et al.* Side-Chain Isomerization on an n-type Organic Semiconductor ITIC Acceptor Makes 11.77% High Efficiency Polymer Solar Cells. *J. Am. Chem. Soc.* **138**, 15011–15018 (2016).
- ⁹⁴ Zhao, W., Li, S., Zhang, S., Liu, X. & Hou, J. Ternary Polymer Solar Cells based on Two Acceptors and One Donor for Achieving 12.2% Efficiency. *Adv. Mater.* **29**, 1604059 (2016).
- ⁹⁵ Baran, D. *et al.* Reducing the efficiency–stability–cost gap of organic photovoltaics with highly efficient and stable small molecule acceptor ternary solar cells. *Nat. Mater.* **16**, 363–369 (2016).
- ⁹⁶ Li, Z. *et al.* High Performance All-Polymer Solar Cells by Synergistic Effects of Fine-Tuned Crystallinity and Solvent Annealing. *J. Am. Chem. Soc.* **138**, 10935–10944 (2016).
- ⁹⁷ G.F. Burkhard, E.T. Hoke, M.D. McGehee. Accounting for Interference, Scattering, and Electrode Absorption to Make Accurate Internal Quantum Efficiency Measurements in Organic and Other Thin Solar Cells. *Adv. Mater.* **22**, 3293(2010).
- ⁹⁸ Sannicolo, T. *et al.* Metallic Nanowire-Based Transparent Electrodes for Next Generation Flexible Devices: a Review. *Small* **12**, 6052–6075 (2016).

Reference

- ⁹⁹ Guo, F. *et al.* ITO-Free and Fully Solution-Processed Semitransparent Organic Solar Cells with High Fill Factors. *Adv. Energy Mater.* **3**, 1062–1067 (2013).
- ¹⁰⁰ Galagan, Y. *et al.* ITO-Free Flexible Organic Solar Cells with Printed Current Collecting Grids. *Sol. Energy Mater. Sol. Cells*, **95**, 1339–1343 (2011).
- ¹⁰¹ Gupta, R. *et al.* Solution Processed Large Area Fabrication of Ag Patterns as Electrodes for Flexible Heaters, Electrochromics and Organic Solar Cells. *J. Mater. Chem. A*, **2**, 10930–10937 (2014).
- ¹⁰² Ghosh, D. *et al.* Highly flexible transparent electrodes containing ultrathin silver for efficient polymer solar cells. *Adv. Funct. Mater.* **25**, 7309–7316 (2015).
- ¹⁰³ Wang, W. *et al.* Transparent ultrathin oxygen-doped silver electrodes for flexible organic solar cells. *Adv. Funct. Mater.* **24**, 1551–1561 (2014).
- ¹⁰⁴ Mateker, W.; McGehee, M. Progress in understanding degradation mechanisms and improving stability in organic photovoltaics. *Adv. Mater.* **29**, 1603940 (2016).
- ¹⁰⁵ Liu, Q. *et al.* Circumventing UV Light Induced Nanomorphology Disorder to Achieve Long Lifetime PTB7-Th:PCBM Based Solar Cells. *Adv. Energy Mater.* **7**, 1701201 (2017).
- ¹⁰⁶ Roesch, R. *et al.* Procedures and practices for evaluating thin-film solar cell stability. *Adv. Energy Mater.* **5**, 1501407 (2015).
- ¹⁰⁷ Lim, F. J.; krishnamoorthy, A. & Ho, G. W. Device stability and light-soaking characteristics of high-efficiency benzodithiophene–thienothiophene copolymer-based inverted organic solar cells with F-TiOx electron-transport layer. *ACS Appl. Mater. Interfaces*. **7**, 12119–12127 (2015).
- ¹⁰⁸ Razzell-Hollis, J. *et al.* Photochemical stability of high efficiency PTB7:PC70BM solar cell blends. *J. Mater. Chem. A* **2**, 20189–20195 (2014).
- ¹⁰⁹ Huang, W. *et al.* A facile approach to alleviate photochemical degradation in high efficiency polymer solar cells. *J. Mater. Chem. A* **3**, 16313–16319 (2015).
- ¹¹⁰ Norrman, K.; Madsen, M.; Gevorgyan, S. & Krebs, F. Degradation patterns in water and oxygen of an inverted polymer solar cell. *J. Am. Chem. Soc.* **132**, 16883–16892 (2010).
- ¹¹¹ Alem, S. *et al.* Degradation mechanism of benzodithiophene-based conjugated

Reference

polymers when exposed to light in air. *ACS Appl. Mater. Interfaces* **4**, 2993–2998 (2012).

¹¹² Mateker, W.; Sachs-Quintana, G; Burkhard, G.; Cheacharoen, R.& McGehee, M. Minimal long-term intrinsic degradation observed in a polymer solar cell illuminated in an oxygen-free environment. *Chem. Mater.* **27**, 404–407 (2015).

¹¹³ Schmidt-Mende, L. MacManus-Driscoll, J. ZnO – nanostructures, defects, and devices. *Mater. Today* **10**, 40–48 (2007).

¹¹⁴ Eugene, A.; Katz, A.; Tromholt, T. & Krebs, F. C. Electrical and photo-induced degradation of ZnO layers in organic photovoltaics. *Adv. Energy Mater.* **1**, 836–843 (2011).

¹¹⁵ Wilken, S.; Parisi, J. & Borchert, H. Role of oxygen adsorption in nanocrystalline ZnO interfacial layers for polymer–fullerene bulk heterojunction solar cells. *J. Phys. Chem. C*, **118**, 19672–19682 (2014).

¹¹⁶ Bao, Q. et al. Effects of ultraviolet soaking on surface electronic structures of solution processed ZnO nanoparticle films in polymer solar cells. *J. Mater. Chem. A*, **2**, 17676–17682 (2014).

¹¹⁷ Verbakel, F.; Meskers, S. & Janssen, R. Electronic memory effects in diodes of zinc oxide nanoparticles in a matrix of polystyrene or poly(3-hexylthiophene). *J. Appl. Phys.*, **102**, 083701 (2007).

¹¹⁸ Morfa, A. J.; MacDonald, B. I.; Subbiah, J. & Jasieniak, J. Understanding the chemical origin of improved thin-film device performance from photodoped ZnO nanoparticles. *Sol. Energy Mater. Sol. Cells* **124**, 211–216 (2014).

¹¹⁹ Heinhold, R.; Cooil, S.; Evans, D. & Allen, M. Stability of the surface electron accumulation layers on the nonpolar (10 $\bar{1}$ 0) and (11 $\bar{2}$ 0) faces of ZnO. *J. Phys. Chem. C* **118**, 24575–24582 (2014).

¹²⁰ Zhu, X.; Zhang, Z.; Men, X.; Yang, J. & Xu, X. Fabrication of an intelligent superhydrophobic surface based on ZnO nanorod arrays with switchable adhesion property. *Appl. Surf. Sci.* **256**, 7619–7622 (2010).

¹²¹ Reese, M. et al. Photoinduced degradation of polymer and polymer–fullerene active layers: experiment and theory. *Adv. Funct. Mater.* **20**, 3476–3483 (2010).

Reference

- ¹²² Chen, S. *et al.* Inverted polymer solar cells with reduced interface recombination. *Adv. Energy Mater.* **2**, 1333–1337 (2012).
- ¹²³ Trost, S. *et al.* Avoiding photoinduced shunts in organic solar cells by the use of tin oxide (SnO_x) as electron extraction material instead of ZnO. *Adv. Energy Mater.* **6**, 1600347 (2016).
- ¹²⁴ Trost, S. *et al.* Overcoming The “light-soaking” issue in inverted organic solar cells by the use of Al: ZnO electron extraction layers. *Adv. Energy Mater.* **3**, 1437-1444 (2013).
- ¹²⁵ Cowan, S. R.; Roy, A. & Heeger, A. J. Recombination in polymer-fullerene bulk heterojunction solar cells. *Phys. Rev. B*, **82**, 245207 (2010).
- ¹²⁶ Heumueller, T. *et al.* Disorder-induced open-circuit voltage losses in organic solar cells during photoinduced burn-in. *Adv. Energy Mater.* **5**, 1500111 (2015).
- ¹²⁷ Liu, Y. *et al.* Aggregation and morphology control enables multiple cases of high-efficiency polymer solar cells. *Nat. Commun.* **5**, 5293 (2014).
- ¹²⁸ Liu Q. *et al.* UV-induced oxygen removal for photostable high efficiency PTB7-Th: PC71BM photovoltaic cells. *ACS Appl. Mater. Interfaces* **8**, 28750–28756 (2016)
- ¹²⁹ Bartesaghi, D., Ye, G., Chiechi, R. & Koster, L. Compatibility of PTB7 and [70]PCBM as a key factor for the stability of PTB7:[70]PCBM solar cells. *Adv. Energy Mater.* **6**, 1502338 (2016).
- ¹³⁰ Schaffer, C. *et al.* A direct evidence of morphological degradation on a nanometer scale in polymer solar cells. *Adv. Mater.* **25**, 6760–6764 (2013).
- ¹³¹ Upama, M. *et al.* Analysis of burn-in photo degradation in low bandgap polymer PTB7 using photothermal deflection spectroscopy. *RSC Adv.* **6**, 103899–103904 (2016).
- ¹³² Inasaridze, L. *et al.* Light-induced generation of free radicals by fullerene derivatives: an important degradation pathway in organic photovoltaics?. *J. Mater. Chem. A* **5**, 8044–8050 (2017).
- ¹³³ Sapkota, S., Fischer, M., Zimmermann, B. & Würfel, U. Analysis of the degradation mechanism of ITO-free organic solar cells under UV radiation. *Sol. Energ. Mat. Sol. Cells.* **121**, 43–48 (2014).

Reference

- ¹³⁴ Jeong, J. *et al.* Significant Stability Enhancement in High-efficiency polymer:fullerene bulk heterojunction solar cells by blocking ultraviolet photons from solar light. *Adv. Sci.* **3**, 1500269 (2015).
- ¹³⁵ Tipnis, R. *et al.* Large-area organic photovoltaic module—Fabrication and performance. *Sol. Energ. Mat. Sol. Cells* **93**, 442–446 (2009).
- ¹³⁶ Kraus, H. *et al.* Analysis of triplet exciton loss pathways in PTB7:PC71BM bulk heterojunction solar cells. *Sci. Rep.* **6**, 29158 (2016).
- ¹³⁷ Bakulin, A. *et al.* Charge-transfer state dynamics following hole and electron transfer in organic photovoltaic devices. *J. Phys. Chem. Lett.* **4**, 209–215 (2013).
- ¹³⁸ Clarke, T. & Durrant, J. Charge photogeneration in organic solar cells. *Chem. Rev.* **110**, 6736–6767 (2010).
- ¹³⁹ Melzer, C., Koop, E., Mihailetschi, V. & Blom, P. Hole transport in poly(phenylene vinylene)/methanofullerene bulk-heterojunction solar cells. *Adv. Funct. Mater.* **14**, 865–870 (2004).
- ¹⁴⁰ He, Z. *et al.* Simultaneous Enhancement of Open-Circuit Voltage, Short-Circuit Current Density, and Fill Factor in Polymer Solar Cells. *Adv. Mater.* **23**, 4636–4643 (2011).
- ¹⁴¹ Distler, A. *et al.* The effect of PCBM dimerization on the performance of bulk heterojunction solar cells. *Adv. Energy Mater.* **4**, 1300693 (2014).
- ¹⁴² Burlingame, Q. *et al.* Photochemical origins of burn-in degradation in small molecular weight organic photovoltaic cells. *Energy Environ. Sci.* **8**, 1005–1010 (2015).
- ¹⁴³ Heumueller, T. *et al.* Morphological and electrical control of fullerene dimerization determines organic photovoltaic stability. *Energy Environ. Sci.* **9**, 247–256 (2016).
- ¹⁴⁴ Burlingame, Q. *et al.* Reliability of small molecule organic photovoltaics with electron-filtering compound buffer layers. *Adv. Energy Mater.* **6**, 1601094 (2016).
- ¹⁴⁵ Kim, W. *et al.* Conflicted effects of a solvent additive on PTB7:PC71BM bulk heterojunction solar cells. *J. Phys. Chem. C* **119**, 5954–5961 (2015).

Reference

¹⁴⁶ Müller-Buschbaum, P. The Active Layer Morphology of Organic Solar Cells Probed with Grazing Incidence Scattering Techniques. *Adv. Mater.* **26**, 7692–7709 (2014).

¹⁴⁷ Rivnay, J., Mannsfeld, S., Miller, C., Salleo, A. & Toney, M. Quantitative Determination of Organic Semiconductor Microstructure from the Molecular to Device Scale. *Chem. Rev.* **112**, 5488–5519 (2012).

¹⁴⁸ Liu, F. *et al.* Characterization of the morphology of solution-processed bulk heterojunction organic photovoltaics. *Prog. Polym. Sci.* **38**, 1990–2052 (2013).

¹⁴⁹ Mantilla, P. Multi-junction thin film solar cells for an optimal light harvesting. Ph.D Thesis (2017).